The Dissertation Committee for Michael Ryan Gardner certifies that this is the approved version of the following dissertation:

Scattering Angle Resolved Optical Coherence Tomography for Early Retinal Detection of Alzheimer's Disease in a Murine Model

Committee:

H. Grady Rylander III, Co-Supervisor

Thomas E. Milner, Co-Supervisor

Andrew K. Dunn

James W. Tunnell

Gracie Vargas

Scattering Angle Resolved Optical Coherence Tomography for Early Retinal Detection of Alzheimer's Disease in a Murine Model

by

Michael Ryan Gardner

Dissertation

Presented to the Faculty of the Graduate School of

The University of Texas at Austin

in Partial Fulfillment

of the Requirements

for the Degree of

Doctor of Philosophy

The University of Texas at Austin

August 2018

Dedication

In the name of God, whose light shines in the darkness, and whose eye runs to and fro throughout the whole earth.

Acknowledgements

There are many people to acknowledge for their help in this effort. Each of them contributed in unique ways and has my deepest gratitude.

My advisors have been founts of knowledge and guidance as different pieces of this dissertation came together. Dr. Rylander's ophthalmic expertise and advice has played a critical role in helping me interpret the SAR-OCT data. Dr. Milner's skills in optical design were instrumental in fostering my development as an engineer. Both of these men are admirable advisors.

The support of Dr. Dunn and Dr. Tunnell, both serving on my committee, has been appreciated. The coursework they offered was influential in pushing forward much of this work.

Our collaborators at the University of Texas Medical Branch at Galveston are skilled researchers and considerate supporters of my work. Dr. Vargas, also a committee member, and Dr. Motamedi have both offered encouraging direction and thoughtful critique of this work. Jon Luisi and Mauro Montalbano were helpful counterparts in a joint effort. Thank you all for your collaboration and for providing the mice for the Alzheimer's disease study!

My fellow lab members, Vik Baruah, Dr. Arnold Estrada, Scott Jenney, Jason King Nitesh Katta, Dr. Eun Kim, Jason King, Austin McElroy, Bharadway Muralidharan, and Dr. Tianyi Wang have each assisted me and shaped my thinking in more ways than I could possibly list here. They have truly been a joy to work with. Thank you all!

I have worked with many undergraduate researchers at UT Austin who have each contributed in different ways to my research. Thank you to each of them: Salman Zaidi,

Jongwan (Daniel) Park, Ayesha Rahman, Stefan Sierra, Amit Narawane, Elizabeth Stutzmann, Ronit (Popeye) Kar, Kristen Gentry, Matthew Prinz, Nick Ray, John Rector, Andrew Horvit, Shyon Parsa, Rogelio Salomon, Ana Perez, Madison Round, Donovan Moses, and Fawaz Mohsin.

There are several UT Austin staff members who have been a great help along the way. Kathryn Starr at the Animal Resources Center helped by training me in mouse handling and by answering countless questions I had for her. In the Mechanical Engineering machine shop, Ricardo Palacios helped me fine-tune my opto-mechanical design, and Danny Jares was masterful in his machining the parts for the SAR-OCT system. Adam Kennedy in the Chemistry glass shop has been accommodating and innovative for numerous projects in the lab, including drilling the glass PME with precision.

My parents, Brett and Betty, set a firm foundation for me in pursuing my academic studies. Their support has been a great blessing, and I could not thank them enough.

To my kids, Eloise and Simeon: While you likely won't remember our time in Austin, having you with us here has been one of the greatest joys of my life. The love you expressed to me here, in the ways you knew how, was always a refreshing reprieve from the stresses of days away from you.

Finally, to Anna, my bride: Your love, your joy, and your patience have been extraordinary. I cannot imagine a more graceful woman than you, enduring my graduate studies through such major milestones—the first few years of marriage and having two children. You are an incredible wife and mother, and I love you so much!

Scattering Angle Resolved Optical Coherence Tomography for Early Retinal Detection of Alzheimer's Disease in a Murine Model

Michael Ryan Gardner, PhD

The University of Texas at Austin, 2018

Supervisors: H. Grady Rylander III, Thomas E. Milner

Alzheimer's disease (AD), a debilitating neurodegenerative disease, is becoming more prevalent with an aging population. Early detection of AD is critical to extending healthy lives, but current techniques for AD detection are invasive and cost-prohibitive. The retina is embryonically derived from the forebrain and, with recent mounting evidence that it may reveal markers of brain injury, is considered a "window to the brain." Early neurodegenerative changes in the brain are likely to be observed in the retina—synaptic failure and shifts in mitochondrial dynamics. Optical imaging techniques could hold the key to non-invasive early detection of AD in the retina since these disruptions may be observed with light. In particular, optical coherence tomography (OCT) retinal imaging offers 3D images of retinal neurons, but the resolution of clinical OCT systems is not fine enough to observe disruptions in the sub-cellular space. Scattering angle resolved (SAR-) OCT, a new method introduced in this work, aims to access sub-resolution scattering properties which could expose fundamental changes in the neurons associated with AD.

In this dissertation, a custom SAR-OCT system and new image processing protocols are designed and constructed for murine retinal imaging. Then, three in-vivo studies are conducted using the imaging system to demonstrate its potential use in disease detection. In the first study, which establishes fundamental measures provided by SAR-

OCT, the imaging system discerns native scattering differences between retinal layers and regions in healthy mice. In the second study, significant scattering angle shifts are observed in ischemic retinas. Finally, a cross-sectional study compares a transgenic murine model of AD (3xTg-AD) with age-matched wild type controls. By examining the distribution of scattering angles detected by the SAR-OCT system, significant differences are observed in the earliest ages of the diseased mice compared the control mice. In the final chapter, limitations of these studies as well as the imaging and image processing protocols are examined, and recommendations are made for future studies to leverage SAR-OCT for early detection of AD or other neurodegenerative diseases.

Table of Contents

List of Tables

List of Figures

PART 1: INTRODUCTION AND SYSTEM DESIGN

Chapter 1: Introduction

DISSERTATION OUTLINE

This dissertation is split in two parts: (1) Introduction and System Design and (2) In-Vivo Studies and Conclusion. These parts are further divided into chapters. In part 1 there are three chapters: (1) Introduction, (2) Designing a Scattering Angle Resolved Optical Coherence Tomography (SAR-OCT) System, and (3) Image Processing and Feature Extraction for SAR-OCT. In part 2, there are four chapters: (4) Scattering Property Variation in the Mouse Retina, (5) Scattering Angle Changes During Euthanasia, (6) Retinal Changes in the Retina of a Mouse Model of Alzheimer's Disease using SAR-OCT, and (7) Conclusions and Future Work. A bank of acronym meanings is included in the glossary.

This chapter provides a primer on neurodegeneration, focusing on Alzheimer's disease. The discussion ranges from the societal impact of the disease to the biological basis of how this dissertation aims to early detect it. There is also a discussion of OCT and why it is relevant to early detection of neurodegeneration. Lastly, a discussion of the mouse retina will aid in understanding the scope of the work described this dissertation.

NEURODEGENERATION

Neurodegeneration is in fact a broad category with many expressions, including several different diseases and pathologies; several well-known diseases such as Alzheimer's disease (AD), Parkinson's disease (PD), Huntington's disease (HD), and amyotrophic lateral sclerosis (ALS) are all types of neurodegenerative diseases. In more recent years glaucoma has also been categorized as a neurodegenerative disease.[1] In the

strictest sense, neurodegenerative disease may be defined as those pathologies primarily affecting the neurons.[2]

Other diseases and pathologies affect neurons but are not considered neurodegenerative diseases. As an example, multiple sclerosis (MS) is a disease of the nervous system that implicates neurons by degrading the myelin sheath, but strictly speaking, it should not be categorized as a neurodegenerative disease because it does not have a primary pathology in the neuron itself, but instead on its attributes. Other pathologies in which neurons die as the result of a known cause (e.g. poison or infection) are not categorized as neurodegenerative diseases.

Alzheimer's Disease and Society

Of all neurodegenerative diseases, AD is the most common. It was estimated in 2016 that 5.4 million Americans have AD; 5.2 million of these people are age 65 or older.[3] Of people 65 years and older, 11% have AD, and 32% of people over 85 years old have AD.[4] In America, these numbers are expected to increase as the baby boom generation continues to age and treatment options for other diseases extend lives.[5]

Recent guidelines and criteria for diagnosing AD include a new category for symptomatic, pre-dementia phase AD known as "mild cognitive impairment (MCI) due to AD".[6], [7] However, even in this early state of the disease, significant pathophysiology has already occurred.[8] In fact, changes in the brain begin more than 20 years prior to the onset of AD symptoms.[9]–[11]

Detecting Alzheimer's Disease

Early detection of AD seems to be the best path forward for efficacious treatment of the disease,[12], [13] and delays in AD onset and progression would significantly reduce the disease's global burden.[14] Current clinical tests for AD include a variety of

psychological testing and medical imaging. Neuropsychology can be unreliable, and a patient's baseline characteristics can be hard to determine. Lumbar puncture testing, on the population level, can predict AD four to six years before the onset of clinical symptoms by elevated levels of tau,[15] but it is quite invasive. Much research energy is being put into developing biomarkers based on lumbar puncture, but as it is now, this approach has low specificity and thus is not particularly helpful in the clinical diagnosis of AD for single individuals. Magnetic resonance imaging (MRI) and computed tomography (CT) brain imaging can predict which MCI patients will develop AD;[16] though, the classification of the patient groups is unreliable with low specificity. Altogether, cost, invasiveness and non-specificity plague each of these methods, thus leaving space for a non-invasive, economical alternative for early AD detection.

Classical histopathological signs of AD include amyloid beta (Aβ) plaques, tau protein tangles, neurofibrillary tangles and neuronal atrophy,[17] but it is now known that these markers are prefaced by synaptic failure.[18] More specifically, synaptic failure is associated with mitochondrial dysfunction and changes in signaling pathways.[19], [20] In healthy neurons, mitochondria maintain a balance between fission and fusion states, dividing and fusing to form robust networks of the vital energy-producing organelles. Before classic histologic changes associated with neurodegenerative diseases are initiated, the fission-fusion balance in mitochondria is upset, with the fission state becoming more dominant.[21] Eventually, mitochondrial dysfunction can surpass a threshold and the neurodegenerative disease can be detected by contemporary detection methods.[22] Importantly, if the mitochondrial dysfunction associated with the neurodegenerative disease progresses to this level, available therapeutic interventions will not delay or reverse the disease, and patients will suffer from extreme cognitive and/or motor dysfunction.[23]

Figure 1.1 outlines the progress of the disease from early, non-detectable stages, as presented here.

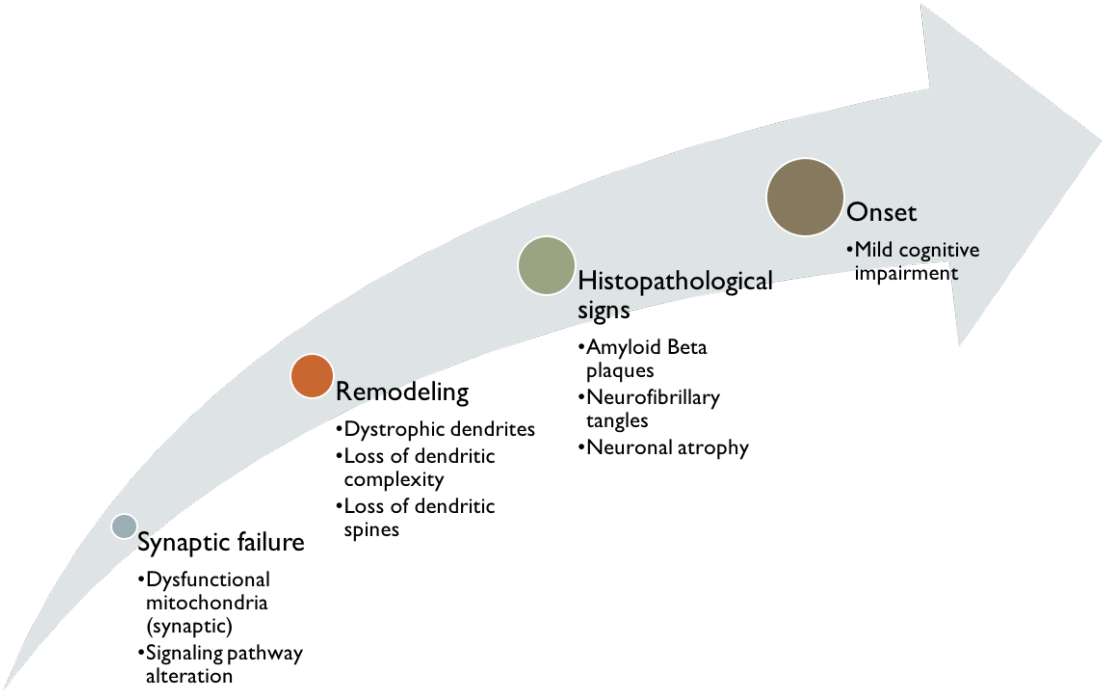

Figure 1.1: A schematic summarizes AD progression. The AD patient experiences synaptic failure, synaptic remodeling, histopathological symptoms, and finally the onset of mild cognitive impairment.

Motivating New Detection Techniques

Detecting dysfunctional mitochondria in vivo is difficult because of their small size—beyond the resolution of most in vivo optical imaging techniques. Mitochondria, however, are known to scatter light with unique characteristics making optical methods an attractive candidate to screen for patients exhibiting early mitochondrial dysfunction. Additionally, because the optic nerve is embryonically derived from the forebrain and encased within the meninges, the eye is now recognized by many investigators as a "window to the brain."[24], [25] In fact, considerable evidence suggests that many neurodegenerative diseases have a primary retinal pathology.[25]–[28] Optical coherence

tomography (OCT) has become the standard of care in ophthalmology and is routinely used to monitor changes in the retina and optic nerve. However, standard clinical OCT systems are unable to resolve disruptions in mitochondrial function.

Previous publications from Biomedical Engineering Laser Laboratory (BELL) suggest a pathway to identify sub-clinical neuropathies before any other detection method. First, a non-human primate study conducted at BELL proposed a new contrast mechanism ("reflectance index") that decreased in eyes with elevated intraocular pressure.[29] In a second BELL study, a refined measure of reflection ratios ("normalized reflectance index") revealed an early correlation with pre-perimetric glaucoma in human subjects.[30] BELL investigators suggested that the biological mechanism behind these changes is modification of the scattering properties of sub-resolution mitochondria. Consequently, a third study was conducted in which a scattering angle resolved (SAR-) OCT system was designed and constructed to inspect the optical properties of healthy human retinas.[31] In this study, ocular regions with lower retinal ganglion cell density correlated with the SAR-index, reflective of the sensitivity of SAR-OCT to morphological variation. BELL has demonstrated that SAR-OCT can identify sub-resolution light scattering variations in the retina—such as those that occur in neurodegenerative diseases (though not necessarily unique to it). Thus, there is an unmet opportunity for applying SAR-OCT to early detect AD. Furthermore, the kind of alteration to a standard clinical OCT system is the simple addition of one optical component, thus retrofitting these machines would be a viable option if SAR-OCT proved to be a viable route for early detecting neurodegeneration, particularly AD.

There are at least three advantages of detecting AD in its early stages. First, early detection creates an opportunity to begin therapeutic intervention at an earlier stage of the

disease, when remedies are more effective and can even reverse disease progression.[23], [32]

Second, a tool to early detect AD can also be used as a tool to monitor new therapeutic interventions. SAR-OCT for AD detection would be a valuable asset to researchers conducting a study on the effectiveness of their approach. Currently, longitudinal murine or human studies that aim to avoid invasive or expensive procedures must rely on behavioral or cognitive deficits, especially during early stages, but these methods are highly subjective. On the other hand, if SAR-OCT is sensitive to changes in mitochondrial dynamics, the window for monitoring AD can be pushed to a much early time.

A third benefit is that of further understanding the disease pathology. SAR-OCT creates an opportunity to study the neuro-retina in a way that it has not been studied before – non-invasively (that is, no disruption of the natural environment) with sensitivity beyond the optical resolution limits. This means that potential previously undetectable changes are now potentially accessible. Though SAR-OCT by itself cannot indicate the specific cellular mechanism behind such potential alterations to neurons in the retina, it has the distinguishing capacity to point researchers to a region that has perhaps gone unstudied, so that they might provide more insight into the fundamental nature of the disease. The correlative measures SAR-OCT offers can then serve as surrogate markers to these biological changes.

OPTICAL COHERENCE TOMOGRAPHY

In order to understand how SAR-OCT might be utilized in early-detection of AD, a brief primer on OCT is included here.

OCT is an optical imaging technique that offers tomographic information about the properties of turbid samples.[33] OCT may be thought of as a light-analog to ultrasound with gated detection of reflected photons, but because light travels so quickly it cannot be sampled by modern electronic systems as it is reflected. Thus, detecting reflected light from the sample must rely on the interferometric properties of light, instead of direct backscatter sensing. OCT offers an axial resolution between 1-15 μm—one or two orders of magnitudes finer than conventional ultrasound (50-100 μm). OCT has been used in a variety of fields, ranging from manufacturing[34]–[40] to various biological applications,[41]–[44] but the mainstay for OCT technology is ophthalmic imaging.

OCT systems scan a focused beam across the sample to probe it. One axial scan is called an "a-scan," with each point representing the backscatter of ballistic photons at corresponding depths. A series of "a-scans" in a line form a "b-scan," and several "b-scans" can then form an OCT volume (Figure 1.2).

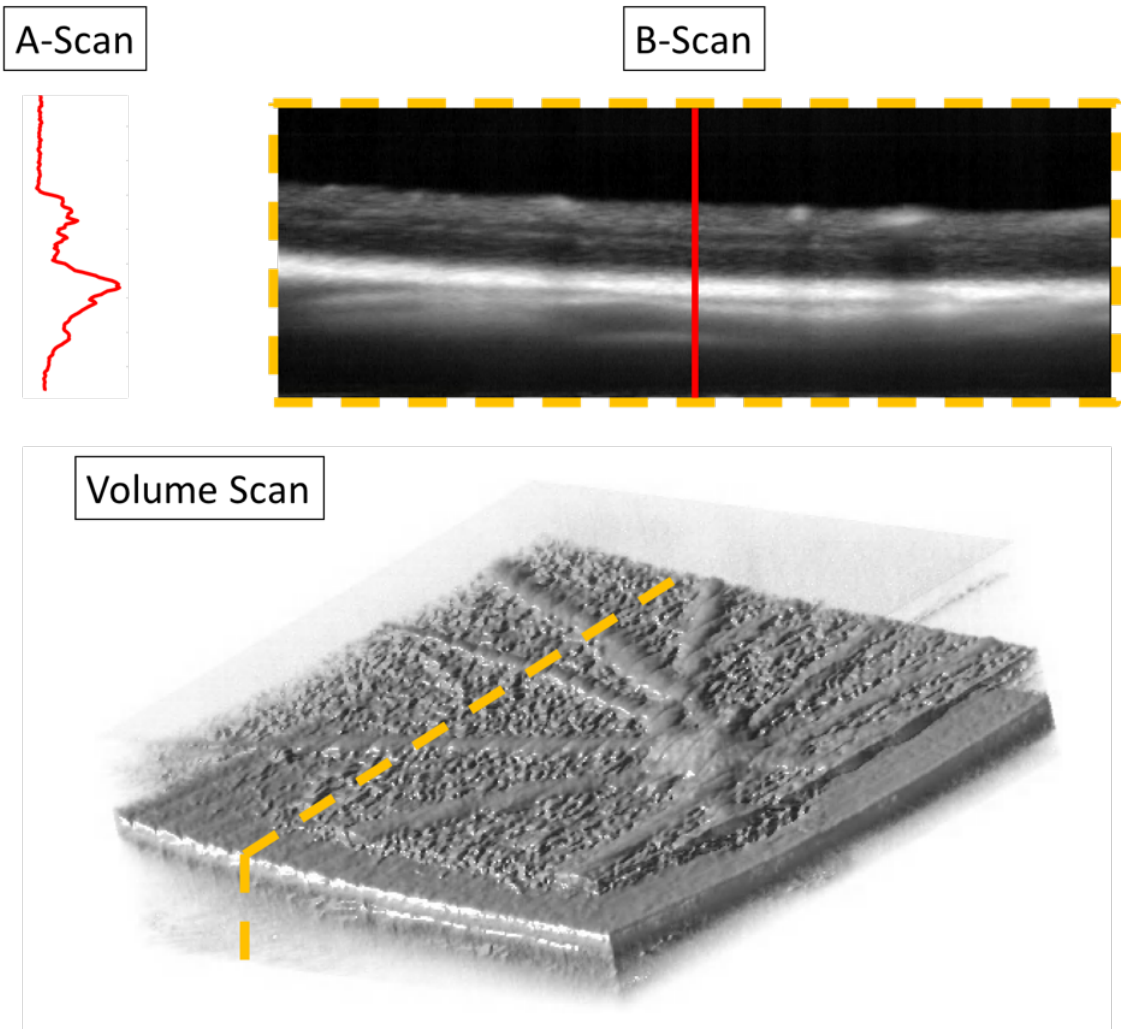

Figure 1.2: The intensity of a sample a-scan is indicated by the red line, and a sample b-scan is indicated by the yellow section. The volume scan is a collection of b-scans.

Low coherence interferometry (LCI) is the basis of OCT, and works by interfering light from a sample arm with light from a reference arm with a known pathlength. Low coherence (or white light) interferometry was described by Sir Isaac Newton, but was introduced more recently for measure optical echoes in fiber optics and waveguides,[45]–[47] as well as for biological tissue sampling.[48], [49] Figure 1.3[50], [51] diagrams a simple Michelson interferometer.

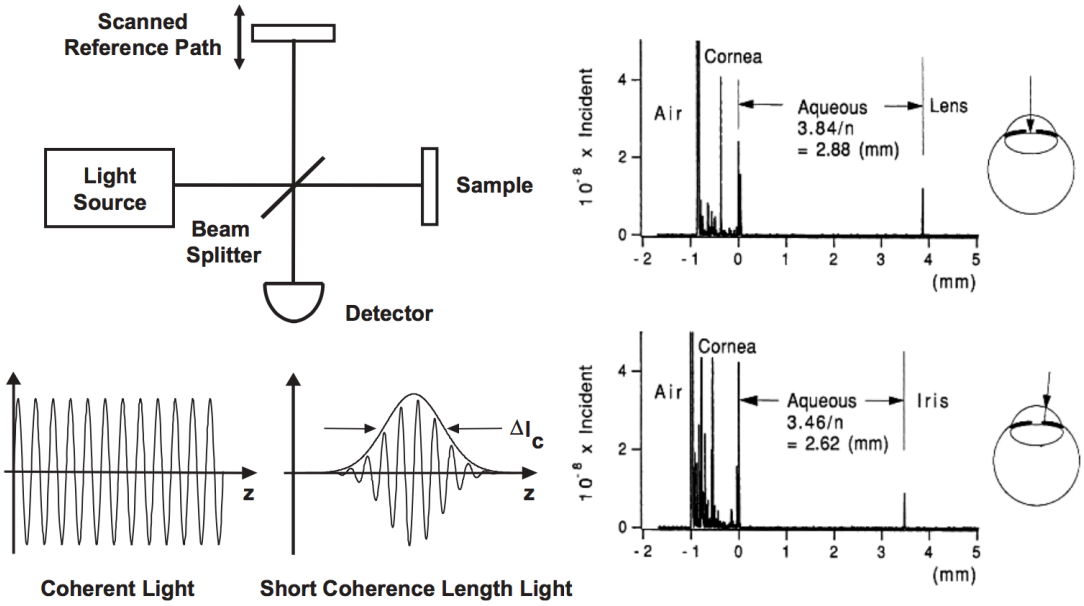

Figure 1.3: A simple Michelson interferometer (top left) that uses short coherence length light yields an interferometric signal when the reference and sample paths scatter light at pathlengths within the coherence length of the source. Example results of bovine imaging are shown on the right. [50], [51]

The intensity of the detected signal is proportional the sum of the sample and reference fields and an interaction term:

$$I_o \sim |E_r|^2 + |E_s|^2 + 2E_r E_s \cos(2k\Delta L), \tag{1.1}$$

where E_r is the reference field, E_s is the sample field, k is the wavenumber, and L is the pathlength difference.

OCT expands the utility of LCI by scanning the beam over the sample to build up volume scans. There are two categories of OCT systems: (1) time domain and (2) Fourier domain. Fourier domain systems are further split into "spectral" OCT systems that use a broadband light source and a spectrometer, and "swept source" OCT systems that use a source that sweeps through wavelengths with time and collects the interfered light at a

detector. A swept source OCT system was developed for this dissertation and is described in detail in Chapter 2 after a brief discussion of the murine retina.

THE MURINE RETINA

The retina is commonly divided into approximately thirteen anatomical layers, depending on how the layers are defined. From superficial to deep, they are (1) internal limiting membrane (ILM), (2) retinal nerve fiber layer (RNFL), (3) ganglion cell layer (GCL), (4) inner plexiform layer (IPL), (5) inner nuclear layer (INL), (6) outer plexiform layer (OPL), (7) outer nuclear layer (ONL), (8) external limiting membrane (ELM), (9) inner segment (IS), (10) outer segment (OS), (11) retinal pigment epithelium (RPE), (12) Bruch's membrane, (13) choroid (Figure 1.4).

There are five classes of neurons that make up the retinal layers: (1) photoreceptors, (2) bipolar cells, (3) ganglion cells, (4) horizontal cells, and (5) amacrine cells. The cell bodies and the synapses are located in alternating layers. Cell bodies are in the GCL, INL, and ONL, whereas synapses are located in the IPL and the OPL. The photoreceptors are the cells sensitive to light and are in the deeper layers of the retina.

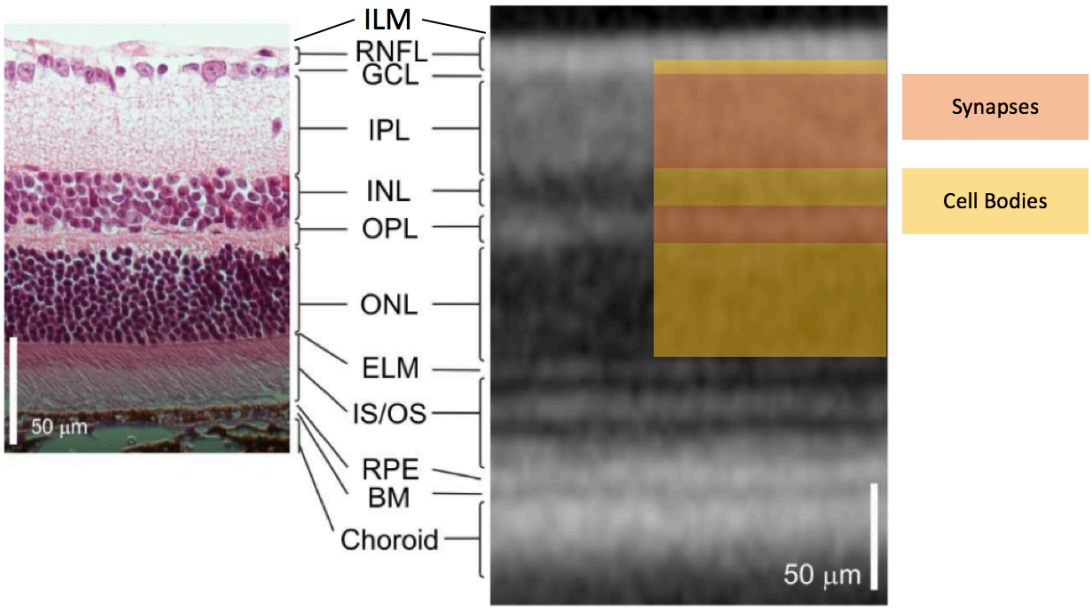

Figure 1.4: Twelve layers of the murine retina are shown on the left with H&E staining, and on the right as an OCT image. The location of synapsis and cell bodies in the retinal layers is indicated by color overlay on the right. Image adapted from Dysli.[52]

Light that is incident on the rods and cones is transduced into electrical signals by the photoreceptors, whose cell bodies are located in the ONL. Then, the electrical signals are transmitted via synapses in the OPL to the horizontal cells and bipolar cells. These cells' bodies are in the INL and transduce signal between photoreceptors (in the case of horizontal cells) and to the IPL (in the case of bipolar cells). In the IPL, the synapses of bipolar, amacrine, and ganglion cells meet. Amacrine cell bodies are in the proximal INL. Ganglion cells take the signal from the IPL synapses through the GCL and out to the optic nerve via the RNFL. (Figure 1.5). The RGC axons project to the lateral geniculate nucleus of the thalamus. The optic nerve is anatomically a tract of the brain, and *the working hypothesis of this dissertation is that the optic nerve should manifest neurodegenerative disease of the brain*.

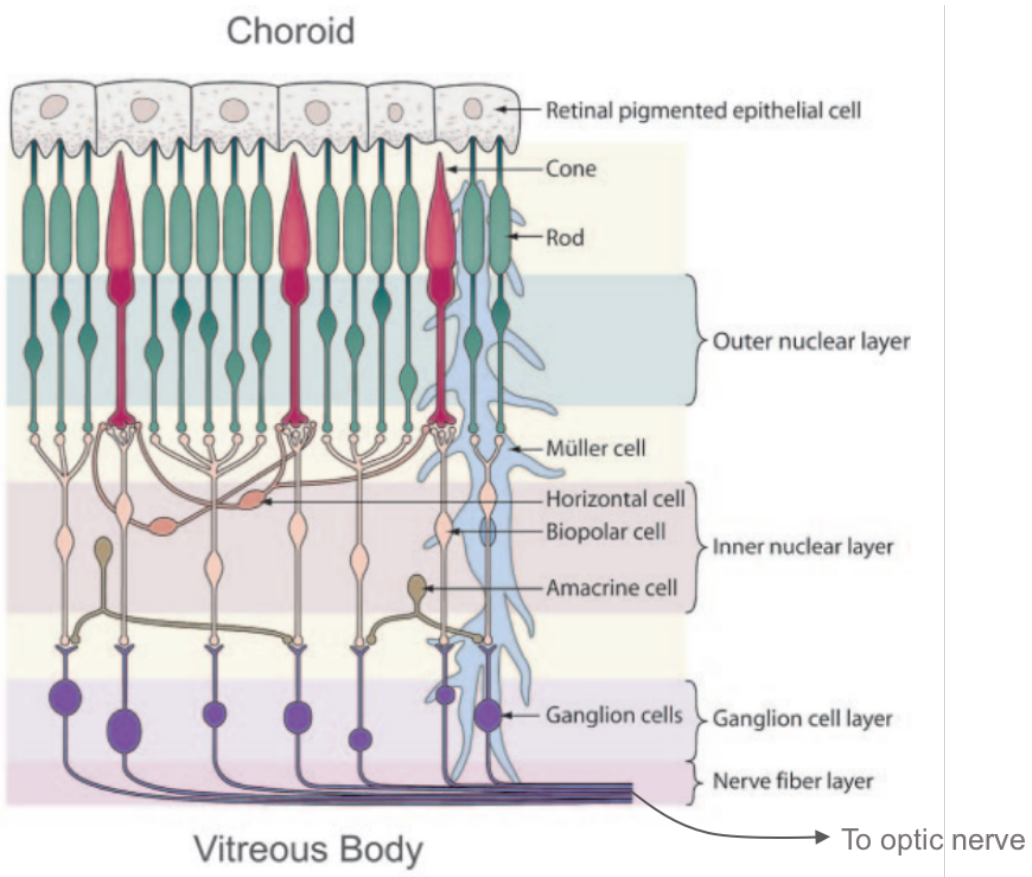

Figure 1.5: The retina is a neuron-rich tissue with horizontal and vertical information flow, segmented into several layers with distinct functions. Ultimately signals generated by incident light on the photoreceptors are transmitted to the brain via the optic nerve. Figure selected from Wang et al.[53]

Distal to the rods and cones is the RPE. The RPE serves two functions: (1) facilitating the phagocytosis of old receptor disks from the photoreceptors and (2) regenerating photopigment molecules after exposure to light.

The morphology of retinal structures is important for understanding optical imaging of the retina. Compared to synapse-rich layers, the cell body-rich layers of the retina are generally more uniform in their constitutive structures—distributions of spheroids with

vertical striations where the cell bodies connect to the synapses. The synapse-rich layers have less order. These differences are detectable in OCT images where the GCL, INL, and ONL (cell body layers) appear generally darker than the IPL and OPL (synapse-rich layers) which stand out in brightness. Brightness in OCT images is a product of backscattering due to refractive index changes at the microscopic level; higher backscattering yields a brighter image. Thus, it is observed that layers with higher morphological disorder scatter more.

The brain is considered the most metabolically active organ, and the retina is the most demanding part of the brain.[54]–[56] Of all the retinal layers, the RPE and photoreceptors are the most ATP-demanding.[57] Other high-energy demand layers include the INL and OPL, where much of the neurotransmission occurs.[58] To maintain membrane potentials, neuroglobin and mitochondria are prevalent in the plexiform layers.[59], [60] Interestingly, in avascular retinas (like those of guinea pigs and rabbits), the retina is nourished from vasculature in the choroid.[61] However, in humans and mice, which have vascularized retinas, mitochondria are localized to vascularized layers (RNFL, IPL, OPL).[59], [60]

Thus, finally, a discussion on vasculature is pertinent. In the mouse and human, larger vascular structures are located in the RNFL, with some capillary presence. As the vasculature (both mouse and human) develops, the first vessels originate from the optic nerve head and spread across the retina.[62], [63] After the network has spread across the entire retina, new vessels extend downward into the inner plexiform layer and begin to spread to form the intermediate and deep plexuses in the IPL and OPL.[63]

In the mouse retina, the superficial plexus feeds the deeper layers located in the IPL (intermediate plexus) and the OPL (deep plexus). The vasculature in the RNFL takes its blood from near the optic nerve head, where blood vessels are fed from the central retinal

artery (CRA). The ophthalmic artery feeds the CRA and the choroidal vasculature (Figure 1.6).[64]

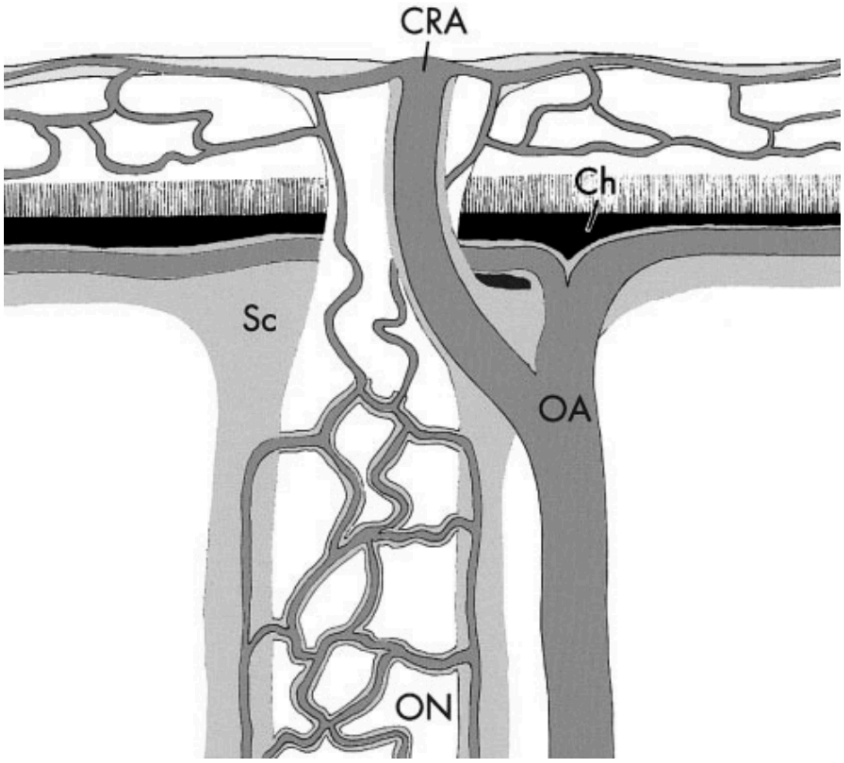

Figure 1.6: Drawing of the murine optic nerve (ON) and its vascularization taken from May et al.[64] The ophthalmic artery (OA) feeds the choroidal vasculature and the central retinal artery (CRA), which in turn feeds the intermediate and deep vascular plexuses. The choroid is indicated here by “Ch” and the sclera by “Sc.”

Chapter 2: Designing a Scattering Angle Resolved Optical Coherence Tomography System

Scattering Angle and OCT

Angle resolved imaging measures the angular distribution of backscattered light, which changes based on tissue anisotropy. Previously, angle-resolved interferometric imaging approaches have been used to detect sub-wavelength cellular properties such as the size distribution of nuclei and more recently to characterize the nuclear morphology, in situ, of both a rat model for esophageal carcinogenesis and murine retinas.[65], [66]

Scattering angle resolved (SAR-) OCT was applied by Wang et al. to the human retina where data from the additional SAR contrast mechanism correlates with known azimuthal variation in retinal ganglion cell density.[31]

Mouse Eye Model

To design an OCT system with sensitivity to symptomatic AD in mice, it is of first importance to understand the optics of the mouse eye. Many OCT studies involve mouse models of various diseases and disease states because of the mouse eye's striking similarity to the human eye (in particular, over that of a rat). This is due to the mouse eye's larger numerical aperture and higher order aberrations that resemble that of the human eye.[67] Though the optical properties of the mouse eye have been explored at short wavelengths,[68], [69] the mouse eye has not been characterized at wavelengths in the near infrared (NIR) wavelength range. This work was necessary before beginning to design an optical system to interface with the mouse eye.

To begin, the curvatures of the eye components were constructed as reported by Remtulla.[68] Then, the refractive indices of the various layers of the eye were modeled. Remtullah reports the refractive index of each layer of the mouse eye at four wavelengths.

This data was extrapolated to the NIR by fitting the four data points from Remtullah to Conrady's dispersion equation:[70]

$$n(\lambda) = n_0 + \frac{B}{\lambda} + \frac{C}{\lambda^{3.5}}. \quad (2.1)$$

In Conrady's equation, n is the refractive index, n_0 is the refractive index as λ approaches ∞, B (μm) is a parameter affecting the curvature and amplitude of the refractive index at visible wavelengths, and C [$\mu m^{3.5}$] influences the behavior of the refractive index at short wavelengths in the UV. The Conrady dispersion formula is ideal for transparent materials such as the mouse eye. The fit yielded the parameters and refractive indices in Table 2.1 at 1.31 μm.

Eye Segment	n_0	*B*	*C*	*n (at 1.31 μm)*	*RMS Error*
Cornea	1.399	-2.177×10^{-3}	1.260×10^{-3}	1.398	1.674×10^{-4}
Aqueous	1.289	3.277×10^{-2}	-1.382×10^{-3}	1.313	1.834×10^{-4}
Lens	1.635	2.831×10^{-3}	4.411×10^{-3}	1.639	2.567×10^{-4}
Vitreous	1.319	8.008×10^{-3}	2.551×10^{-4}	1.326	1.228×10^{-4}

Table 2.1: Conrady parameters for the murine ocular media

Combined, the radii of curvature and the refractive indices for each mouse eye segment yielded a suitable optical model in OpticStudio (Zemax). Figure 2.1 shows a real mouse eye cross section from Remtalluh superimposed with the optical model described above. With a sufficient model for the mouse eye, an optical design for the OCT system was developed, as described below.

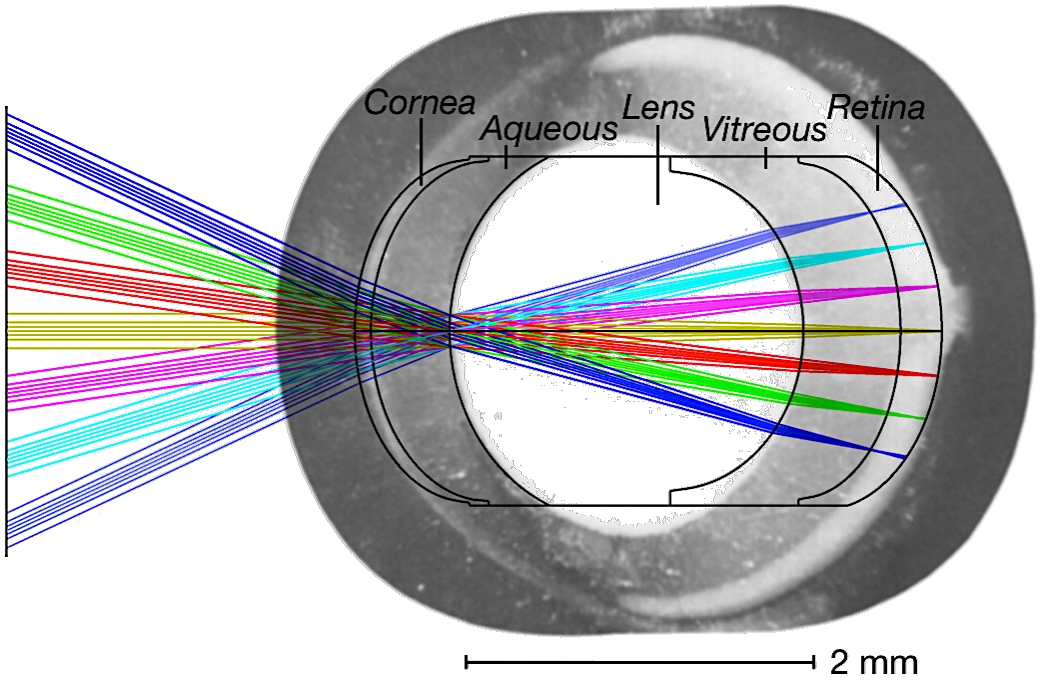

Figure 2.1: Optical model (Zemax) overlaid with an image of mouse eye cross-section. Collimated light focuses on the retina as expected.

SYSTEM DESIGN

The SAR-OCT system previously reported by Wang was for human retinal imaging, but due to animal availability and ease of access for proof-of-concept work in accelerated studies, an animal SAR-OCT system for ocular imaging is a valuable tool to examine how diseases affect the scattering properties of the retina. There are several well-documented models of neurodegenerative diseases in mice, both transgenic and induced models, that have retinal pathologies. Thus, an SAR-OCT mouse retinal imager was designed and constructed. The SAR-OCT system is diagramed in Figure 2.2, and the components are described in the following sections. A wiring diagram is included in Appendix A.

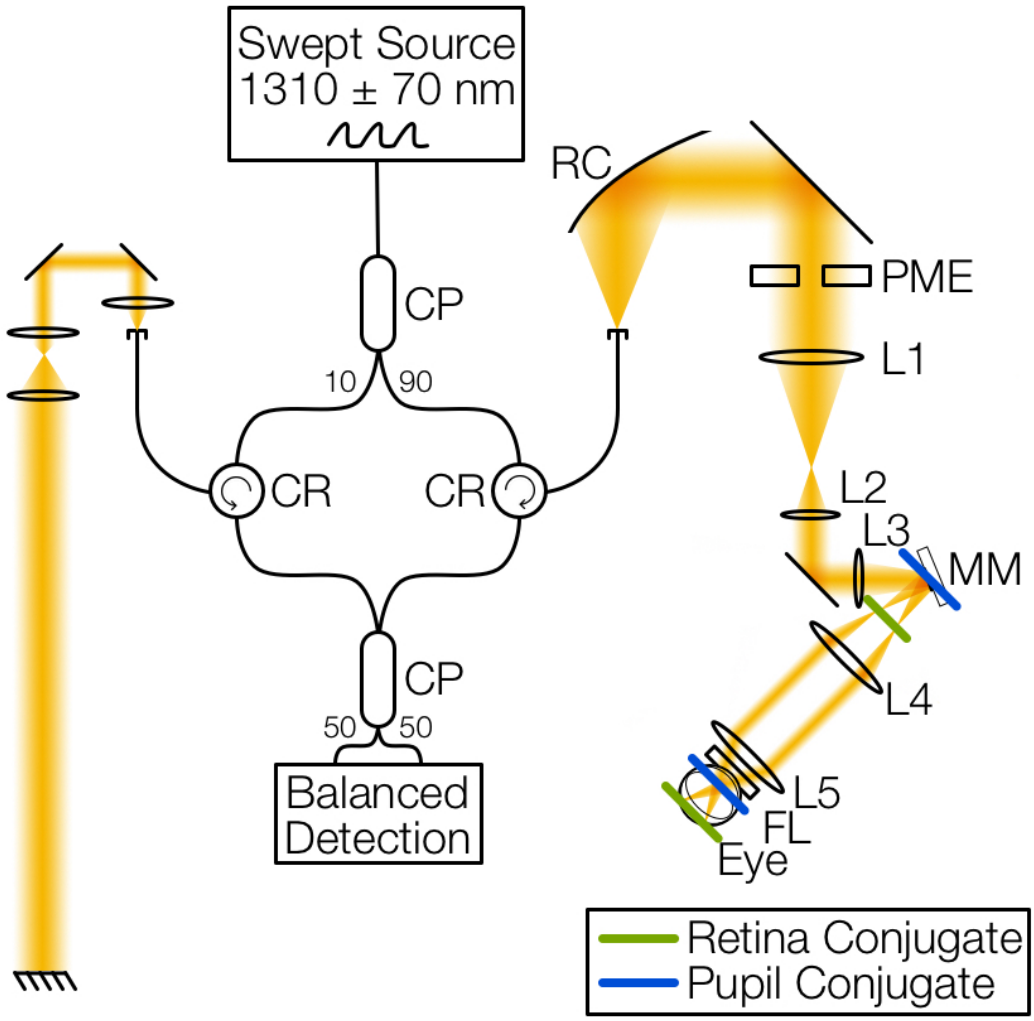

Figure 2.2: The SAR-OCT system for murine retinal imaging is diagramed. The design includes a 1310 nm ± 70 nm swept source laser and a fiber-based interferometer setup (CP): fiber coupler, CR: fiber circulator). The sample arm includes a reflective collimator (RC), pathlength multiplexing element (PME), several gradient index lenses (L1-L5), a dual-axis MEMS mirror (MM) conjugate to the ocular pupil plane, and a fundus lens (FL) that interfaces with the mouse cornea. The reference arm includes three lenses for dispersion matching and a mirror pathlength-matched to the mouse's retina.

Interferometer and Laser

Similar to the Wang design, the SAR-OCT design described here is a fiber-based system for ease of transport to the operating room. Bulk optics systems are difficult and time-consuming to align to obtain a reliable signal. Fiber optics are a good choice for ease of use and high-fidelity signals. SMF-28e fibers are used here which transmit the 1310 nm (± 70 nm) broadband swept source (100 kHz repetition rate, Axsun) in a single mode. The Axsun laser bandwidth is greater and the repetition rate faster than that of the Wang design. FC-APC fiber connections are also used so that any unwanted reflected light from fiber-fiber or fiber-component interfaces is not maintained in the single mode necessary to interfere signals with similar optical pathlengths.

A 90:10 fiber coupler directs 90% of the laser's output to the sample arm and 10% of the light to the reference arm (Figure 2.1). Each arm of the interferometer has a fiber circulator with three arms. Light entering arm 1 exits arm 2, and light entering arm 2 exits arm 3. After the sample and reference optics, the light is interfered in a 50:50 fiber coupler, and each output is measured by a balanced detection scheme. Balanced detection eliminates the background signal to isolate the interference fringe.

2D MEMS Mirror

Most murine retinal images reported in scientific literature include post-objective scanning systems. In these systems, galvanometers are placed between the final lens (objective) and the retina. Collimated light is directed by mirrors at different angles to reach different parts of the retina. This design limits the field of view of the OCT systems because the ocular pupil clips the OCT light at the system's most extreme angle.

This problem can be mitigated by placing the mirrors at a conjugate to the ocular pupil plane and thus steering the beam beyond the aperture of the pupil. However, engineers using this approach have typically used two-mirror galvanometer systems. In

this case, the designer must choose either the slow axis, the fast axis, or somewhere in-between as a conjugate plane to the ocular pupil. The slow-axis has historically been chosen to maximize collection efficiency and minimize vignetting.[71] New approaches to limit vignetting and maximize collection efficiency have included pupil tracking to control where the beam enters the pupil.[72]

Dual-axis MEMS mirrors have been used commonly in OCT catheter designs and free-space optical setups,[73], [74] but dual axis-mirrors have been more slowly adopted for retinal imaging. Recent examples include hand-held OCT retina and anterior segment imaging systems.[75], [76] In this system, our group developed the first dual axis MEMS mirror scanning system for a murine retinal OCT system, as reported by Gardner in 2017.[77]

Cornea Contact

Many OCT systems, including almost all human retinal imaging systems, are non-contact systems. That is, the objective lens does not make contact with the subject's cornea. This is particularly helpful for human subjects who may be told to hold still for several seconds while an OCT image is captured. Patient discomfort is thus minimized by removing the need for an index matching medium between the objective and the patient's cornea. Mice are typically anesthetized when their retinas are imaged using OCT, thus allowing for a corneal contact system.

One issue with non-contact OCT retinal imagers is that the beam wavefront is subject to the natural aberrations of the eye—the air/cornea and aqueous/lens interfaces providing most of the optical power. The mouse eye has significant amounts of spherical aberration and coma, with astigmatism.[78] In conflicting reports, the mouse eye has been reported as both myopic and hyperopic.[67], [78] There are also significant longitudinal

chromatic aberrations, and the mouse eye has a numerical aperture of 0.5, as opposed to a human eye's 0.2.[67]

A murine retinal imager must account for these aberrations to obtain quality images. Generally, there are two approaches to limiting the effect of aberrations in murine retinal imaging.

First, wavefront sensing and adaptive optics can improve the spot size of the beam on the retina and account for aberrations in the eye. Such systems have been reported for human retinal OCT and scanning laser ophthalmoscope systems[79], [80] and for murine retinal OCT systems.[81], [82] Classically, these OCT systems have some method of sensing the reflected wavefront (either with a Shack–Hartmann wavefront sensor or computationally). Based on the sensed wavefront characteristics, an adaptive optic element (e.g. deformable mirror, spatial light modulator) will adaptively alter the incident beam wavefront until the reflected beam has a high-quality wavefront. This intervention ensures that the beam spot size on the retina is small and thus improves spatial resolution. Although these systems are powerful tools, they are cost-prohibitive and thus will be slow to make their way to a clinical setting.

The second approach is to design a corneal contact system to limit the effect of aberrations from the air-cornea interface. This interface has the most optical power and contributes significantly to optical aberrations in the mouse eye.[68] For a more cost-effective approach to limiting aberrations, a corneal contact lens can be index matched to the cornea.

For non-contact systems, the incident beam is collimated (or its wavefront adjusted with adaptive optics) and relies on the natural optics of the eye to focus on the retina. By removing the optical power of the cornea with a contact lens, light should have some

positive (convergent) power upon entering the eye in order to focus on the retina. Figure 2.3 presents non-contact and contact designs.

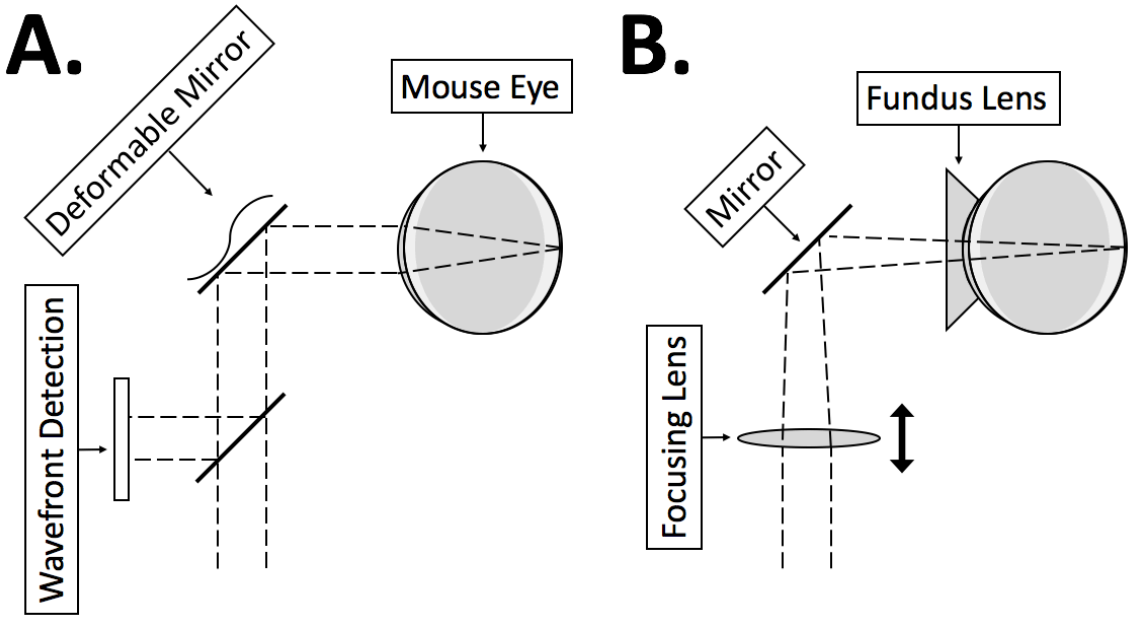

Figure 2.3: (A) Non-contact OCT systems from murine retinal imaging rely on the natural optics of the mouse eye to focus the beam. Without expensive adaptive optics, the beam is subject to the severe aberrations of the mouse eye. (B) A contact lens uses a fundus lens with one flat surface and another concave surface that is indexed matched to the cornea. This approach limits the aberration contribution of the air/cornea interface. Instead of entering the eye collimated, the beam enters with some optical power from a focusing lens. The focusing lens adjusts the focal plane at the retina to account for variations in eye length between mice.

A custom contact lens was created by the company Optics Technology by etching down a BK7 window with an anti-reflective (AR) coating. The AR coating was maintained on the non-contact side, and a concave surface was formed at the opposite side (radius = 2 mm). The AR coating limits any unwanted reflections from being coupled back into the

fiber interferometer. The concave surface is index-matched to the cornea using methyl cellulose.

Focusing Lens

Because the system uses a contact lens, the light should have some optical power upon entering the eye. However, given the variability of optical properties across different mice, particularly the thickness of ocular components, it would be advantageous to have a translating lens to optimize the spot size on the retina. Thus, the lens providing the power is placed on a translating stage. For longer eyes, the lens is translated forward to move the focal plane deeper into the eye, and vice versa. This lens and translating mount are placed before the 2D MEMS mirror, thus the diameter of the beam on the mirror (and the ocular pupil plane conjugate to the pupil) varies with the translation of the lens. Although the beam size on the mirror varies, it never is clipped by the mirror.

Dispersion Compensation

Group delay dispersion mismatch between the sample and reference arms can negatively affect OCT images by causing the full-width at half maximum (FWHM) of a surface to expand. Spectral phase expansion can be written as:

$$\phi(\omega) = \sum_n \frac{1}{n!} \phi^{(n)}(\omega_0)(\omega - \omega_0)^n, \tag{2.2}$$

where $\varphi(\omega)$ is the phase expansion relative to the center frequency, ω ($\omega = 2\pi\nu$). The units are in radians/second. The zero-th order term describes the common phase shift. The first-order term, $\varphi^{(1)}(\omega_0)$, contains the inverse group velocity, that is "group delay," and the units are in seconds. The second-order (quadratic) term, $\varphi^{(2)}(\omega_0)$, is the group delay dispersion (GDD), and the units are seconds^2.

Without dispersion compensation lenses in the reference arm, the SAR-OCT system presented in Figure 3.1 would have dramatic GDD mismatch. To characterize the dispersion mismatch of the SAR-OCT system sample and reference arms, a series of measurements was taken in which a mirror was placed in the sample arm and the reference arm. With only a single collimating lens in the reference arm, each lens of the sample arm was added, one-at-a-time, in order and the dispersion mismatch was measured.

Table 2.1 shows the 2nd order term to characterize dispersion after successive lenses and the contribution of each lens individually. The total amount of dispersion mismatch was measured to be 5.01 e-28 [s^2].

After the total dispersion mismatch was determined, two achromatic lenses were selected to match this dispersion and placed in the reference arm. After the addition of the two lenses placed in a telescopic configuration, the total dispersion mismatch was measured to be 9.50 e-29 [s^2]. This amount of dispersion was sufficient for high-quality retinal imaging.

Measurement taken after:	**Combined 2nd order terms after element [s^2]**	**Individual Contribution [s^2]**
Reflective collimator	5.40 e-31	5.40 e-31
Lens 1	1.77 e-28	1.76 e-28
Lens 2	2.61 e-28	2.61 e-28
Lens 3	3.24 e-28	6.33 e-29
Lens 4	4.21 e-28	9.65 e-29
Lens 5	5.04 e-28	8.34 e-29
Fundus lens	5.01 e-28	-2.87 e-30

Table 2.2: Contribution of each lens (summed and individual) to the dispersion mismatch.

Pathlength Multiplexing Element

The key component to the SAR-OCT system is the pathlength multiplexing element (PME). The PME is a BK7 window, 5 mm thick, with a center aperture. The center aperture has a 5 mm radius. Light in the sample arm of the SAR-OCT system has three potential optical pathlengths: Pathlength 1 is light that travels through the center aperture to and from the retina. Pathlength 2 is light that travels through the PME once—to or from the retina. Pathlength 3 is light that travels through the PME twice—to *and* from the retina. Figure 2.4 illustrates the potential pathlengths.

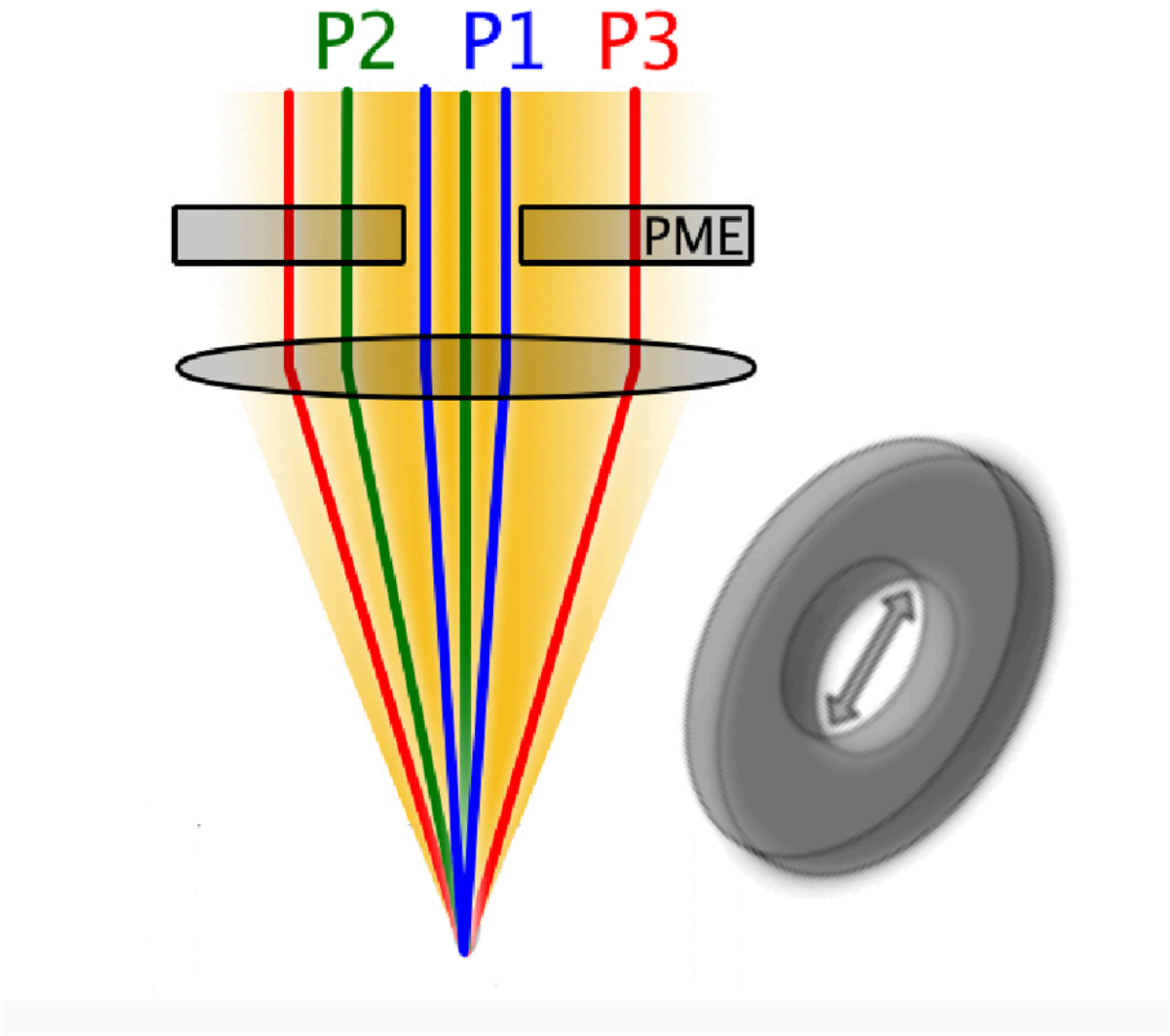

Figure 2.4: The PME introduces three potential pathlengths for light. Light mapped to pathlength 1 (P1) travels through the center of the PME to and from the retina. Light mapped to pathlength 2 (P2) travels through the PME glass only once—travelling either to or from the retina. Light mapped to pathlength 3 (P3) travels through the PME glass twice—both to and from the retina.

Mathematically, the additional pathlengths added for each path through any PME are described generally below:

Additional pathlength added for pathlength 1 (L-L) is

$$L_L = (d + d) - (d + d) = 0. \quad (2.3)$$

Additional pathlength added for pathlength 2 (L-H_2) is

$$L_{H_2} = (d + n \cdot d) - (d + d) = d(n - 1). \quad (2.4)$$

Additional pathlength added for pathlength 3 (L-H_3) is

$$L_{H_3} = (n \cdot d + n \cdot d) - (d + d) = 2d(n - 1). \quad (2.5)$$

In equations 2.3-2.5, d is the thickness of the PME, and n is the refractive index of the glass at the center wavelength of the OCT system. In the case of the 5 mm PME made of BK7 (n=1.50 at 1310 nm), L=0, H_2=2.5 mm, and H_3 = 5 mm. Thus, each sub image on the OCT is separated vertically by 2.5 mm.

A Monte Carlo model was developed to determine the effect of PME center aperture size on the intensity of light in each pathlength. Photons were randomly generated within the area of the beam, and each photon was weighted by its position in the Gaussian beam profile of the OCT source. Then, each photon was assigned a scattering angle off of the sample based on an assigned g-factor (anisotropy) of 0.97, a measured g anisotropy value for the neural retina.[83] It was recorded whether the photon travelled through the PME glass once, twice, or never, and each photon contributed to the intensity of its assigned pathlength (Figure 2.5). The scattering angle of the photon was also recorded. The results of the Monte Carlo simulation indicated that there is no single PME aperture size at which the pathlength intensities would each be equal.

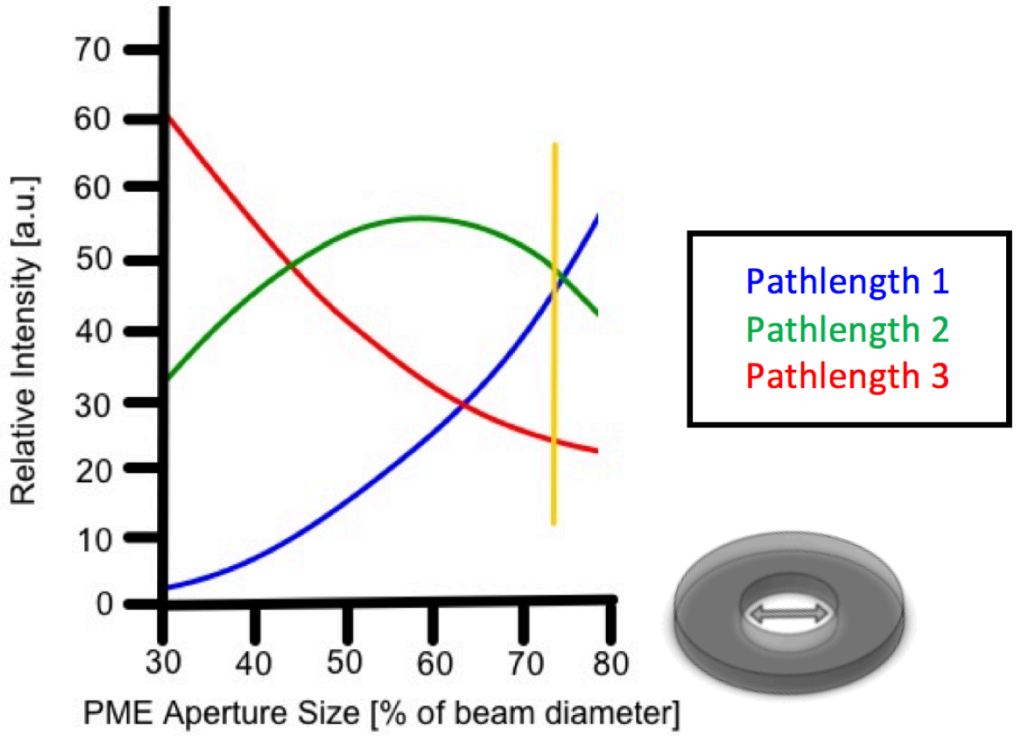

Figure 2.5: The results of a Monte Carlo simulation show the relative intensity of each pathlength as a function of PME aperture size (diameter; percent of beam diameter). The intensity of light in pathlength one increases monotonically with PME aperture size, and the intensity of light in pathlength 3 decreases monotonically with PME aperture size. The intensity of light due to photons in pathlength 2 increases and then decreases, with an infection point at a PME aperture size (diameter) of about 60% of the OCT beam diameter. The yellow vertical line corresponds to the angular distributions in Figure 2.5.

Plotting the angular distribution of scattered photons for each pathlength revealed that pathlengths 1 and 2 have the most angular discrimination (Figure 2.6). Pathlength 3 contains light that is scattered at each extreme—both direct backscattering and high-angle backscattering. This simulation makes sense when considering the model in Figure 2.4. In order to maximize the utility of the angular discrimination in pathlengths 1 and 2, a PME aperture size was chose around 72% of the beam. At this aperture size, the intensity of light

in pathlengths 1 and 2 were about equal; the intensity of light in pathlength three was about half that of pathlengths 1 and 2. This selection is indicated by the yellow line in Figure 2.5, and the angular distribution of light at this aperture size is plotted in Figure 2.6.

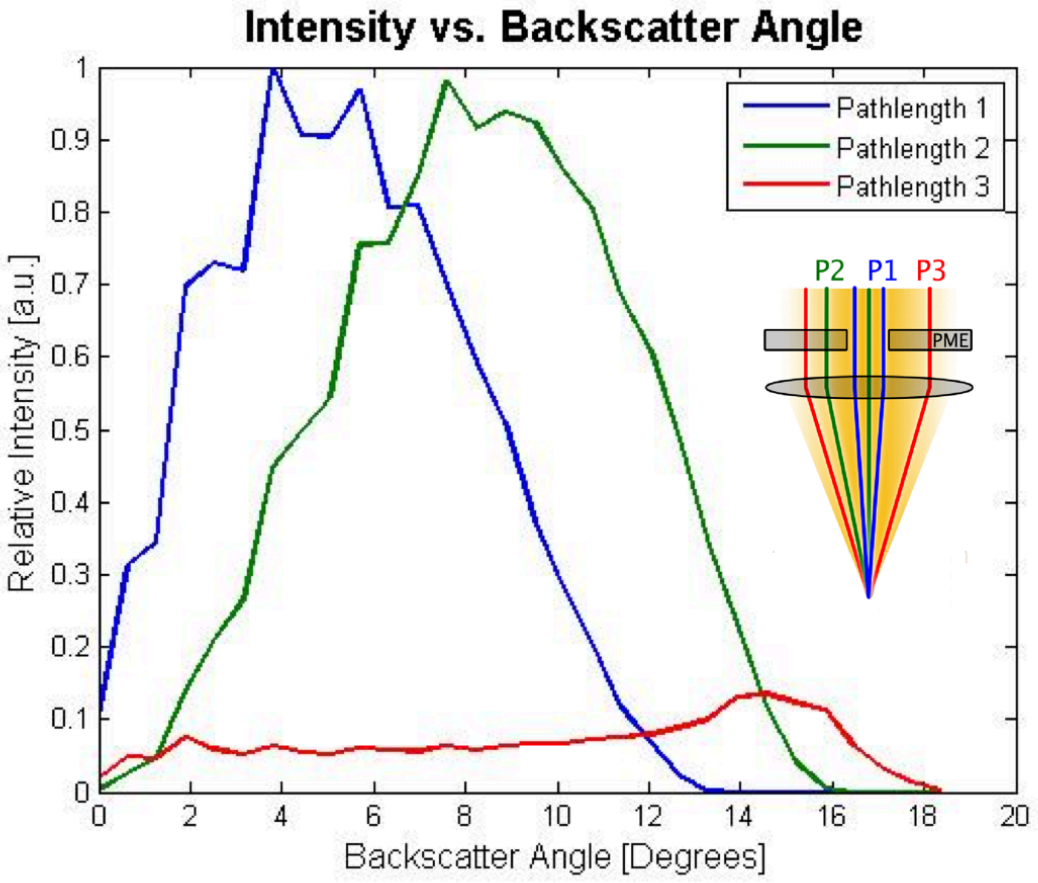

Figure 2.6: The distribution of scattering angles of photons in the Monte Carlo simulation are plotted for each pathlength. Pathlength 1 contains the lowest scattering angles, and is most distinguished from pathlength 2. Pathlength 3 contains both high- and low-angle backscattering and is thus degenerate.

Given the 12 mm beam diameter after the reflective collimator (Figure 3.1) and the discontinuity of drill bit sizes available in the glass shop, a 7 mm diameter aperture was selected for this SAR-OCT systems PME.

System Construction

It was necessary that the system be transportable to the operating room for imaging mice under anesthesia, so the SAR-OCT system was designed to be mounted on an articulating arm, which was in turn mounted on a rolling cart. To fit the arm, the system needed to be compact and stable, yet flexible enough to allow for adjusting high-precision optical components. The SAR-OCT mechanical system was custom-designed in a computer aided design (CAD) software package with a combination of off-the-shelf optical components from ThorLabs and custom aluminum components for mounting the optics. Then, the aluminum parts were machined by the University of Texas at Austin's Mechanical Engineering machine shop. A complete CAD rendering of the proposed SAR-OCT design is pictured in Figure 2.7, and a photo of the system is in Figure 2.8.

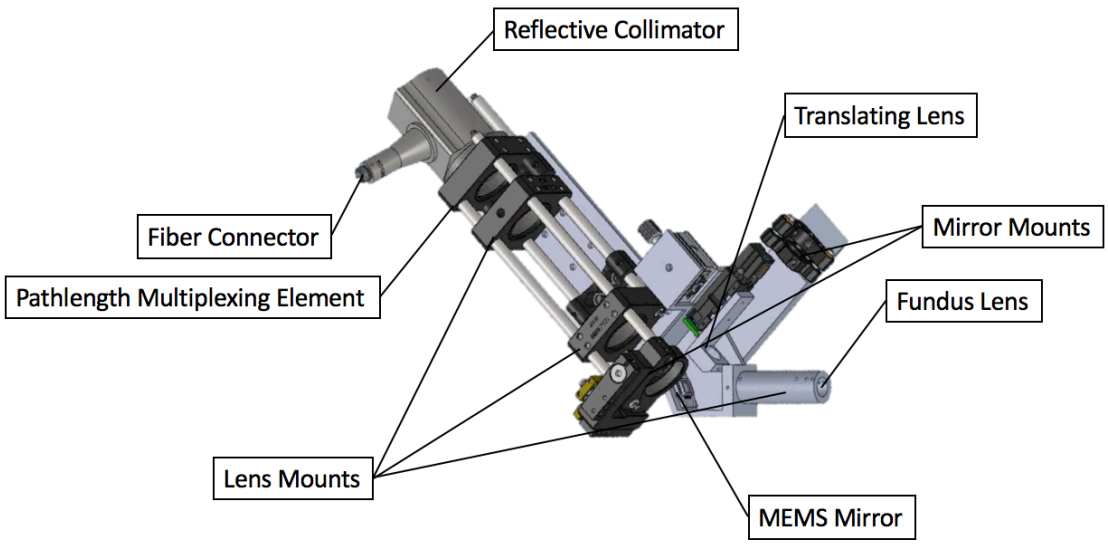

Figure 2.7: The SAR-OCT mount was designed in a CAD software using off-the-shelf components from ThorLabs and custom aluminum parts to mount the optics compactly and securely.

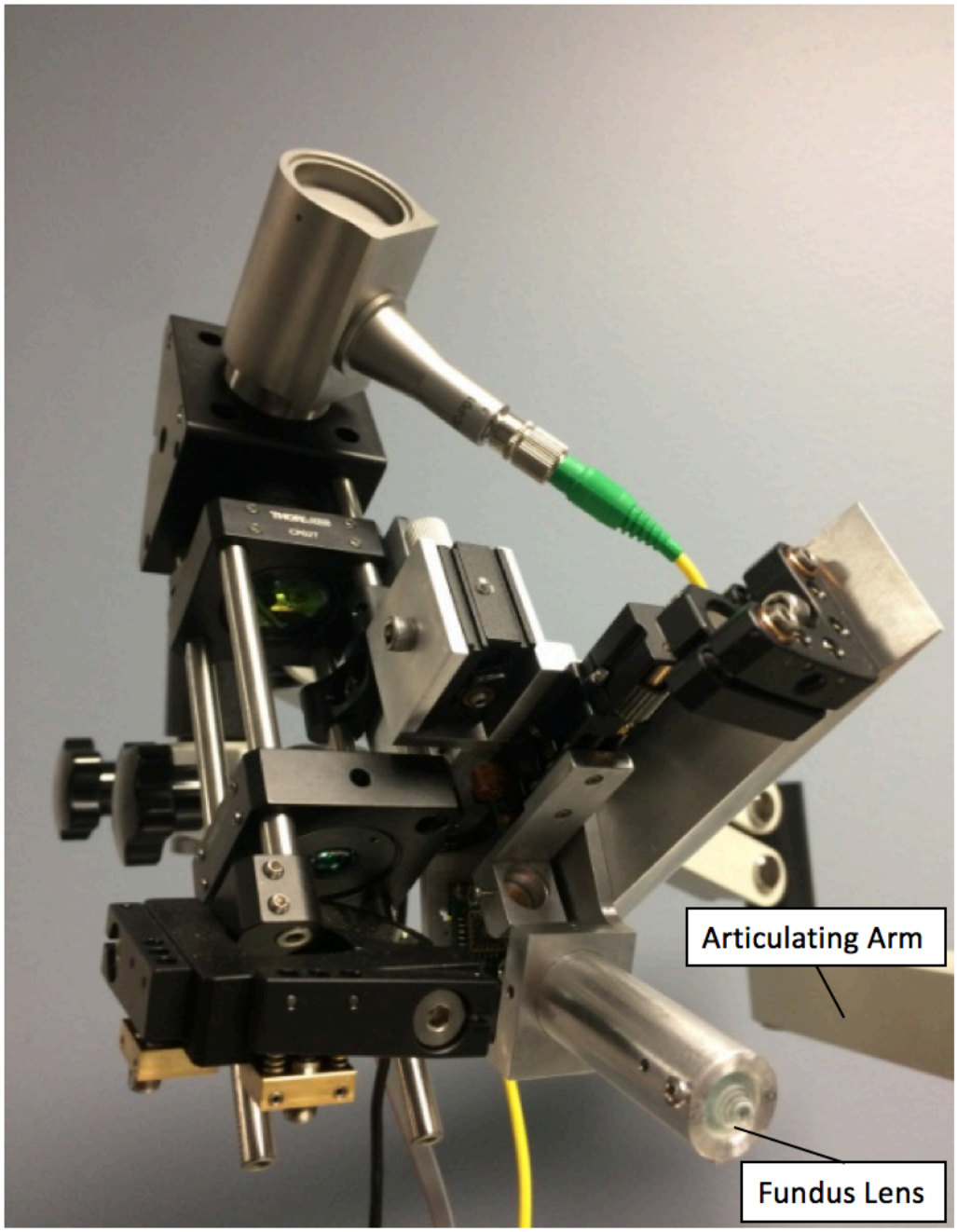

Figure 2.8: A photo of the SAR-OCT system shows a yellow fiber optic cable directing light into the reflective collimator. The fundus lens that makes contact with the mouse cornea is in the lower right-hand corner. The entire system is mounted on an articulating arm for ease of movement.

SYSTEM PERFORMANCE

Scattering Angle Characterization

To characterize the sensitivity of the system to changes in scattering angle, an experiment was designed in which light was reflected back at known angles. A dual-axis MEMS mirror was placed just beyond the focal plane of the objective lens and raster-scanned to collect a range of pathlength intensities corresponding to bulk scattering angles (Figure 2.9). The incident beam was not scanned in this configuration, only the angle at which the light was reflected from the dual-axis MEMS mirror in the focal plane. The dual-axis MEMS mirror only tilted ±4 degrees in the x and y directions; thus, several raster scans were collected with various tilt offsets and stitched together in post-processing. Figure 2.10 shows sample B-scans from this experiment.

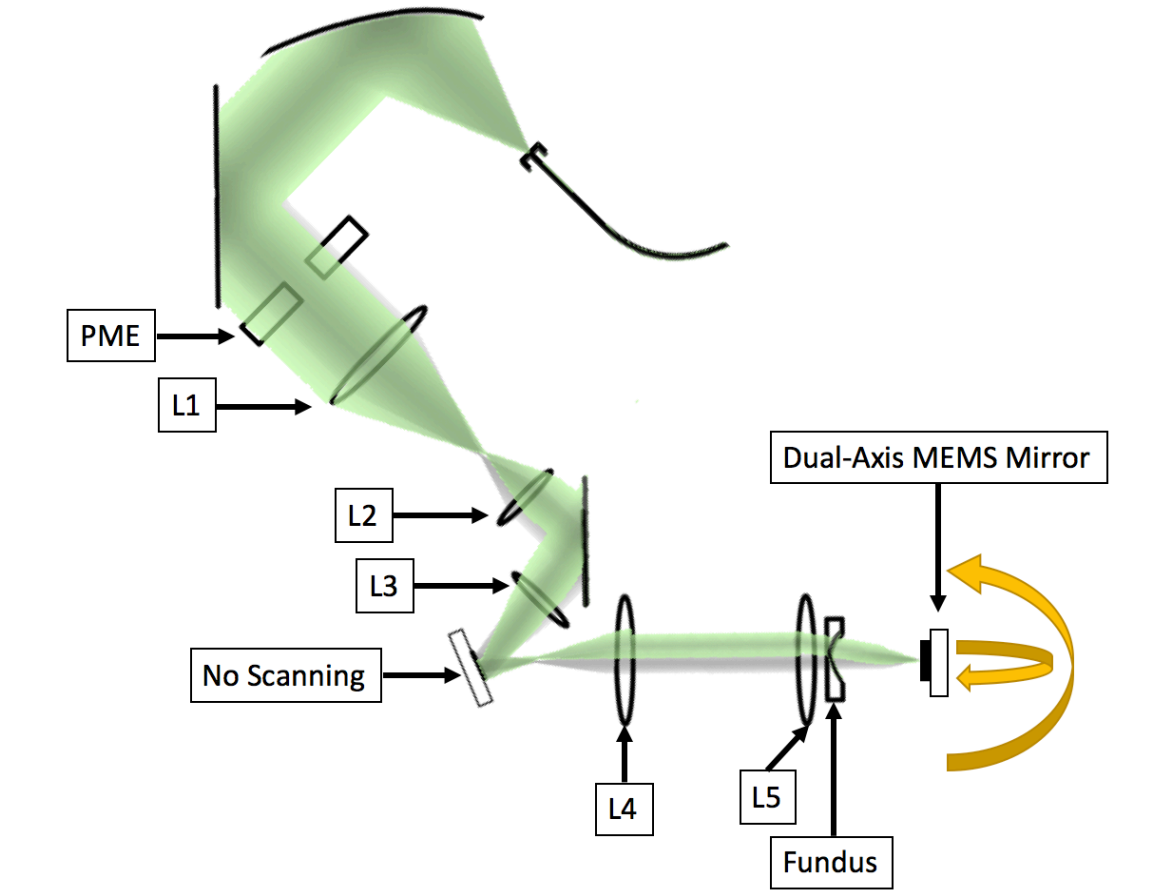

Figure 2.9: A dual axis MEMS mirror located at the focal plane raster scans through a range of bulk backscattering angles. The grayscale beam is the incident beam, and the green beam is an example reflected beam. The green beam, reflected with some angular deviation due to the dual-axis MEMS mirror, depicts more light travelling through the glass of the PME than the incident beam had. One would expect that the resultant images would have higher intensity in pathlengths 2 and 3 (H_2, H_3) and lower intensity in pathlength 1 (L) compared to a beam that is reflected with no angular deviation.

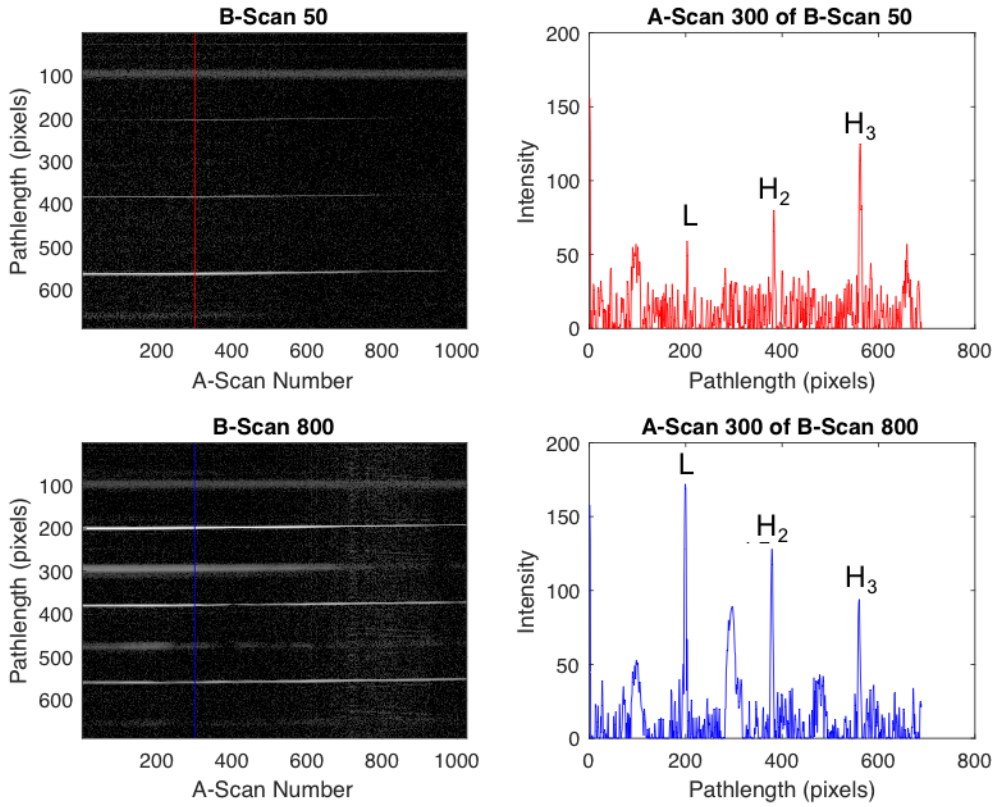

Figure 2.10: Sample b-scans show how the intensity of pathlengths 1, 2, and 3 vary for different angles. At a-scan 300 of b-scan 50, pathlength 3 (H_3) has the strongest intensity. This indicates that the mirror was at an extreme angle. In contrast, a-scan 300 of b-scan 800 has a strong pathlength 1 (L) has the strongest signal; this indicates that the mirror was at an angle closer to zero (direct back-scatter). A-scan numbers represent a linear increase in bulk scattering angle in one dimension, and b-scan numbers represent a linear increase in bulk scattering angle in the other dimension. See Figure 2.11(A) for the transformation from a-scan/b-scan number to angle.

Depths corresponding to the MEMS mirror at pathlengths 1-3 were isolated, and then intensity values corresponding to a given reflection angle were averaged azimuthally in reference to the neutral position (degree 0,0) (Figure 2.11). Figure 2.11(A) shows the intensity of each pathlength for each angular displacement, and Figure 2.11(B) plots the

intensities after azimuthal averaging. The sample a-scans in Figure 2.10 are also indicated in the same color by vertical dashed lines in Figure 2.11(B).

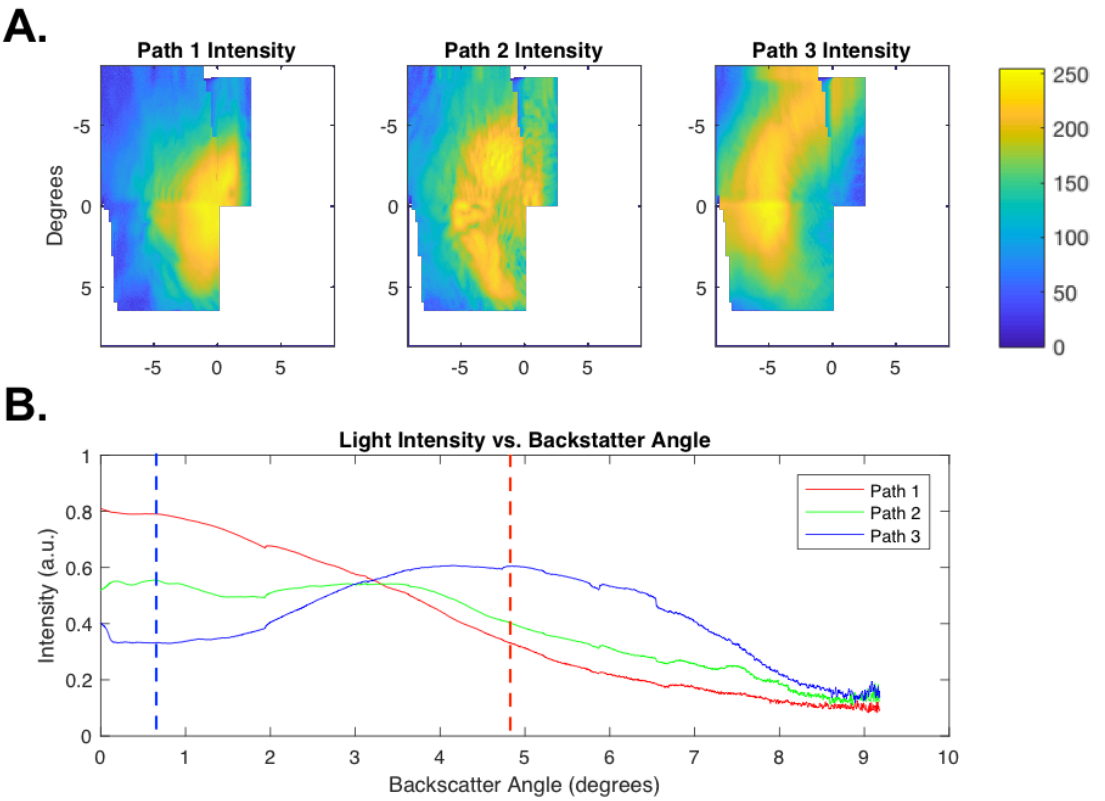

Figure 2.11: (A) shows the peak intensity of each pathlength as a function of angular deviation due to the dual-axis MEMS mirror raster scanning. Several images were stitched together to form a more complete data set. (B) shows the azimuthal average of each pathlength intensity. The blue dashed line is matches the location of the blue line in Figure 2.10. The red dashed line matches the location of the red line in Figure 2.10.

It was thus experimentally determined that the SAR-OCT murine retinal imaging system described here is able to detect changes in bulk scattering angle up to around eight degrees from a direct backscatter. That is, from a zero-degree backscattering angle to an eight-degree backscattering angle, the combination of light from pathlengths one, two and

three have unique contributions to the total image intensity. Light scattered from a sample at an angle greater than eight degrees will not be coupled back into the SAR-OCT system. Developing an image feature based on the intensities of different pathlengths is described fully in Chapter 3.

Imaging

Finally, murine retinal images were gathered using the SAR-OCT system, and the total intensities in each pathlength for 32 mice were recorded. The intensities were normalized to the pathlength with the maximum intensity. Based on the Monte Carlo model results shown in Figure 2.4, the light intensities in pathlengths 1 and 2 should be about the same, and the intensity of light in pathlength 3 should be about 50% of the intensity of light in pathlengths 1 and 2. The experimental results showed a greater intensity of light in pathlength 3 than the Monte Carlo simulation predicted (Figure 2.12), but it is beneficial to err on the side of more balanced pathlength intensities. Sample OCT retinal images are shown in Figure 2.13.

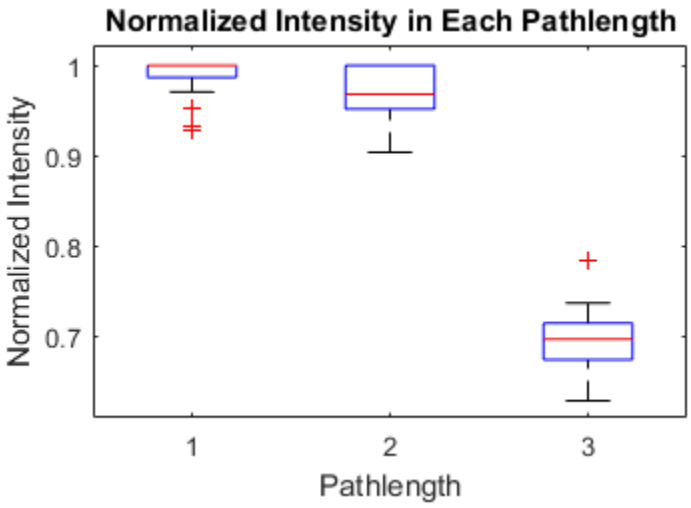

Figure 2.12: The distribution of normalized intensity of each pathlength is shown for 32 mouse retinal images. The mean normalized intensity was 0.99 for pathlength 1, 0.97 for pathlength 2, and 0.69 for pathlength 3.

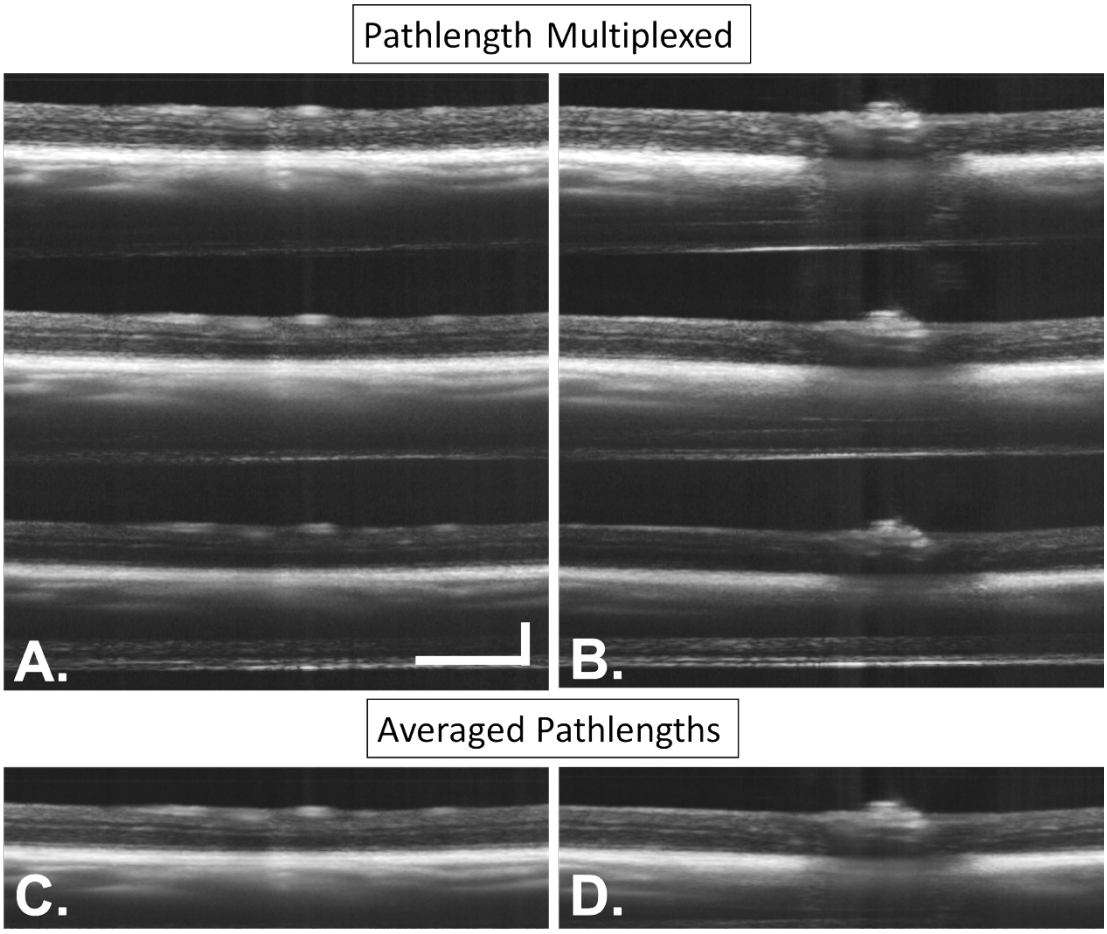

Figure 2.13: Sample SAR-OCT images (A) and (B) show cross-sectional images of the same mouse at two different locations. Pathlengths 1, 2, and 3 are seen. Each of the pathlengths has been averaged to obtain images (C) and (D). Scale bars indicate 300 μm.

Chapter 3: Image Processing and Feature Extraction for SAR-OCT

Image processing for SAR-OCT may be split into four broad categories: (1) initial processing, (2) intensity processing, (3) speckle processing, and (4) segmentation. These processes contribute to four analysis regimes for feature extraction: (1) scattering angle, (2) angiography, (3) normalized reflectivity, and (4) layer thicknesses. This chapter will discuss in-depth each of these four processes (and sub-processes), as well as the four analysis regimes. Figure 3.1 presents a flow chart to anchor the discussion of each processing and analysis step.

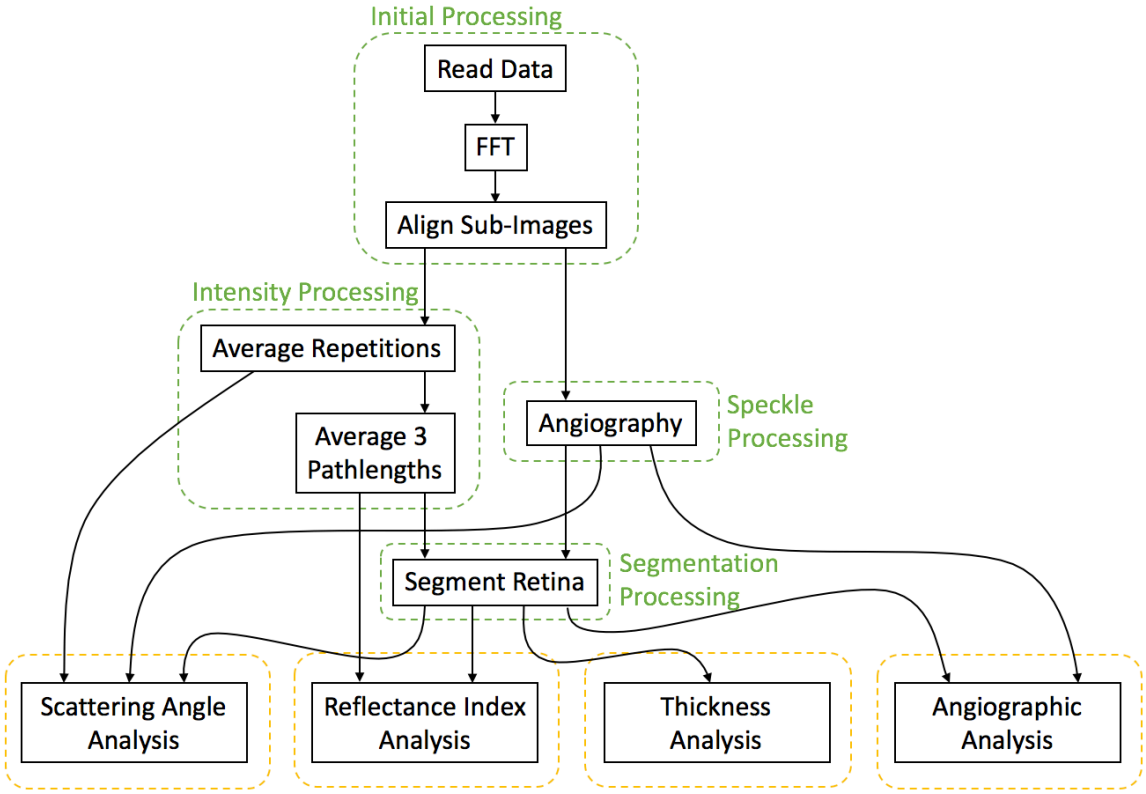

Figure 3.1: A flow chart for signal processing serves as an anchor for this dissertation chapter. Processing steps are indicated by green boxes, and the four analysis steps for feature extraction are indicated by yellow boxes.

PROCESSING STEPS

Initial Processing

The first step in image processing for SAR-OCT is to convert the raw fringe signal to tomograms. Sampled voltages from the balanced detection scheme are saved as 8-bit unsigned integers, and the parameters used to collect the tomogram are saved in a parameters file. The parameters file includes the number of A-scans per B-scan, number of B-scans, the number of times a B-scan is repeated, and the number of samples per A-scan. Figure 3.2(A) shows the fringe data for a single B-scan. Each volume is of size 1472 pixels (height; points per A-scan) × 512 pixels (width; A-scans per B-scan) × 4096 (depth; number of B-scans, 512, times the number of repetitions at each B-scan location, 8).

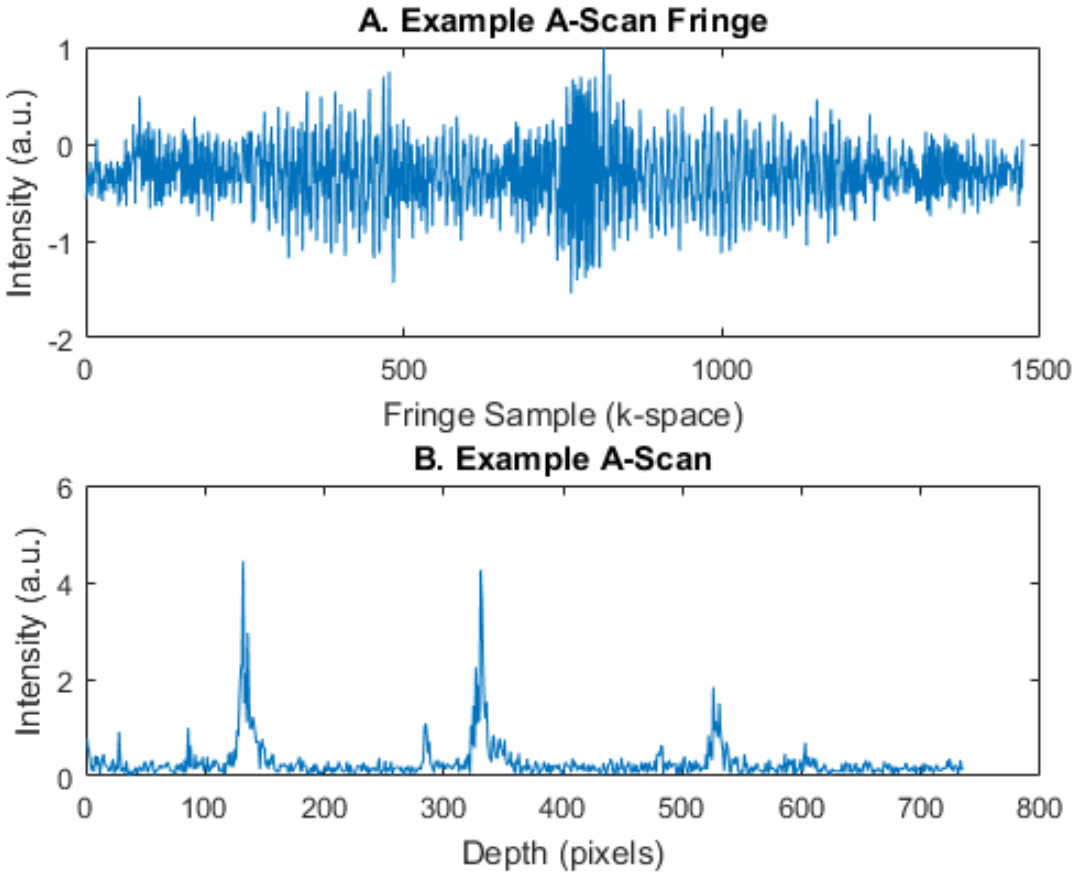

Figure 3.2: (A) shows an example SAR-OCT a-scan fringe taken on a mouse retina. (B) shows an example a-scan after the Fast Fourier Transform. The three pathlengths can be seen in the repeating pattern of two peaks, one small (the internal limiting membrane) and one large (the retinal pigment epithelium).

The data is loaded into MATLAB one b-scan at a time. Once a volume of fringe data is formed, a Fast Fourier Transform (FFT) transforms the fringe signal from k-space to image-space. An example image-space a-scan is displayed in Figure 3.2(B). The real part of the data is retained and may be displayed as a cross sectional image after converting to decibels ($20*\log_{10}$). The volume of the real part of the data has size 737 (height; 1472/2 + 1 after FFT) × 512 (width) × 4096 (depth).

With the inclusion of the PME, three pathlengths are evident in every B-scan, each corresponding to three different bulk scattering angles (see Chapter 2). To align the images for analysis, the first sub-image (pathlength 1) is used as a reference. Sub-images are selected manually, each with the same height (typically ~150 pixels). Then pathlengths 2 and 3 are shifted in the z-direction (axially) to align with pathlength 1. The MATLAB function '*imregister*' is set to perform only axial shifting for precise alignment. After the sub-images are aligned, each pathlength sub-image is saved as a tiff stack. This results in three image stacks with size 150 (height) × 512 (width) × 4096 (depth).

This first initial processing step outputs three aligned image stacks. With these three stacks, intensity processing, speckle processing, and segmentation may be performed before the four subsequent analysis steps for feature extraction.

Intensity Processing

Before analysis can be performed, the eight repeating b-scans in each b-scan location are first averaged together and collapsed into one b-scan. Thus, the three sub-images previously aligned and saved are taken from size 150 × 512 × 4095 to 150 × 512 × 512. Averaging over the eight repeated b-scans yields higher signal-to-noise ratios (SNR) as is apparent in Figure 3.3. These three volumes, corresponding to each of the three pathlengths, are used in scattering angle analysis (described later).

The second process under intensity processing is to take the three sub-images (150 x 512 x 512) and average them together, voxel-by-voxel. This averaging further increases the SNR and permits more repeatable analysis of layer thickness and reflectance index.

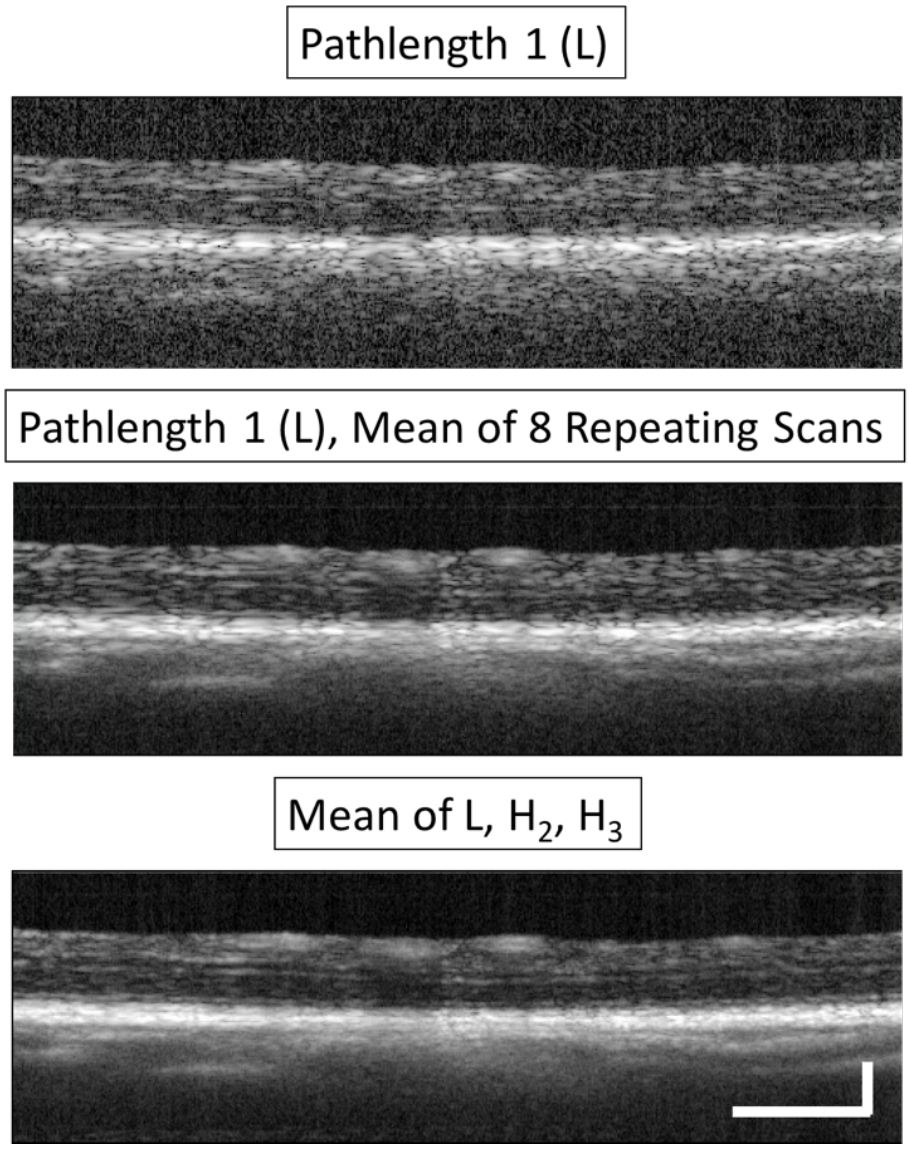

Figure 3.3: The first image shows pathlength 1 (L) of a single b-scan repetition of a mouse retina with no averaging. The second image shows the same location after averaging 8 repeating b-scans (pathlength 1). The third image shows the average of pathlength 1 (second image) and the corresponding averaged b-scans for pathlengths 2 and 3. The SNR increases with each averaging step. The scale bars show 300 μm.

Speckle Processing

Angiography Method

There are several established methods of determining areas of blood flow using OCT for biomedical imaging. These can be divided into three categories: methods that use the OCT (1) phase signal only, (2) amplitude signal only, and (3) complex signal.

The earliest OCT angiography publications relied on only the phase of the OCT signal. These methods leveraged the Doppler shift of light due to the movement of blood in the tissue to detect blood flow, including the velocity vector.[84], [85]

There are several intensity-based methods that rely on changes in the intensity of b-scan pixels across repeated b-scan measurements. These amplitude approaches are good for OCT systems in which the source is not phase-stable,[86] and these approaches are less sensitive to the Doppler angle than phase-only approaches.[86] On the other hand, the amplitude approach to angiography also discounts any signal from moving particles that are not significant enough to affect the amplitude, but instead affect only the phase. Amplitude-based methods were first proposed by Barton and Stromski,[86] and include speckle variance (sv-) OCT,[87] log-based intensity subtraction,[88] linear intensity subtraction methods,[89] simple intensity thresholding,[90] correlation mapping,[91] and split-spectrum amplitude decorrelation angiography (SSADA).[92]

A third group of OCT angiography approaches are those that combine phase and amplitude signals. Optical microangiography (OMAG) is a common approach that subtracts successive complex B-scans collected in an B-M-mode setting (repeating B-scans in the same location).[93] Another approach is complex differential variance (CDV), which intrinsically limits phase noise due to bulk motion.[94] Because of its outperformance of other methods based on angiographic analysis of collected SAR-OCT retinal images, CDV was selected as the angiographic method for this dissertation.

The CDV signal for any given a-scan can be described as

$$f_{CDV}(z) = \sqrt{1 - \frac{\sum_{t=1}^{M-1} \left| \sum_{k=-L}^{L} w(k) R(z-k,t) R^*(z-k,t+1) \right|}{\sum_{t=1}^{M-1} \sum_{K=-L}^{L} w(k) \frac{1}{2} \left[|R(z-k,t)|^2 + |R(z-k,t+1)|^2 \right]}}, \quad (3.1)$$

where M is the total number of repeating b-scans, L (more precisely, $2L+1$) is the length of the kernel, w is the depth window function, and R is the complex OCT signal at time point t ($R = A(z,t)e^{i\phi(z,t)}$). Thus, $R \cdot R^*$ represents the complex differential A-scan. The coherent average is normalized by division with the incoherent average of the original A-scan data.

Angiography Filtering

Three sequential processes take CDV volumes as input in order to obtain high-fidelity angiograms: (1) filtering to remove bulk motion, (2) Frangi vesselness filter to improve SNR, and (3) adaptive thresholding for binarizing angiograms.

Despite the CDV algorithm's robustness to handle bulk motion compared to other methods, the problem of bulk motion can still be seen clearly in the first row of images in Figure 3.4, where vertical lines obscure vascular structures. These vertical lines are due to bulk movements of the mouse including heart beat and breathing. For filtering, these lines are first detected manually, with the user clicking to the left and right of a line in the superficial plexus image. The width of the line is then determined by a custom MATLAB script, and the entire artifact is replaced with values taken from the left and right of the obscuring line. The same replacement process is repeating automatically in the intermediate and deep plexuses.

The second filtering process applies the Frangi vesselness filter[95] to the filtered image to isolate those areas of the image that are vessel-like. The Frangi filter, which uses Gaussian-like distributions with user-defined widths to search for vessel-like features, is a helpful tool for the retina because the sizes of the vessels are generally known, a priori.

The Frangi filter takes as inputs the size distribution of vessels and searches for structures that are around that size. If not handled carefully, this processing step could introduce false vessel structures from noise.

The final step was to binarize the image such that more intensive vascular analysis could be performed. The image was binarized using a built-in MATLAB filter with adaptive thresholding. One note here is that adaptive filtering assumes the presence of a vessel; thus, Chapter 4, a euthanasia experiment for which blood flow ceases at some time point, replaces this step with a non-adaptive thresholding method. This isolated deviation from the image processing protocol is discussed more fully in Chapter 5.

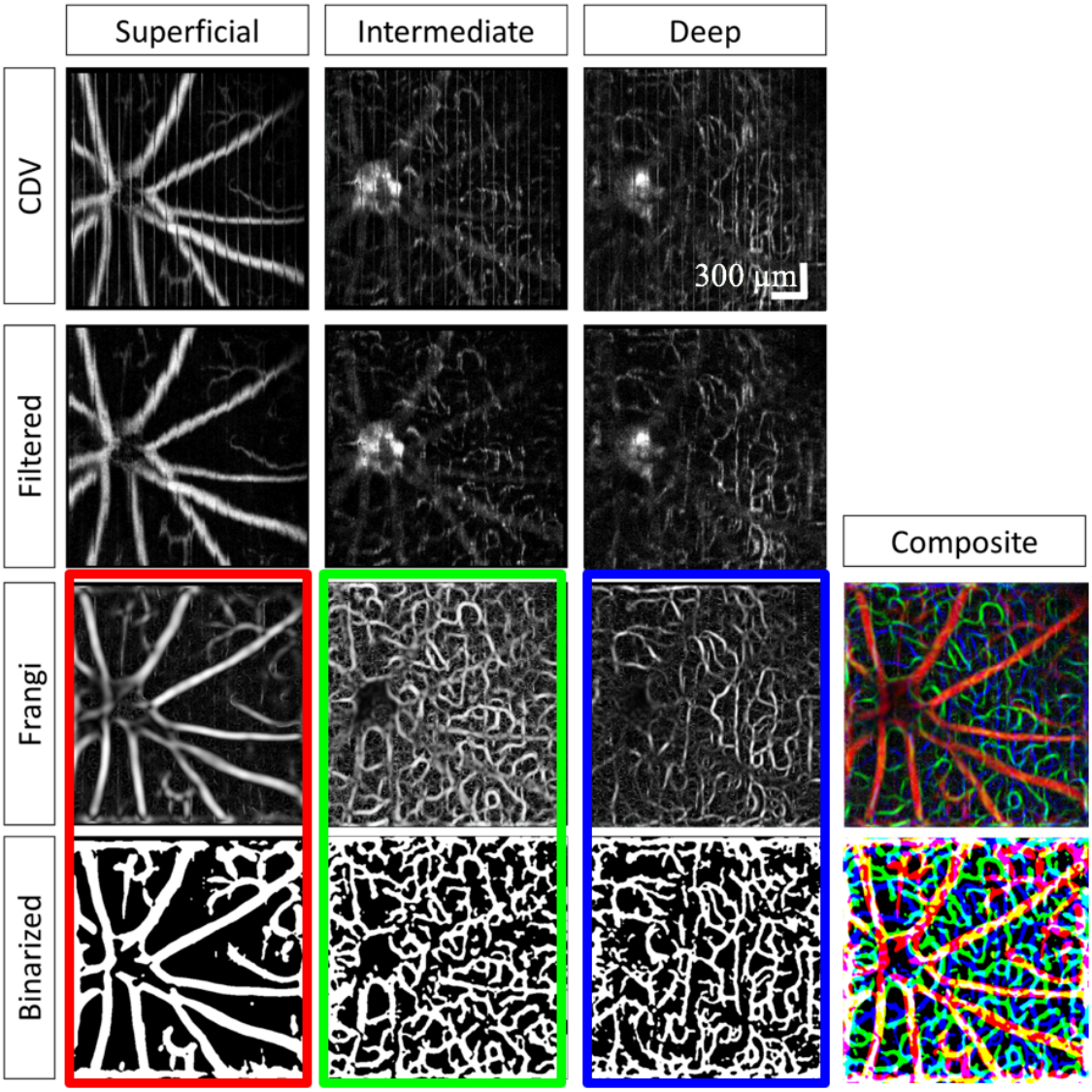

Figure 3.4: CDV angiography images (row 1) are manually filtered to remove bulk motion artifacts due to breathing and heart beat (row 2). A Frangi vesselness filter is then applied to improve SNR (row 3). Lastly, the Frangi-filtered images are binarized using adaptive filtering (row 4). Columns 1-3 show different vascular plexuses, and column 4 shows composite images of the Frangi-filtered and binarized angiograms. Scale bars indicate 300 μm.

Segmentation

Retinal segmentation is a requirement for conducting almost any sophisticated analysis of the retina for detecting disease states using OCT images. The thicknesses of various retinal layers are known to have widespread clinical significance. For example, the thickness of the retinal nerve fiber layer (RNFL) is reduced in multiple sclerosis (MS) patients, and especially in MS patients with a history of optic neuritis.[96] The RNFL is also a well-established indicator of glaucoma: the thickness of the RNFL decreases before visual field loss,[97]–[100] before the onset of optic nerve head defects,[101], [102] and with ocular hypertension.[103] RNFL thickness is also reduced in AD patients,[104], [105] and PD,[106], [107] but is elevated in Leber's hereditary optic neuropathy.[108]

Beyond layer thicknesses, there are layer-specific physiological changes that might be observed with SAR-OCT. Specifically, if shifts in mitochondrial dynamics are large enough to be detectable using SAR-OCT, it is expected that those changes would occur in layers that are rich in mitochondria—layers distinguished by the increased density of synapses, like the inner plexiform layer and the outer plexiform layer. The physiological importance of different retinal layers is described more fully in the introduction to Chapter 4.

Moreover, retinal segmentation is also key in determining the relative changes in scattering angle of particular retinal layers compared to other retinal layers.

Furthermore, murine ocular vasculature is generally isolated to three retinal layers: superficial vasculature in the RNFL and the ganglion cell layer (occasionally divided into two layers: radial parapapillary capillary plexus and superficial vascular plexus), intermediate vasculature at the boundary of the inner plexiform layer and the inner nuclear layer, and deep vasculature at the boundary of the inner nuclear layer and the outer

plexiform layer (Figure 3.5).[109] Any meaningful analysis of vasculature in mice necessitates proper retinal layer segmentation.

Thus, it has been illustrated that to conduct worthwhile retinal analysis, retinal segmentation is required.

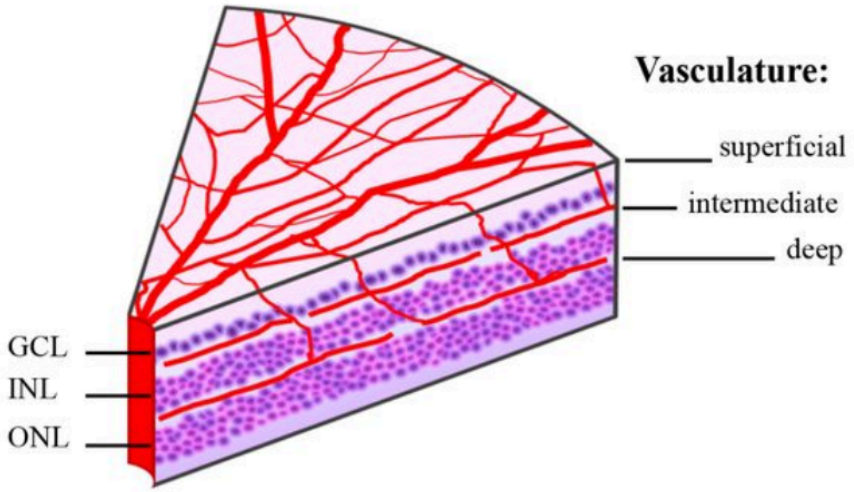

Figure 3.5: Red segments represent the location of vasculature. There are three vascular plexuses that can be isolated in specific retinal layers: then RNFL (superficial), the outer plexiform layer (intermediate), and the inner plexiform layer (deep). The retinal layers between the vascular plexuses are indicated on the left (GCL – ganglion cell layer, INL – inner nuclear layer, ONL – outer nuclear layer). This diagram of a mouse retina is taken from Ivanova.[109]

Previous Segmentation Algorithms

While human retina segmentation algorithms are numerous, only a handful of rodent retinal segmentation algorithms have been reported. These include a 3D segmentation algorithm for two boundaries,[110] a two-algorithm method that includes iterative refinement for three boundaries,[111] an active contours approach for six

boundaries,[112] a machine learning/graph-based method for ten boundaries,[113] and a sparsity based denoising/support vector machines/graph theory/dynamic programming approach for nine boundaries.[114]

While these methods reportedly segment murine retinal layers for various disease and non-disease states, no open source retinal segmentation algorithm was found that could successfully and repeatedly segment the retinal layers of mice imaged with the SAR-OCT system described in the previous chapter. Thus, a new approach was designed.

New Segmentation Algorithm

The murine retinal segmentation algorithm for the SAR-OCT images used in this dissertation can be summed up in three kinds of processes interspersed throughout the algorithm: (1) stack conditioning, (2) Sobel edge detection, and (3) error removal, each custom-designed in MATLAB.

As a part of the stack conditioning process, the angiography and intensity scans are simply summed. Because the vasculature of the murine retina is highly localized to particular regions, the addition of the SAR-OCT intensity volume with the angiography image intensifies the boundaries between retinal layers.

Another part of the stack conditioning process occurs after the ONL/RPE boundary is found. The retina is flattened with reference to the ONL/RPE boundary. Then, a median filtered is applied with the size of 50 x 50 x 1 (voxels, xyz). Because the retina has been flattened, this process works to provide some uniformity within each layer and make the layers more distinct.

The second category of segmentation processes is edge detection. Each boundary is determined by examining volumes that have been filtered with a Sobel edge detection filter.[115] The Sobel filter has a convolution kernel given by:

$$\begin{bmatrix} -1 & -2 & 1 \\ 0 & 0 & 0 \\ 1 & 2 & 1 \end{bmatrix}.$$

The ONL/RPE boundary is, for the most part, the most prominent edge detected by the Sobel edge filter. However, spurious noise could also be detected by the filter, so a secondary means of eliminating wrong boundaries was employed. Before the edge is selected by the MATLAB script, the user of the script must manually click throughout the image over several boundaries as prompted by the script. The user input is used as an initial guess for boundary detection; that is, boundaries are only considered as the possible correct boundary if they are within a physiologically reasonable range of the inputted boundary. This clicking technique is applied only to three of the five boundaries detected: the ONL/RPE boundary, the INL/OPL boundary, and the vitreous/ILM boundary.

Finally, the inputs of these user inputs are also used to form a 3D second-order polynomial that is utilized in the third processing step, error removal. It occasionally occurs that the edge selected by the MATLAB script is not the correct edge, and, perhaps the edge is not even reasonably determinable by the human eye. In such cases, it can be easily imagined where the edge is based on the surrounding tissues (e.g. under vessel shadows). In these cases, the 3D polynomial is manually selected (in those regions alone) to replace the semi-automatically detected edges. Example edge detection results may be see in Figure 3.6.

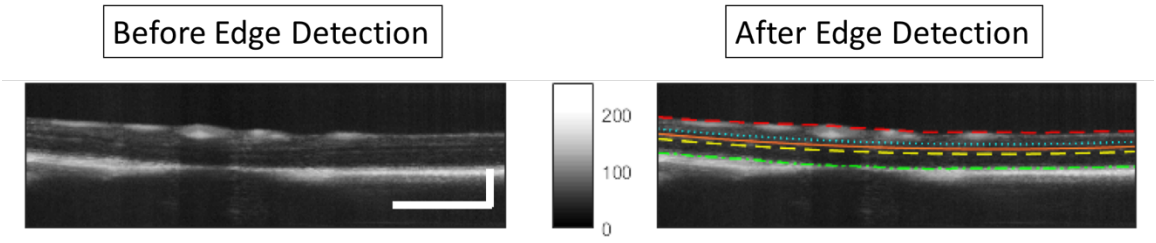

Figure 3.6: The left image is segmented, and the boundaries on the right. The boundaries displayed are the vitreous/ILM, IPL/INL, INL/OPL, OPL/ONL, ONL/RPE boundaries. Scale bars represent 300 μm.

ANALYSIS FOR FEATURE EXTRACTION

Scattering Angle

Scattering angle analysis using SAR-OCT can offer some insight into the bulk scattering properties of the tissue for each voxel, but it is important to design a feature that will leverage the utility of the optical design, considering the morphological changes in a given retinal pathology.

Ratiometric Feature

Ratio processing is the simplest approach, and is the approach previously described by Wang et al.[31] Wang looked to pathlength 3 as it contains the highest possible scatterers and found that the ratio of pathlength 1 to pathlength 3 (L/H_3) correlated with known azimuthal variation of retinal ganglion cell size.

However, as was demonstrated in the Monte Carlo simulation in Chapter 3, it is actually pathlength 2 and pathlength 1 that give the greatest angular discrimination. Although pathlength 3 contains higher backscattering angles than pathlength 2, pathlength 3 also contains the lowest possible angles (direct backscattering). Thus, L/H_2 was decided

upon as an image feature. A visual explanation of the PME and L/H_2 is provided in Figure 3.7.

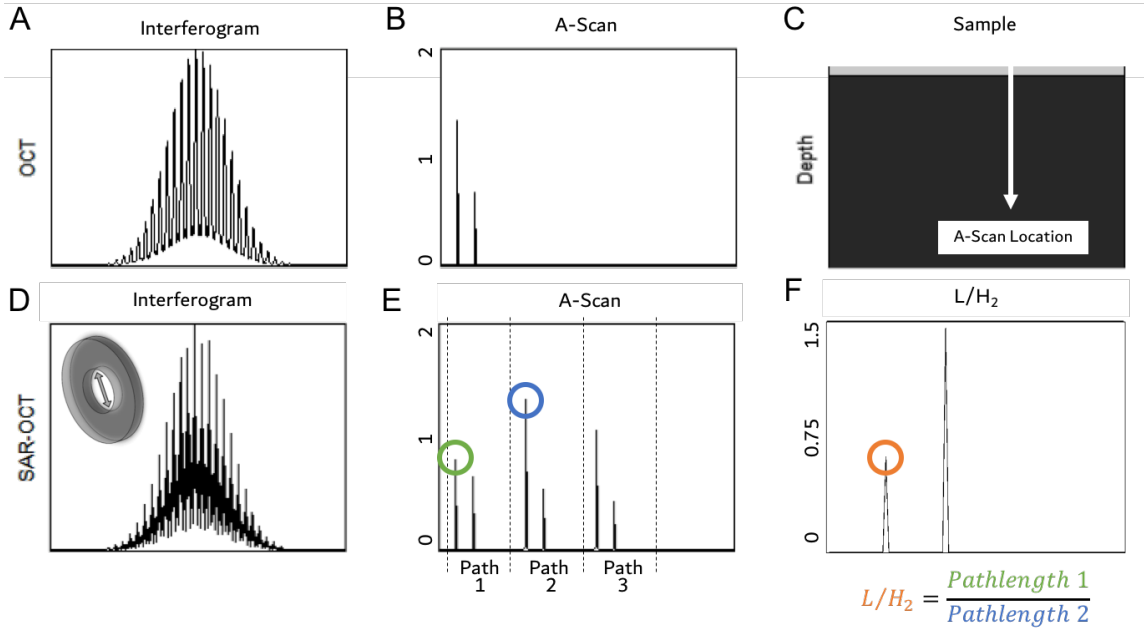

Figure 3.7: (A) shows a standard interferogram resulting from the a-scan in the sample (C). (B) shows the FFT of the interferogram; the peaks indicate the changes in refractive index that result in backscattering. (D) shows how the interferogram changes with the introduction of a PME, and (E) shows the effect on the resultant a-scan. Finally, (F) shows how L/H_2 is calculated for the a-scan.

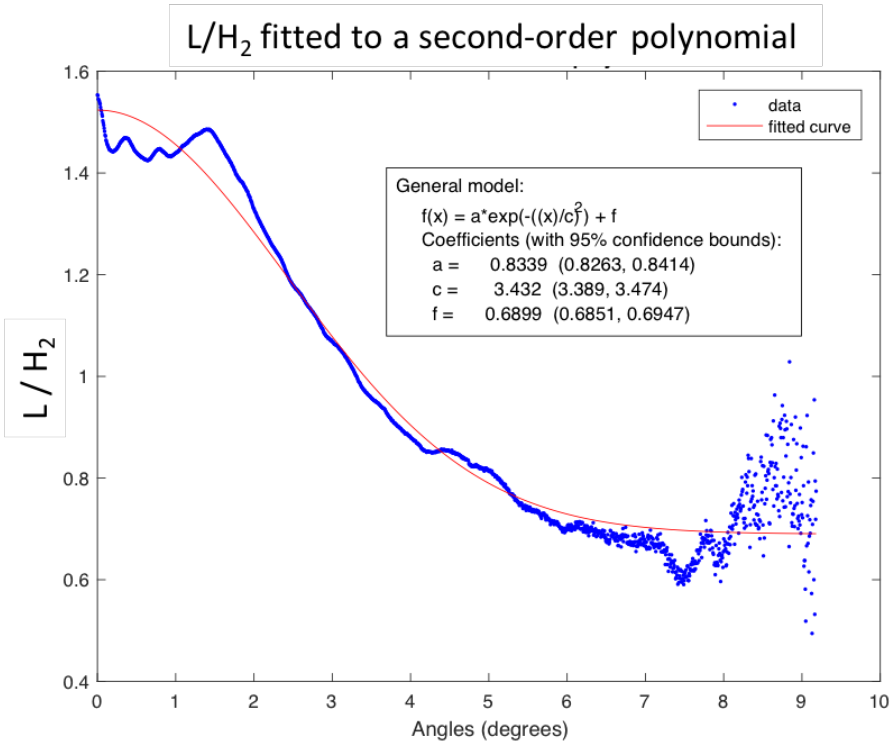

Figure 3.8: L/H_2 is plotted versus the backscattering angle. This plot shows that angular discrimination is possible out to 8 degrees. The limit of the fit of L/H_2 at Angle = ∞ is 0.69.

Now that L/H_2 has be decided upon as an image feature, it is important to revisit the experiment described in Chapter 2 (Figure 2.8-2.10) which supported the claim that backscattering angles up to eight degrees are recorded by the SAR-OCT system. Specifically, all three pathlength intensities could be combined to yield a unique backscattering angle. The question now is: can only pathlengths 1 and 2 (excluding pathlength 3) yield the same specificity? Indeed, Figure 3.8 illustrates that L/H_2 satisfies the demands of a good SAR-OCT image feature; pathlengths one and two may be combined to yield a single backscattering angle based on the fitted second-order polynomial.

To obtain a L/H_2 tomogram, pathlength 1 and pathlength 2 are divided at every x, y, and z position. With this approach, the segmentation output can be superimposed on the volume to sort the L/H_2 values of the retina into their corresponding layers (Figure 3.9). Comparing the L/H_2 values for particular retinal murine retinal layers will be explored further in Chapter 4.

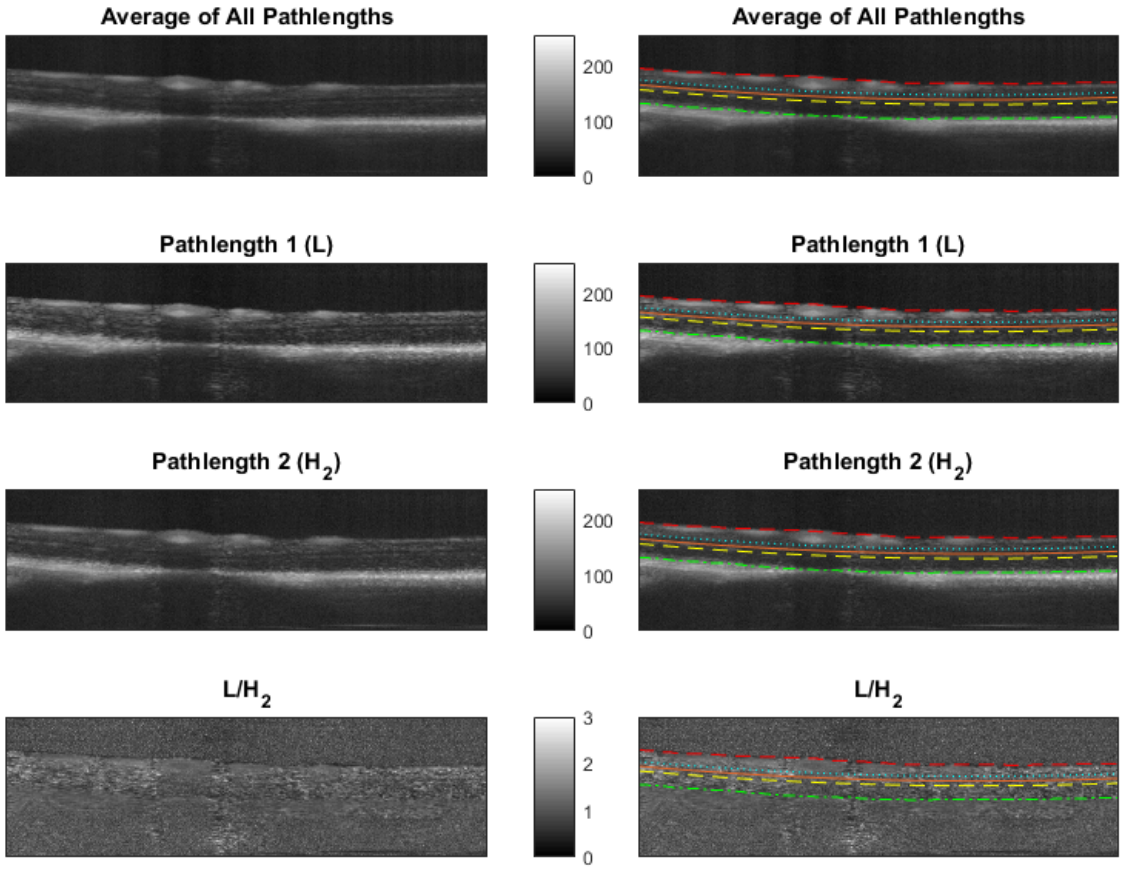

Figure 3.9: L/H_2 is the ratio of pathlength 1 and pathlength 2. The segmented retinal layers can be superimposed on L/H_2 to identify morphological edges native to the retina. Some layered differences are observed in L/H_2.

Burr Distribution

In order to better capture the utility of the L/H_2 ratio, the ratios for various retinal segments (e.g. layers, quadrants, vasculature/non-vasculature regions) are analyzed altogether—as distributions instead of averages. It is imaginable that some disease state of the retina could produce an increase in both high-angle and low-angle voxels. In this case, the mean of the L/H_2 values wouldn't shift, but some parameter of the distribution would (e.g. standard deviation in the case of a Gaussian distribution).

The Burr Type XII distribution is used here to parameterize the distribution of L/H_2 values in any volumetric region of the murine retina. It was found that the distribution of L/H_2 values in the retina fit nicely to a Burr Type XII (or Burr) distribution.

The Burr Type XII distribution is a generalization of the Pareto distribution and the Weibull distribution and was first described by Singh and Maddala[116] who used it to fit a size distribution of incomes. It has also been reported in diverse fields such as failure analysis,[117] forestry (tree diameter),[118] and behavioral science (travel time reliability).[119]

The Burr distribution's probability density function is given by Equation 3.2:

$$PDF_{Burr}(x|\alpha, C, K) = \frac{\frac{KC}{\alpha}\left(\frac{x}{\alpha}\right)^{c-1}}{1+\left(\frac{x}{\alpha}\right)^{c}}, \tag{3.2}$$

where α is a scale parameter (in the x-dimension), C and K are shape parameters, and *x* is the value of the sample. The influence of α, C, and K parameters are demonstrated by Figure 3.10.

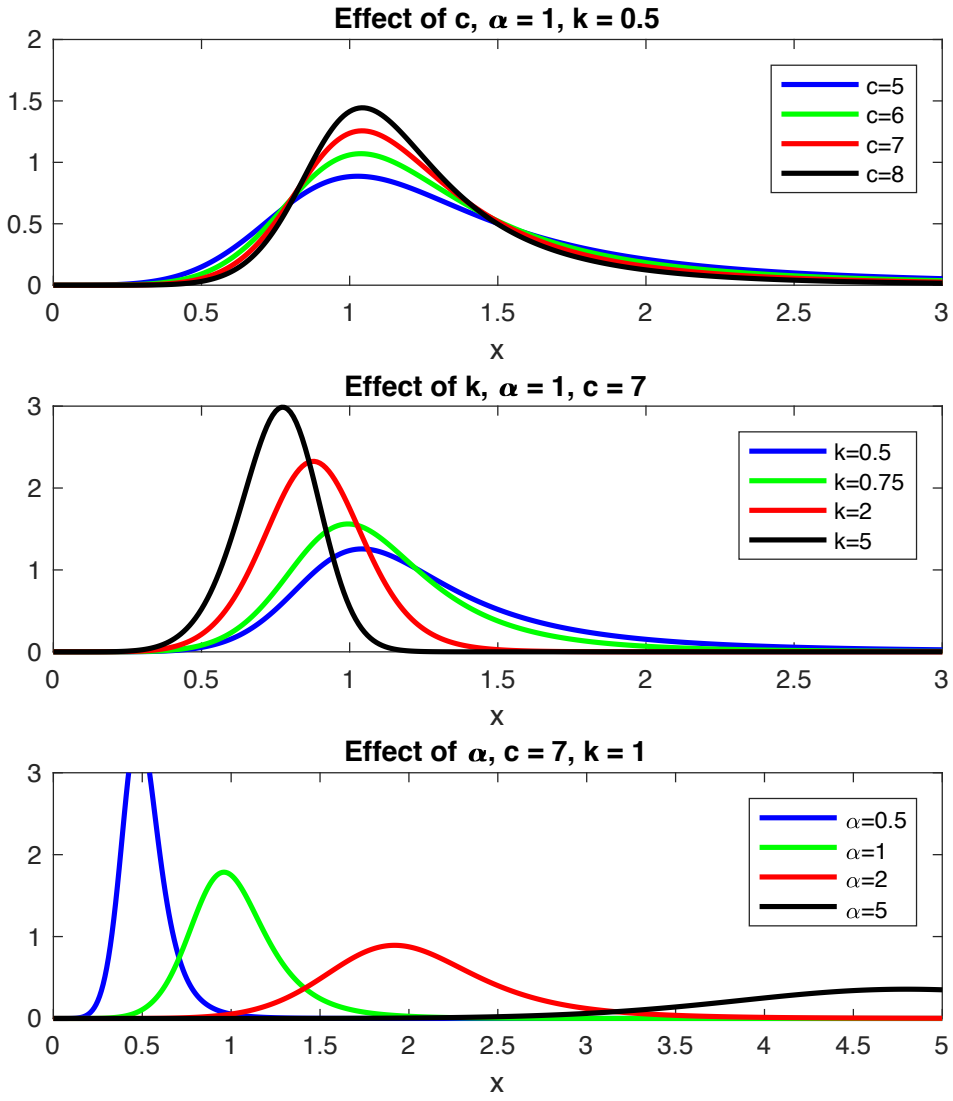

Figure 3.10: α is a parameter of the Burr Type XII distribution that controls scale in the x-dimension. C and K are parameters that control shape.

To demonstrate the goodness of fit of the Burr distribution to the L/H_2 values, the segmented inner nuclear layer of a mouse was chosen as a representative retinal volume. The L/H_2 values in the segmented inner nuclear layer were fit to a Burr distribution, and the resulting confidence intervals for the Burr distribution parameters were extremely tight. The α parameter was calculated to be 1.069 (confidence interval: [1.068, 1.071]), C

parameter as 5.315 (confidence interval: [5.303, 5.327]), and K parameter as 0.972 (confidence interval: [0.967, 0.977]). Thus, there is 95% confidence that the real value falls with 0.16% of α, 0.23% of C, and 0.55% of K. Expanded to each Burr distribution for every layer of a control mouse, on average there is 95% confidence that the real value falls within 0.43% of α, 0.58% of C, and 1.58% of K (Figure 3.11).

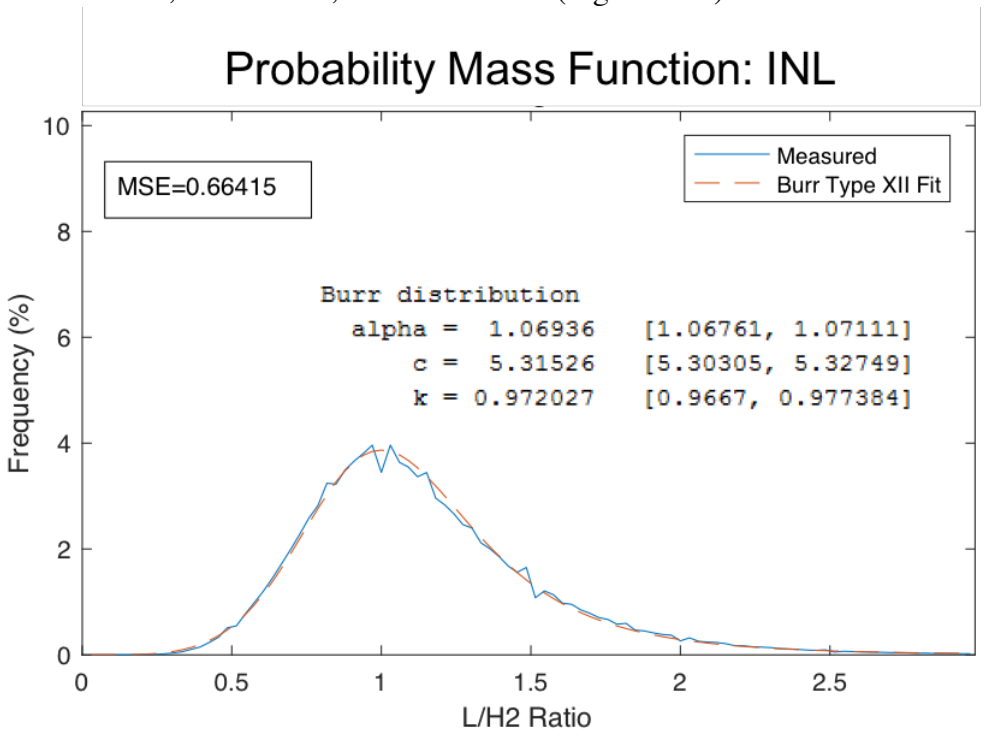

Figure 3.11: The probability mass function for the INL is displayed with the Burr distribution fit. The burr distribution is an excellent fit for L/H_2 values.

The Burr distribution parameters are examined throughout the remainder of the dissertation in in-vivo studies for various retinal layers, regions, and disease states.

Reflectance Index Analysis

Reflectance index has been previously shown to be an early marker of glaucoma in a primate and human study.[29], [30] The reflectance index is useful in that it can describe the attenuation properties of the RNFL, using the RPE as a means of normalization. This

removes the potential of attenuation changes anterior to the retina to affect analysis. The reflectance index is defined as:

$$RI(x,y) = \frac{I_{RNFL}(x,y)}{I_{RPE}(x,y)}, \tag{3.3}$$

where I is the intensity of the specified layer, and x and y are the lateral locations on the retina.

Because the lower boundaries of the RNFL and the retinal pigment epithelium (RPE) are not segmentable for the SAR-OCT setup, the RNFL is taken as the top ten pixels from the ILM, and the RPE is taken as the top ten pixels after the ONL/RPE boundary.

The reflectance indices in different regions of the retina are examined in the upcoming chapters on euthanasia and the murine model of AD.

Thickness Analysis

Thickness is examined simply as the distance between two boundaries. Several features can be extracted here using the segmented retina: thickness of the (1) RNFL + GCL + IPL, (2) INL, (3) OPL, (4) ONL, (5) total retinal thickness (RNFL-RPE). Furthermore, throughout the dissertation, these features are examined at various retinal regions as might be useful based on the experiment.

Angiographic Analysis

The final set of analysis that is performed on the processed images is angiography analysis, which can be divided into two categories: (1) volumetric blood flow (vessel density), (2) fractal analysis.

Vessel density, or "volumetric blood flow" as it is referred to in this dissertation, is simply the percentage of the tissue volume occupied by a blood vessel. For this dissertation, the binarized angiography images were used in this calculation:

$$Volumetric\ Blood\ Flow = \frac{number\ of\ white\ pixels}{total\ number\ of\ pixels}. \quad (3.4)$$

Similar measures have been used to distinguish between healthy and glaucomatous eyes in human patients in various retinal regions.[120]–[122] As some changes to vasculature in Alzheimer's disease patients and animal models have been noted (see Chapter 1), this imaging feature could offer important information about the murine retina.

A second feature that was examined with the binarized images was the fractal dimension. The fractal dimension provides a measure of how complex a geometrical pattern is. Fractal dimensions have been applied to OCT angiography images for retinal imaging,[123] as well as other retinal imaging modalities,[123] and non-biomedical applications such as geological survey.[124]

The fractal dimension is calculated for each vascular plexus using the box counting method[125] and is examined in the final chapter for analyzing the murine model of AD.

PART 2: IN-VIVO STUDIES AND CONCLUSIONS

Chapter 4: Scattering Property Variation in the Mouse Retina

The aim of this chapter is to demonstrate how SAR-OCT is sensitive to scattering changes in the murine retina by leveraging native differences between layers, vascular zones, and ocular regions in healthy mice. If native scattering differences between retinal layers can be detected with SAR-OCT, then a stronger case is made for SAR-OCT as a tool for monitoring scattering angle changes for disease states.

INTRODUCTION

Native scattering properties of the retina are not widely reported in the scientific literature. However, some preliminary work was previously reported using SAR-OCT for human retinal imaging by Wang who reported regional variation of backscattering angles in healthy human retinas.[31] A low/high ratio was developed, where low-angle backscattering was between 0-0.42 degrees, and high-angle backscattering was between 0-1.26 degrees. The study reported more high-angle backscattering (low/high < 1) in the temporal region of the RNFL and more low-angle scattering (low/high > 1) in the nasal region of the RNFL across five subjects. RGC axons have smaller diameters in the temporal region, where higher-angle scattering was more prominent.[31] The study hypothesized that these native morphological difference contributed to the difference in backscattering-angle detected by the human SAR-OCT system.

While interesting and useful, the Wang study did not consider each layer of the retina individually—only the RNFL, and even then, the ratio was averaged over the entire depth of the RNFL at every en-face location.

There remains a gap in the retinal imaging literature to characterize and quantify native retinal layers for healthy subjects in terms of their scattering properties. The system

described in Chapter 2 is used here to leverage backscattering-angle discrimination, and retinal layers are analyzed individually. Differences in scattering-angles between vascular and non-vascular zones are also explored, along with difference across retinal quadrants.

METHODS

Overall, twenty healthy murine retinas are imaged using the SAR-OCT system, and the scattering properties of each layer, region, and vascular zone are reported. The Burr Type XII distribution of pathlength ratios is utilized as a tool for characterizing scattering properties for each of these variables.

Mouse Handling

The twenty healthy mice (B6SJL F1/J—JAX #100012) imaged in this study (IACUC protocol #AUP-2015-00156) ranged in age from 6-10 weeks. Each mouse was anesthetized first in an induction box (5% isoflurane), and then moved to the imaging platform where anesthesia continued via a custom nose cone (1.5-3% isoflurane). The left retina was imaged by the SAR-OCT system for about 15 minutes, and then the mouse was allowed to recover. Overall, the experiment lasted around 30 minutes per mouse.

Image Processing

Past published work by Wang for SAR-OCT has utilized a ratio of pathlength 1 and pathlength 3 (L/H_3).[31] However, as was noted in Chapter 2, pathlengths 1 and 2 give the greatest angular discrimination because pathlength 3 includes both high and low-angle backscattered light. Therefore, for this work, a ratio of pathlength 1 and pathlength 2 is used (L/H_2, that is "low" / "high – from pathlength 2"). Whereas Wang previously reported a mean of L/H_3 for the entire thickness of the retina at every lateral position, here I report voxel-by-voxel analysis of the entire retina via the Burr distribution (Chapter 3).

Image Features

To determine if the Burr parameters could distinguish between retinal layers, a one-way multivariate analysis of variance (MANOVA) was performed using α, C, and K as the related dependent variables and the layer as the independent variable. The null hypothesis for a one-way MANOVA is that any difference observed in the α, C, or K is due to random chance, not differences in retinal layer.

To determine if the presence or absence of vasculature could explain a difference in means, the binarized vasculature images (Chapter 4) were used to categorize every L/H_2 voxel in the RNFL, IPL, and OPL as either being vascular or non-vasculature. Then, these collections of L/H_2 values were fit to the Burr Type XII distribution and compared layer-wise. A one-way MANOVA tested the null hypothesis that any difference observed in the α, C, or K is due to random chance, not differences in vascularization (presence or absence of blood vessels). This test was performed three times, once for each of the vascular plexuses (superficial-RNFL, intermediate-IPL, and deep-OPL).

A series of paired t-test was performed to test the null hypothesis that the difference in the parameters of the fitted Burr distribution between central and peripheral sections for each quadrant (superior, nasal, inferior, and temporal) and for each retinal layer grouping (superficial, intermediate, and deep) was normally distributed about zero.

RESULTS

Layer-wise Analysis

Table 4.1 shows the mean α, C, and K parameters of the Burr Type XII fit to L/H_2 values, organized by layer, vascular zone. A one-way MANOVA test including all three Burr parameters indicated that the space containing the means is two-dimensional. That is, the null hypothesis can be rejected ($p<0.001$). The second p-value, 0.032, also casts doubt

on the hypothesis that the group means lie on a space of 1 dimension. Figure 4.1 shows a grouped scatter plot for this layer-wise one-way MANOVA analysis. The RPE is clearly distinguishable using canonical variable 1. Canonical variable 2 begins to distinguish between other layers. Canonical variables are the product of a calculated Eigen vector and the independent variables' minus their means. Canonical variables may be thought of as principal components for categorical data.

		VASCULAR			NON-VASCULAR			COMBINED		
Retinal Layer	Parameter:	**α**	**c**	**k**	**α**	**c**	**k**	**α**	**c**	**k**
RNFL	**Average**	1.18	5.03	1.21	1.18	4.05	1.23	1.18	4.35	1.23
	St. Dev.	*0.02*	*0.60*	*0.08*	*0.05*	*0.22*	*0.05*	*0.04*	*0.30*	*0.03*
GCL	**Average**				1.19	4.63	1.15			
	St. Dev.				*0.04*	*0.43*	*0.09*			
IPL	**Average**	1.18	5.00	1.07	1.20	4.45	1.17	1.19	4.66	1.14
	St. Dev.	*0.05*	*0.54*	*0.12*	*0.05*	*0.41*	*0.09*	*0.05*	*0.46*	*0.10*
INL	**Average**				1.11	4.83	1.11			
	St. Dev.				*0.04*	*0.42*	*0.12*			
OPL	**Average**	1.12	5.23	1.07	1.10	4.72	1.11	1.11	4.88	1.11
	St. Dev.	*0.06*	*0.21*	*0.12*	*0.06*	*0.38*	*0.14*	*0.07*	*0.32*	*0.15*
ONL	**Average**				1.09	4.64	1.14			
	St. Dev.				*0.06*	*0.38*	*0.10*			
RPE	**Average**				1.05	9.68	1.08			
	St. Dev.				*0.03*	*0.69*	*0.19*			

Table 4.1: The mean Burr distribution parameters are shown here for 20 mice. Color intensity represents magnitude of the value.

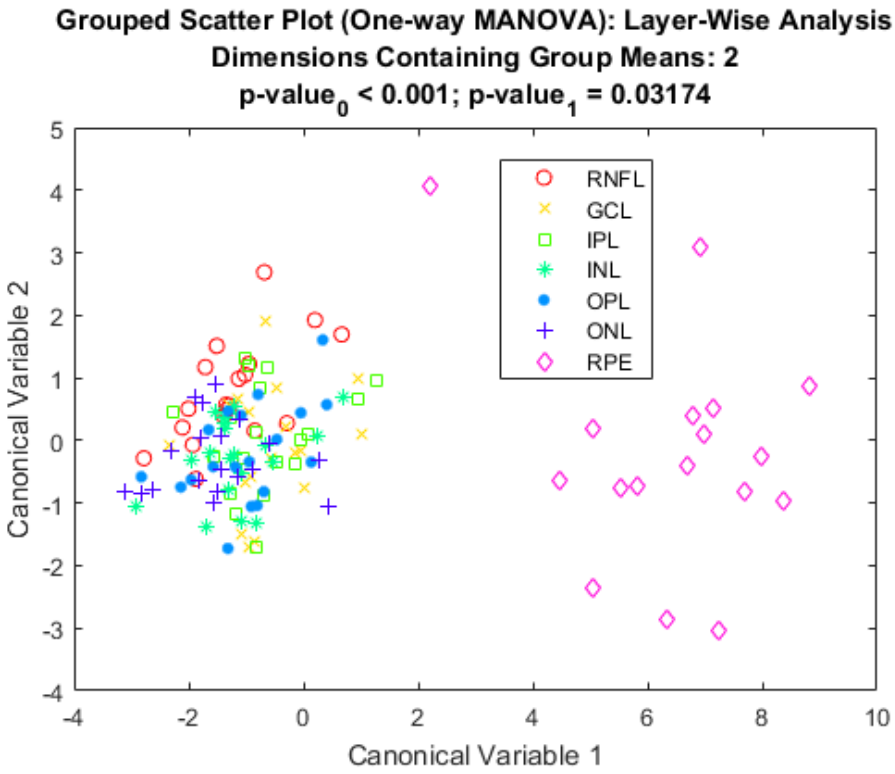

Figure 4.1: A grouped scatter plot that plots the first two canonical values against one another demonstrates the two-dimensional plane on which the group means lie. The RPE is clearly distinguished from the other layers by the first canonical variable. The other layers are approaching separation using canonical variable 2. The RNFL has generally higher values than the ONL, for example.

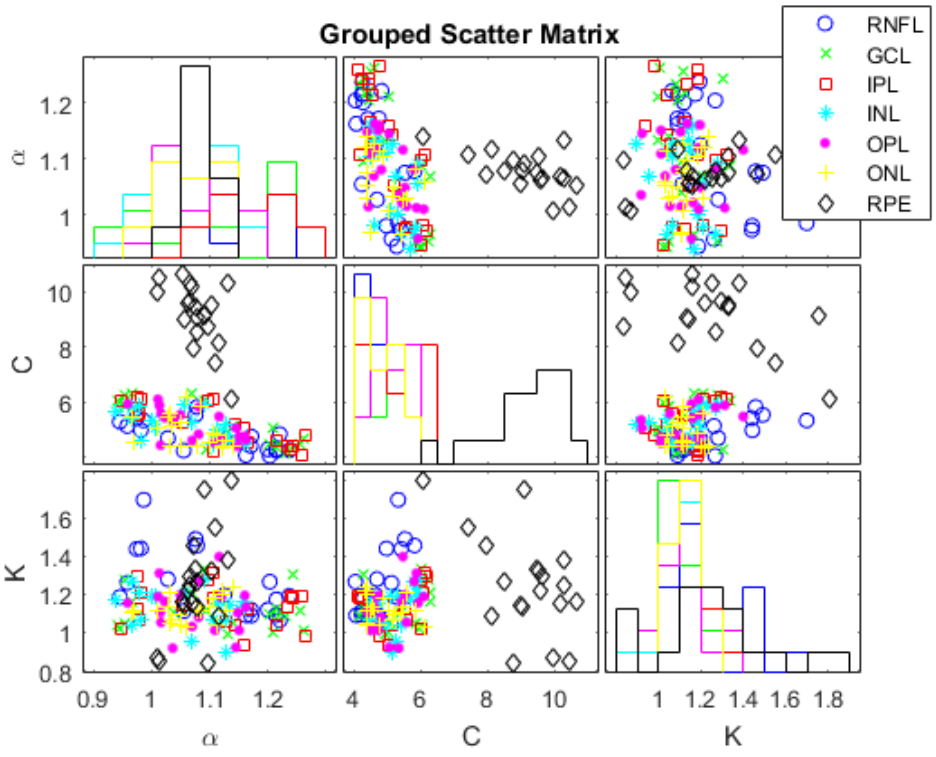

Figure 4.2: A grouped scatter matrix for α, C, and K show that most of the distinguishing power between layers is coming from the C parameter.

A grouped scatter plot reveals that most of the signal is coming from the C parameter (Figure 4.2). However, because the results of the one-way MANOVA test revealed that the group means are on a two-dimensional space, there is some imperceptible value to α and K. To clarify the added value of α and K, the retinal layers were grouped into three layers (1. superficial = RNFL + GCL + IPL; 2. intermediate = INL + OPL + ONL; and 3. the RPE) and a one-way MANOVA test was repeated. The results of the second one-way MANOVA test are presented in Figure 4.3. Figure 4.4 shows that each retina layer grouping may be distinguished by two canonical variables.

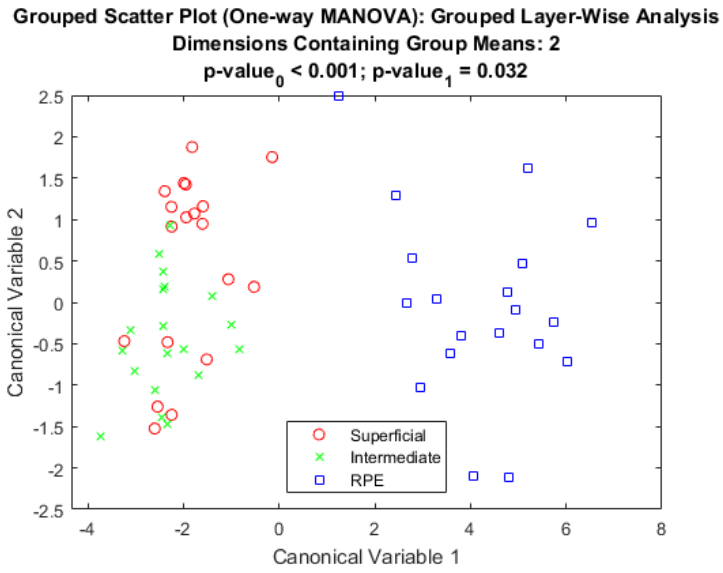

Figure 4.3: A grouped scatter plot for grouped retinal layers (superficial, intermediate, RPE) shows more apparent distinction between the superficial and intermediate layers for canonical variable 2 when compared to the scatter plot for no retinal layer groupings (Figure 4.1).

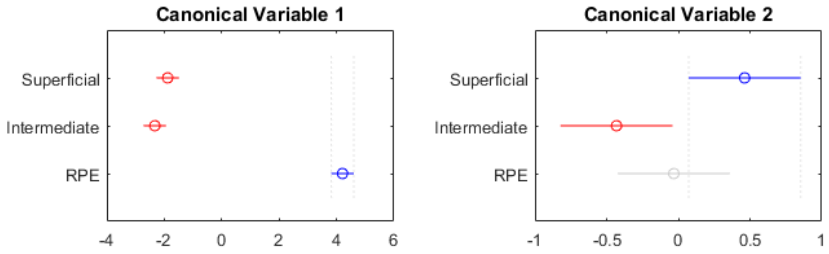

Figure 4.4: Canonical variable 1 distinguishes between the RPE and the other two layer groupings. Canonical variable 2 distinguishes between the superficial and intermediate retinal layer groupings. Bar widths indicate confidence intervals.

Taken altogether, it may be said that the three retinal layer groupings—superficial, intermediate, and deep—are distinguished by their scattering properties, namely the distributions of their L/H_2 values.

Vascular Analysis

The results of the one-way MANOVA for the superficial vascular plexus in the RNFL rejected the null hypothesis that there are no differences in α, C, and K explained by vascularization ($p<0.001$). The multivariate means lie on the same line; that is, vascularization can be described by one canonical variable (Figure 4.5(A)). While the C parameter is sufficient to explain the difference (Figure 4.5(B)), canonical variable 1 is more effective at explaining differences in the groups.

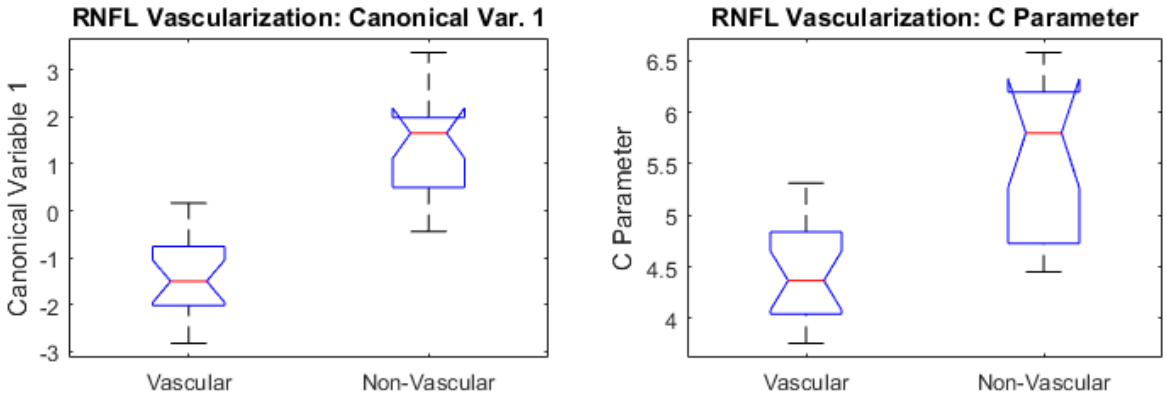

Figure 4.5: The first canonical variable yielded by one-way MANOVA better explains the differences in vascular and non-vascular regions of the RNFL when compared to the C parameter alone. T-test p-values are p=0.0046 (Canonical Var. 1) and p=0.0801 (C Parameter).

Concerning the intermediate vascular plexus in the IPL, the canonical variable yielded by one-way MANOVA was sufficient in explaining the difference between IPL vascular and non-vascular zones (t-test between vascular and non-vascular regions, p=0.0046; Figure 4.6(A)). The C parameter alone does not allow for rejecting a t-test null hypothesis (p=0.0801; Figure 4.6(B)).

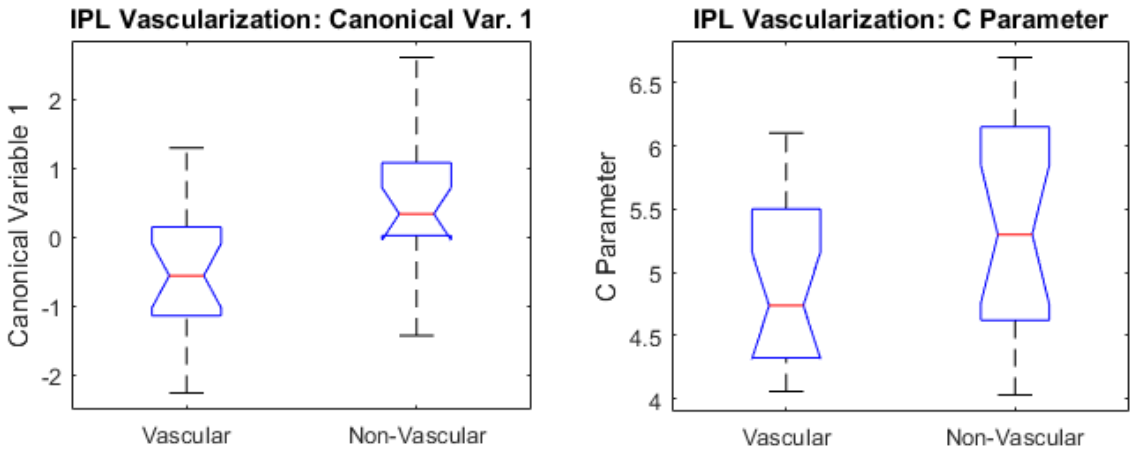

Figure 4.6: The first canonical variable yielded by one-way MANOVA explains the differences in vascular and non-vascular regions of the IPL (p=0.0046). The C parameter alone does not explain difference in vascular and non-vascular regions (p=0.0801).

In the deep vascular plexus (OPL), both the canonical variable (one-way MANOVA) and the C parameter explained the difference between vascular and non-vascular regions of the OPL (t-test, p<0.001; t-test, p=0.0147; Figure 4.7).

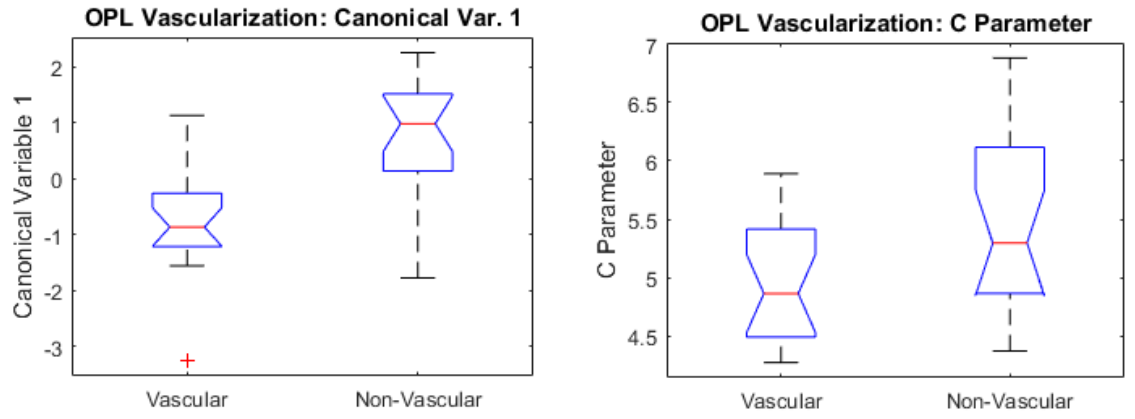

Figure 4.7: The first canonical variable yielded by one-way MANOVA explains the differences in vascular and non-vascular regions of the OPL (t-test, p<0.001). The C parameter also explains the difference in vascular and non-vascular regions (t-test, p=0.0147).

Regional Analysis

The series of t-tests indicated that for the superficial and intermediate retinal layer groupings, the C parameter value of the central sections for each quadrant was statistically different from those of the peripheral quadrants. For each quadrant in the superficial and intermediate layers, the C parameter was greater in the central section of the quadrant than it was for the peripheral section of the quadrant. This pattern did not hold for the deep retinal layers; for the deep layers, there was either no significant differences, or the difference was reversed (C parameters greater in the periphery). Figure 4.8 illustrates the differences in central and peripheral values of the C parameter.

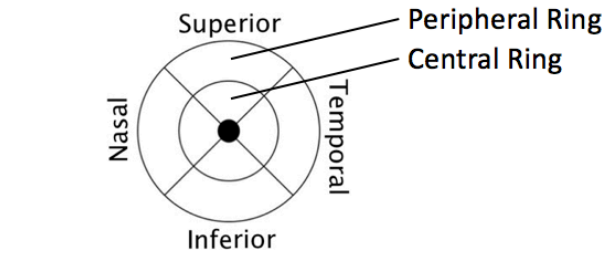

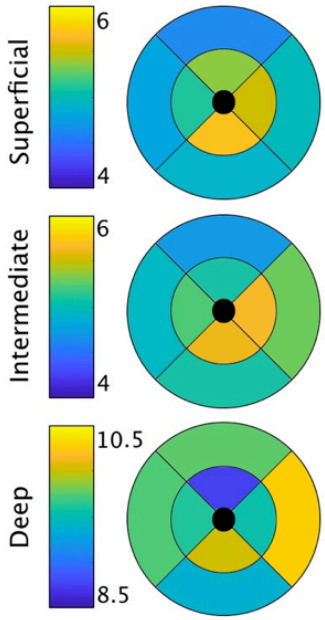

Quadrant	Central (In)	Peripheral (Out)	Confidence Interval (In-Out)	Paired t-test p-value
Superior (n=15)	5.350 (±0.46)	4.638 (±0.53)	[0.52, 0.90]	<0.001
Nasal (n=16)	5.124 (±0.65)	4.790 (±0.68)	[0.12, 0.56]	0.007
Inferior (n=9)	5.717 (±0.53)	4.915 (±0.52)	[0.57, 1.03]	<0.001
Temporal (n=11)	5.516 (±0.57)	4.992 (±0.43)	[0.27, 0.78]	0.001

Quadrant	Central (In)	Peripheral (Out)	Confidence Interval (In-Out)	Paired t-test p-value
Superior (n=15)	5.094 (±0.54)	4.743 (±0.50)	[0.19, 0.51]	<0.001
Nasal (n=16)	5.230 (±0.59)	4.938 (±0.49)	[0.19, 0.39]	<0.001
Inferior (n=9)	5.614 (±0.58)	5.076 (±0.60)	[0.36, 0.72]	<0.001
Temporal (n=11)	5.640 (±0.70)	5.300 (±0.62)	[0.16, 0.52]	0.002

Quadrant	Central (In)	Peripheral (Out)	Confidence Interval (In-Out)	Paired t-test p-value
Superior (n=15)	8.776 (±1.38)	9.765 (±1.06)	[-1.35, -0.62]	<0.001
Nasal (n=16)	9.613 (±1.12)	9.733 (±1.50)	[-0.64 – 0.40]	0.628
Inferior (n=9)	10.028 (±1.15)	9.404 (±1.59)	[-0.52 – 1.77]	0.246
Temporal (n=11)	9.547 (±0.91)	10.255 (±0.74)	[-1.4, 0.01]	0.047

Figure 4.8: For superficial and intermediate retinal layer groupings, the central section of each quadrant has a greater C parameter value than the C parameter values of their corresponding peripheral sections. This pattern generally did not hold for the deep layers of the retina.

There were no statistically significant differences between the quadrants when α, C, and K were transformed to canonical variables using the Eigen vector from grouped retinal layer analysis above.

DISCUSSION

Layer-wise Analysis

As was discussed in the introduction to the dissertation, the retina is known to have morphological shifts as a function of layer. The RPE seems to be very unique in its scattering properties, with more uniform scattering angles (higher C parameter, narrower L/H_2 distribution). Indeed, of all the retinal layers, the RPE might be said to be the most morphologically uniform. In fact, the utility of the attenuation coefficient feature in distinguishing between normal and glaucomatous eyes in another study assumes the scattering uniformity of the RPE.[126] The C parameter sufficiently distinguishes between the RPE and the more superficial layers likely due to the RPE's uniformity.

In contrast to the RPE, the superficial and intermediate layers are not distinguished by the C parameter (i.e. narrowness/broadness in the distribution of L/H_2distribution), but instead by a canonical variable output by one-way MANOVA. It is difficult to untangle here the contribution of α and K parameters and draw conclusions about the anatomical differences between the more superficial layers of the retina.

Vascular Analysis

Zones identified as vascular are those areas within a vascular plexus where there is blood flow, indicated by the angiographic processing. These regions are binarized and used as a mask for the vascular analysis of Burr distributions. Because each B-scan is averaged 8 times to get the intensity OCT image, the scattering profiles of red blood cells and other moving scatterers is likely creating a higher probability of the L and H_2 paths being balanced (higher C parameter). Indeed, this is what is observed using SAR-OCT, however more experiments could be designed to verify this phenomenon.

Regional Analysis

The density of all major retinal cell types in the murine retina is known to be higher in the regions closest to the optic nerve head (Figure 4.9).[127], [128] The increased density of retinal cell populations and decreased cell size near the optic nerve head likely cause the distribution of L/H_2 values to be narrower.

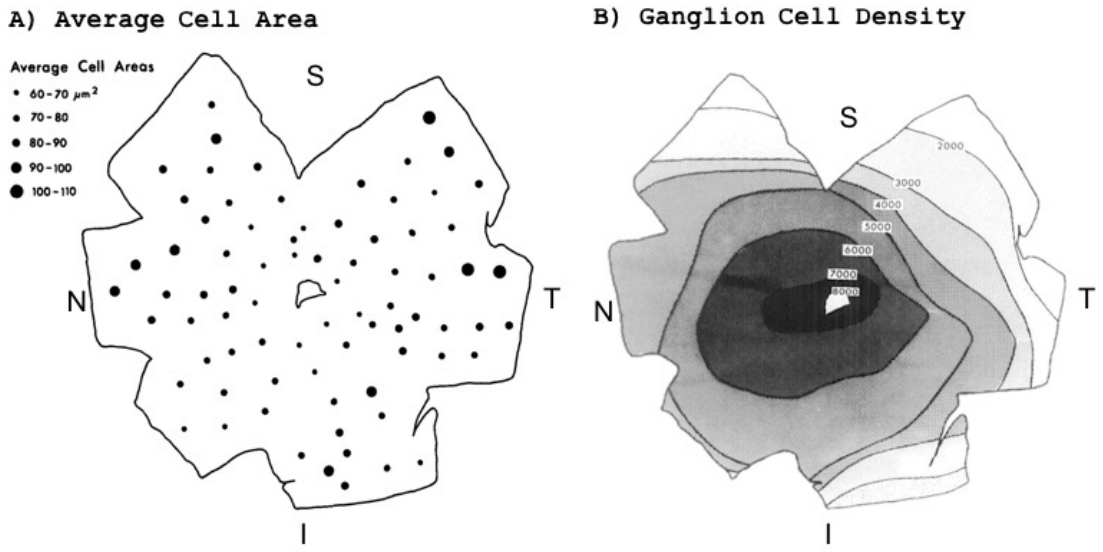

Figure 4.9: The average ganglion cell area is greater in peripheral regions (A), though the density of ganglion cells is greater near the mouse's ONH (B; units in mm^{-2}). Figure adapted from Drager.[127] While Drager only examined ganglion cells, Jeon demonstrated that the trend holds for all major cell populations in the murine retina.[128]

A higher C parameter indicates that there is a greater probability of light scattering from any given voxel such that light in the high angle pathlength and light in the low angle pathlength is about equal. In contrast, the peripheral segments of the retina scatter light with broader distributions. Specifically, a lower C parameter means that there is a greater probability (when compared to a higher C parameter) that light scatters such that the high

angle or the low angle scattered light is off-balance (i.e. the intensity of P1 or P2 is greater than the other).

It makes sense that light would scatter with more predictability as the density of cells increases and the volume decreases (towards the ONH). Fewer individual cellular components can project their distinct scattering profile onto the entire voxel when there are other scattering profiles superposed for the same volume. In contrast, as the density of cells decreases and the volume of the cell increases (towards the peripheral retina), individual scatterers (e.g. mitochondria) have more space to diffuse and are more likely to be one of fewer scatterers in any given voxel. Thus, the scattering profile of any scatterer can more easily dominate the scattering profile of the voxel. If a scatterer in a low-density, high cell-volume area of the retina has a scattering profile that would contribute to a low L/H_2 value for that voxel, it is less likely that this scattering profile would be affected by other scatterers contained in this low-density, high cell-volume voxel than the scattering profile would be affected for a high-density, low cell-volume area.

It should lastly be acknowledged that because the murine retina differs from the human retina in that it does not have a fovea, the kind of parapapillary variation seen in the RNFL by Wang[31] is not expected here; indeed, that variation was not seen.

The findings of this study demonstrate the capacity of SAR-OCT to offer an additional contrast mechanism for retinal imaging. Using the Burr distribution and the L/H_2 paradigm, SAR-OCT might be used to improve retinal segmentation algorithms or used to image mouse models with some hypothesized shift in scattering properties (e.g. neurodegenerative diseases).

CONCLUSION

Twenty mouse retinas were imaged using SAR-OCT, and it was demonstrated by fitting ratiometric data (L/H_2) to a Burr Type XII distribution that SAR-OCT is sensitive to scattering angle differences between retinal layers, vascularization zones, and retinal eccentricity.

Concerning retinal layers, a transformation of α, C, and K into a two-dimensional space via MANOVA created two canonical variables. The first canonical was shown to distinguish between the deep (RPE) and superficial (RNFL + GCL + IPL), and deep and intermediate (INL + OPL + ONL). The main contribution to canonical variable 1 was the C parameter, which was higher for the deep retina. It was hypothesized that the RPE was scattering in more predictable patterns, with high and low-angle backscattered balanced more often than in the superficial and intermediate layers. The second canonical variable could distinguish between the superficial and intermediate layers. The contribution of α and K were harder to extract and explain for this canonical variable.

Vascularization zones for each vascular plexus (superficial in the RNFL, intermediate in the IPL, and deep in the OPL) were selected using binarized angiography images. The vascular and non-vascular zones were shown to have significantly different C parameters for the superficial and deep layers, but not for the intermediate layers. A one-way MANOVA test produced a canonical variable that was mostly influenced by the C parameter, with some contribution from α and K. The first canonical variable for the vascular and non-vascular zones were shown to be significantly different for each of the three vascular plexuses. The vascular zones have obvious morphological differences when compared to other retinal tissue (red blood cells versus neurons). The increased homogeneity and motion of the vascular zones might explain why the C parameter of the

Burr distribution was elevated, indicating more homogenous scattering, or a blurred scattering profile in contrast to more disconnected profiles in non-vascular tissue.

Lastly, it was demonstrated for most layers that there is a shift in the C parameter with eccentricity—comparing the central retina scattering properties to the peripheral retina scattering properties. The C parameter was higher for the peripheral sections for each quadrant in both the superficial and intermediate retinal layers. The same pattern did not hold (and in fact was reversed for one quadrant) in the RPE. These scattering properties can be explained by the anatomical variation of cell volume and cell density in the retina.

Altogether, SAR-OCT has been demonstrated to be sensitive to scattering angle changes within the murine retina. Indeed, layers of the retina are distinguished by their scattering properties as seen in the canonical variables yielded by MANOVA. The exact scattering properties of the murine retina are largely unreported in the literature, and thus strong conclusions may not be drawn about what exactly the SAR-OCT data is indicating. Future studies should examine the morphological conditions of each retinal layer in order to explore the meaning of the SAR-OCT system. Additionally, future studies should work to verify the utility of SAR-OCT in cross-section and longitudinal studies of murine models of retinal diseases.

Chapter 5: Scattering Angle Changes During Euthanasia

In this chapter, my aim is to demonstrate the capacity of the SAR-OCT system to detect scattering angle changes in the murine retina given a hypoxic insult. There are known changes to scattering angle in necrotic tissues due to morphological changes such as cell membrane rupturing and mitochondrial fission. With this background, an experiment is conducted in which mice are euthanized via isoflurane overdose while the retina is imaged using the reported SAR-OCT system. The results validate the sensitivity of the system to scattering angle changes in longitudinal studies by demonstrating shifts in L/H_2 distributions and fluctuations in the reflectance index. Lastly, I discuss the limitations of the experiment and implications for subsequent studies.

INTRODUCTION

There is a rich publication record concerning angle-resolved imaging of apoptotic and necrotic tissues specifically. One study examined the changes in forward scattering (5-90 degrees) due to mitochondrial swelling due to oxidative stress in suspensions of intact murine mammary carcinoma cells and found that the treated cells scattered less light at low angles.[129] Similarly, another study reported an increase the ratio of high to low-angle light scattering (forward scattering) for induced mitochondrial fission.[130] However, two other studies involving the same authors indicated a decrease in the same ratio in apoptotic cells.[131], [132] In each case, the shifts in scattering angle were associated specifically with changes in mitochondrial morphology, supporting the importance of mitochondria in light scattering.[133] While several cell culture and ex-vivo tissue studies have been reported involving angle-resolved imaging, similar optical imaging techniques have not been extensively explored for retinal imaging.

In this chapter, the backscattering properties of the murine retina are examined using SAR-OCT. Using SAR-OCT, scattering properties of each layer of the murine retina may be studied for any state. A euthanasia experiment was designed to answer this question: Is there a detectable change in tissue scattering properties for the oxygen-deprived murine retina using the reported SAR-OCT system? To answer this question, six mice were euthanized by isoflurane overdose and their retina's imaged continuously during the hypoxic event. Four parameters were tracked through the experiment: (1) volumetric blood flow, (2) total retinal thickness, (3) reflectance index, and (4) parameters related to scattering angle detection.

METHODS

Animal Handling

This experiment (IACUC protocol #AUP-2015-00156) used six B6SJL F1/J mice from the Jackson Laboratory (JAX stock #100012) at age 10 weeks. Each mouse was initially anesthetized in an induction chamber (3% mg/kg isoflurane). Once the mouse was recumbent, it was gently removed from the chamber and placed in a secure stereotaxic mount where it continued to received anesthesia via a custom nose cone (isoflurane, 0.5 - 3%).

Then, the animal's left pupil was dilated with 1 drop of tropicamide (Mydrum®). Subsequently, the eye was covered with a drop of hydroxypropyl methylcellulose solution (Methocel® 2%) for index matching to the SAR-OCT system's objective, and the leading lens of the optical coherence tomography (OCT) imaging device was brought in contact with the mouse cornea. The right eye was also covered in hydroxypropyl methylcellulose solution to protect the cornea.

After establishing 10 – 20 minutes of baseline anesthetized murine retinal images with the SAR-OCT system (imaging at intervals of approximately 4 minutes), the isoflurane concentration was increased to 5% to initiate oxygen deprivation. Images were collected for approximately one hour after oxygen deprivation was initiated, well after the mouse had died and up until corneal clouding began to obscure the image quality. After the imaging procedure ended, its death was ensured via secondary euthanasia.

SAR-OCT Protocol

The SAR-OCT system collected fringe data with size 1492 pixels x 512 pixels x 4096 pixels (samples per a-scan, a-scans per b-scan, b-scans per c-scan). Each B-scan location was collected 8 times sequentially for angiographic analysis and averaging for improved SNR. After the FFT and pathlength alignment and averaging, the retina could be represented in a volume sized 150 x 512 x 512.

Image Analysis

Several changes were monitored for each mouse. The most pertinent features include (1) volumetric blood flow, (2) total retinal thickness, (3) reflectance index, and (4) parameters related to scattering angle detection. Each of these features is described below.

Volumetric Blood Flow

In order to identify the status of the mouse's condition (life or death), blood flow was monitored using CDV, the OCT angiography method described in chapter 4. For this experiment, the binarization algorithm was altered slightly from that described in chapter 4. Whereas the binarization process for living mice included an adaptive histogram equalization step to account for areas of decreased regional intensity, the binarization process for this euthanasia experiment did not include this adaptive filter. Instead, the parameters used for the adaptive histogram equalization were averaged over each mouse

in the pre-euthanasia stage of the experiment (before isoflurane overdose was initiated). These averaged parameters were subsequently "hard-coded" to make histogram equalization standard for each time point in the experiment. This removed the binarization algorithm's bias towards the presence of blood flow and enabled the comparison of early time points to late time points in the experiment (Figure 5.1). This "hard-coded" technique was reliable across each of the six experiments.

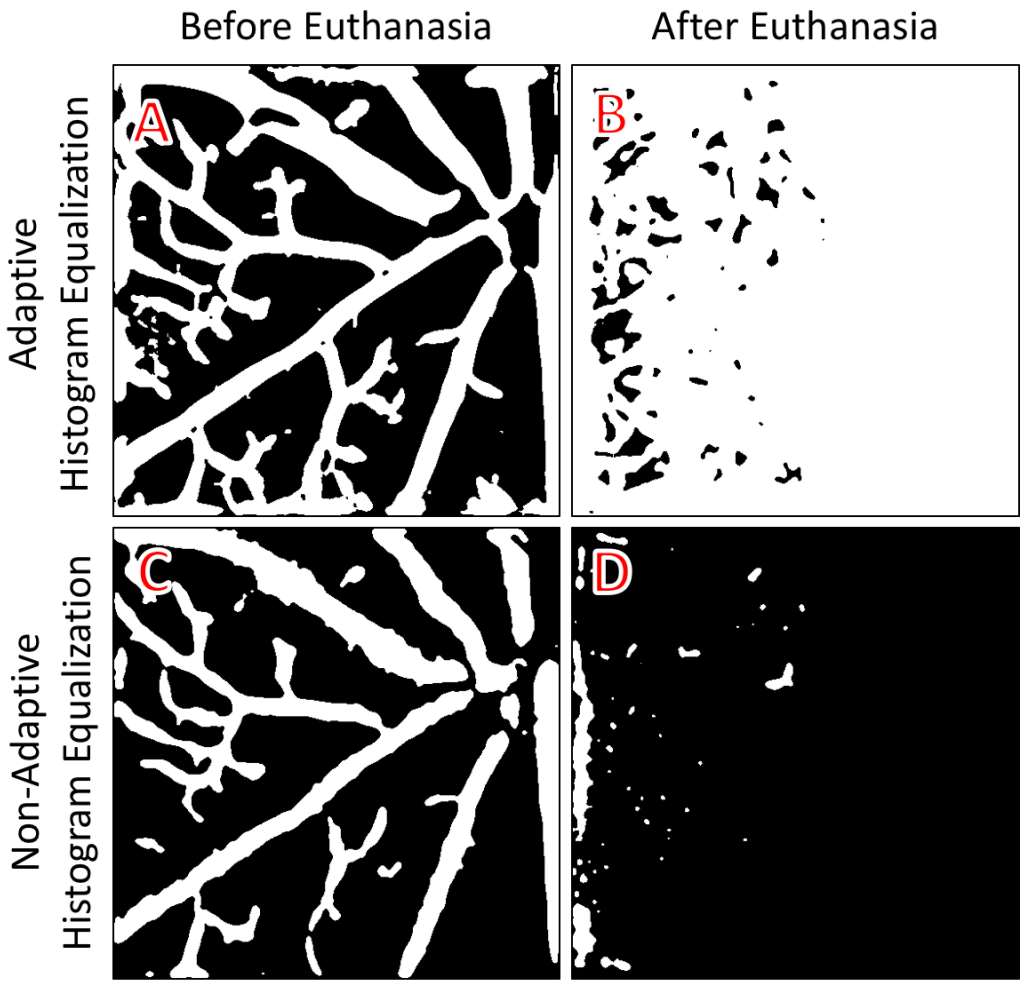

Figure 5.1: Adaptive histogram equalization is biased toward the presence of a signal, as illustrated by sub-image (B) where the noise floor is interpreted as the presence of vasculature. While the non-adaptive filter (C) does not detect every vessel that the adaptive approach detects (A), the non-adaptive approach more accurately depicts blood flow at time points where there is no blood flow (D). The image shown is representative of all six experiments.

Volumetric blood flow was calculated after vessel binarization by calculating the percentage of white pixels in the layer. Regional volumetric blood flow by retinal region is then plotted versus time for each animal as a representation of animal death. At later time points, retinal layers became more difficult to discern; thus, volumetric blood flow analysis was only performed in the superficial plexus (RNFL). It was expected that once the isoflurane overdose is initiated, volumetric blood flow will decrease to zero or the noise floor.

Total Retinal Thickness

The thickness of the retina is reported as the thickness [um] from the internal limiting membrane (ILM) to the top of the retinal pigment epithelium (RPE). Changes in thickness can be informative of the morphological status of the retina. For example, will the retina swell or thin as the mouse dies? It is expected that the retina will become edematous as the mouse dies, and retinal edema will be detectable by SAR-OCT.

Reflectance Index

As discussed in chapter one, reflectance index has been demonstrated as an early indicator for Glaucoma.[29], [30] Here, reflectance index is defined as the ratio of mean intensity in the RNFL to the mean intensity of the RPE, for each pixel in the x and y directions.

$$Reflectance\ Index\ (x,y) = \frac{\left[\sum_{z=T_{RNFL}(x,y)}^{B_{RNFL}(x,y)} I_{RNFL}(x,y,z)\right]/[H_{RNFL}(x,y)]}{\left[\sum_{z=T_{RPE}(x,y)}^{B_{RPE}(x,y)} I_{RPE}(x,y,z)\right]/[H_{RPE}(x,y)]}, \qquad (5.1)$$

where I is the intensity of a given voxel, T is the z-location of the top boundary of the given layer at a given Cartesian location, B is the z-location of the bottom boundary of the given

layer at a given Cartesian location, and *H* is the total thickness of the given layer at a given Cartesian location.

Scattering Angle Detection

To detect changes in scattering angle, the distribution of L/H_2 ratios is traced over time using the methods described in chapter 3, namely fitting the L/H_2 distributions to a Burr Type XII distribution and plotting the *c* parameter over time. Probability density functions are also reported for L/H_2 for three groups of retinal layers: (1) RNFL + GCL + IPL, (2) INL + OPL + ONL, and (3) RPE + choriocapillaris (CC). These three groups of retinal layers have distinct L/H_2 distributions as reported in chapter 5 and may be treated similarly for improved Burr distribution fitting.

RESULTS

Results for each mouse, for every feature, are visualized in Figures 5.2-5.10 and described in the text following each figure.

Volumetric Blood Flow

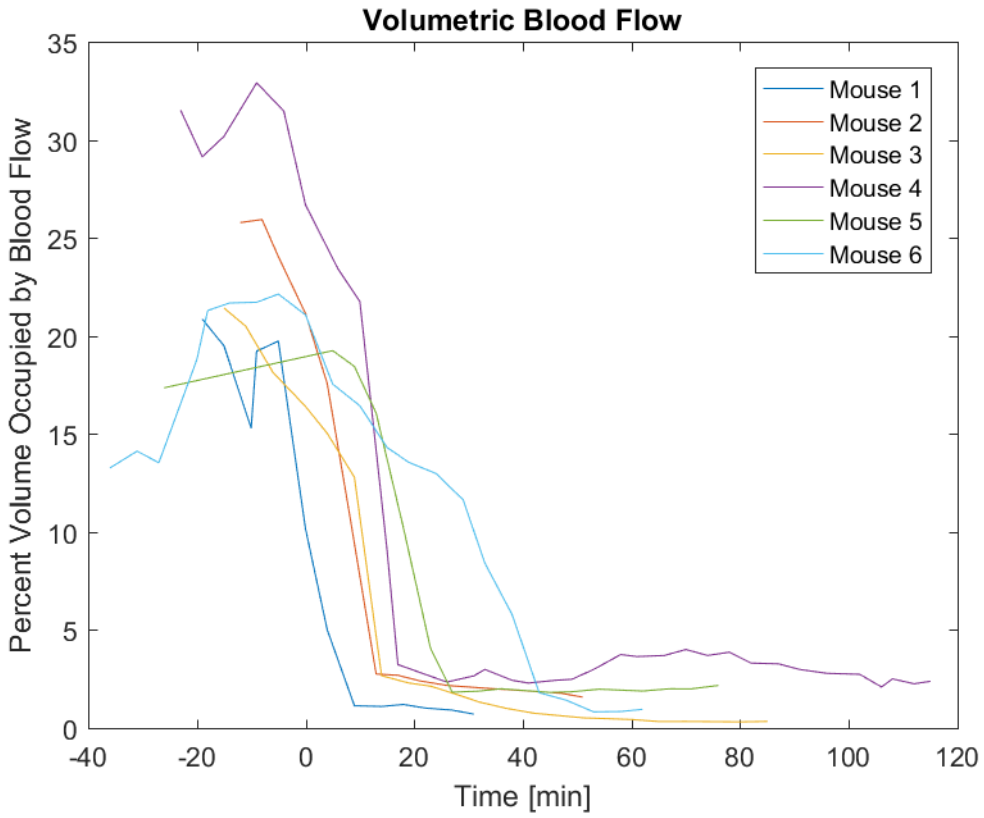

Figure 5.2: Volumetric blood flow for each euthanized mouse is plotted versus time, where t=0 minutes is the time at which isoflurane overdose was initiated. On average, the volumetric blood flow began at 21.7% (±6.385) and ended at 1.4% (±0.824)—the noise floor. The average time to no blood flow (noise floor) from the time of isoflurane overdose was 20.5 minutes (±12.582).

Volumetric blood flow analysis for the superficial plexus revealed a decrease in blood flow starting at the time isoflurane overdose was initiated (t = 0 minutes). On average, the volumetric blood flow began at 21.7% (±6.385) and ended at 1.4% (±0.824)—the noise floor. Variation in the percent volume occupied by blood flow varied from 13% to 32% in the superficial plexus; this value was highly dependent on the region of interest tracked during the euthanasia experiment. For some mice, the ROI was centered on the optic nerve head. This ROI maximized blood flow density in the image as the concentration

of vasculature increases at the optic nerve head. For other mice, the ROI had the optic nerve head in the corner of the image, such that the concentration of vasculature was lower. The mean time to blood flow cessation was 20.5 minutes (±12.582).

Total Retinal Thickness

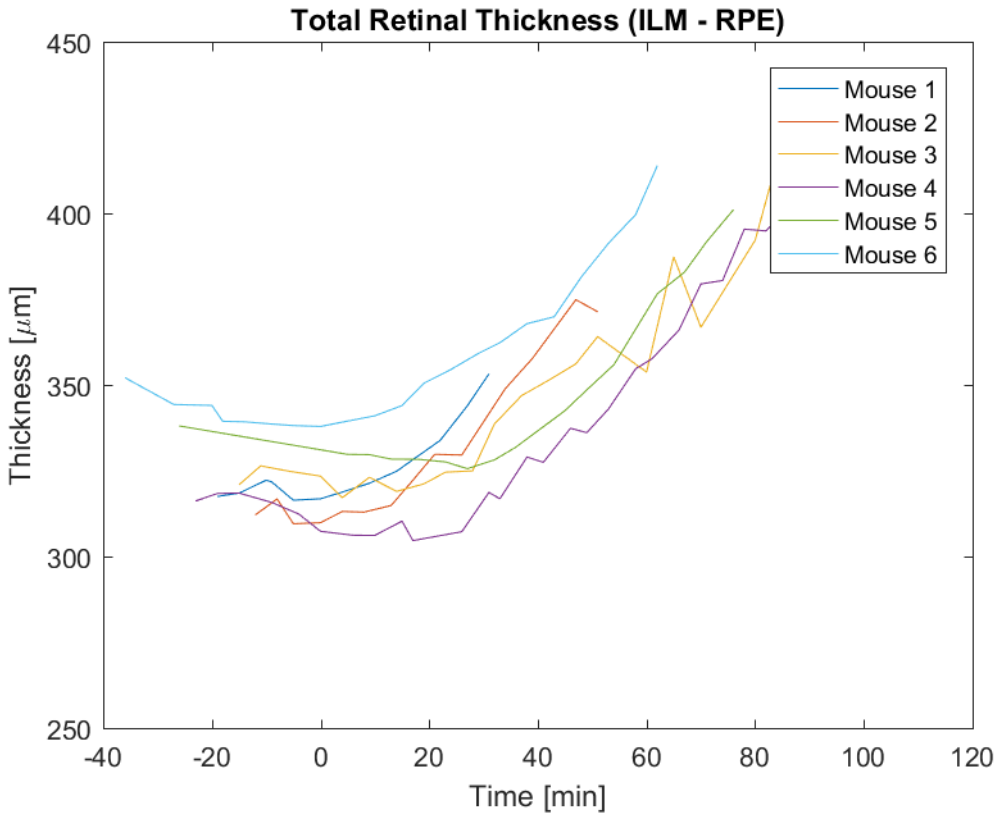

Figure 5.3: Total retinal thickness (ILM – RPE) increased through each euthanasia experiment from an average of 326.1 μm (±15.59), at a rate of 1.122 μm/min (±0.11) after initiating isoflurane overdose up to at least 90 minutes.

Total retinal thickness (ILM – superficial boundary of the RPE) for each mouse before euthanasia began was an average of 326.1 μm (±15.59). For each mouse, the total retinal thickness began to increase before blood flow ceased, and the retinal thickness increased approximately monotonically for as long as the retina was reliably observable

(before corneal clouding obscured the image). The average rate of thickness increase was 1.122 μm/min (±0.11).

Reflectance Index

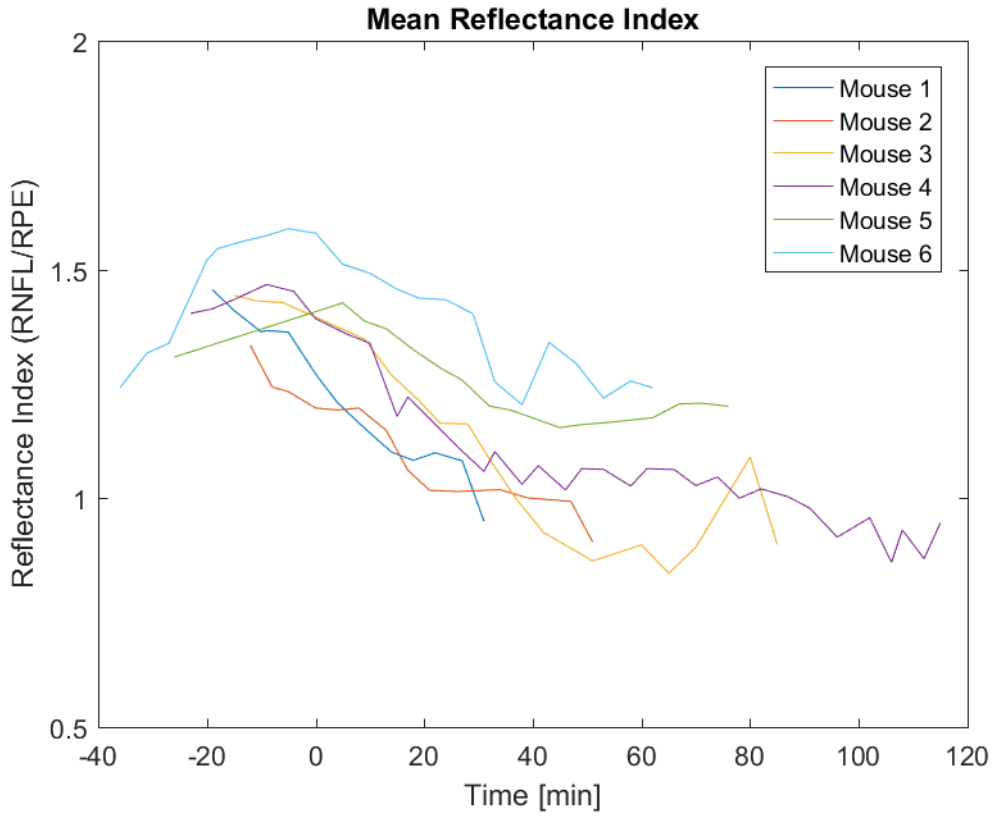

Figure 5.4: The mean reflectance index decreased after isoflurane overdose was initiated for each mouse. This decrease began before blood flow had ceased. In the case of mouse 6, the reflectance increases up to around isoflurane overdose initiation. The average decrease in the reflectance index occurred at a rate of -0.0056 [1/min] (±0.0026).

The reflectance index (RNFL/RPE) decreased for every mouse. The average value of the reflectance index at t=0 minutes was 1.3775 (±0.13), and the average rate of decrease for reflectance index was -0.0056 [1/min] (±0.0026). The changes in reflectance index were

not isolated to a single region of the retina, but instead occurred across each azimuthal region.

Scattering Angle Detection

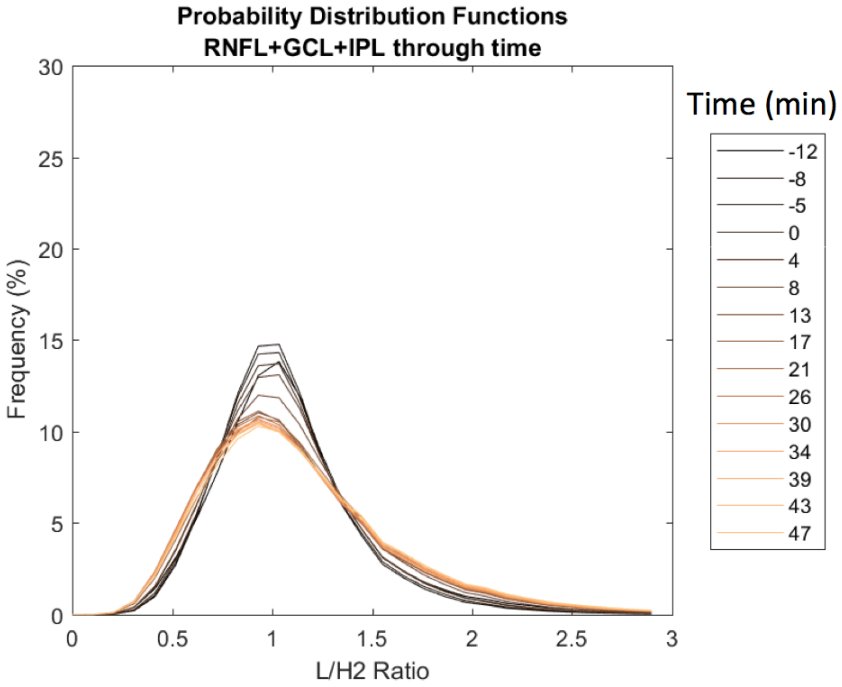

Figure 5.5: The probability distribution function of L/H_2 in the RNFL+GCL+IPL layer grouping for mouse 2 broadens through the euthanasia experiment.

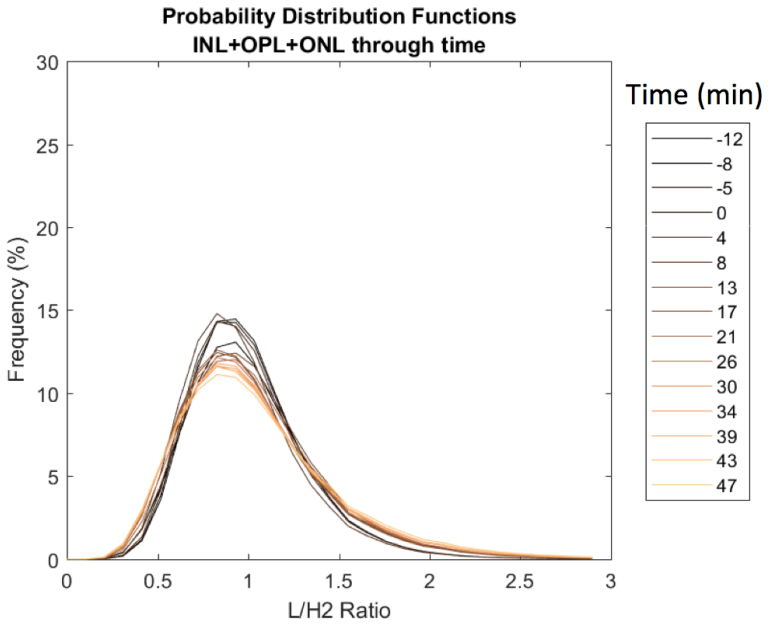

Figure 5.6: The probability distribution function of L/H_2 in the INL+OPL+ONL layer grouping for mouse 2 broadens through the euthanasia experiment.

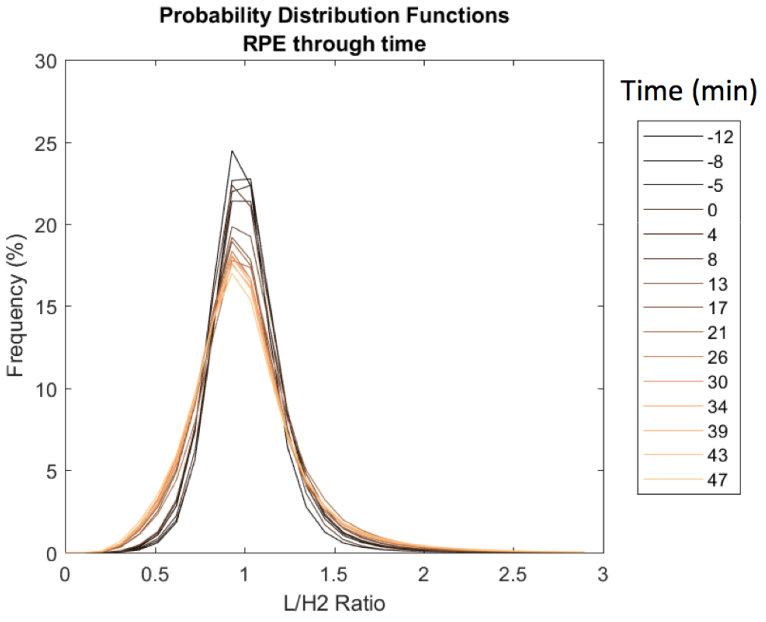

Figure 5.7: The probability distribution function of L/H_2 in the RPE for mouse 2 broadens through the euthanasia experiment.

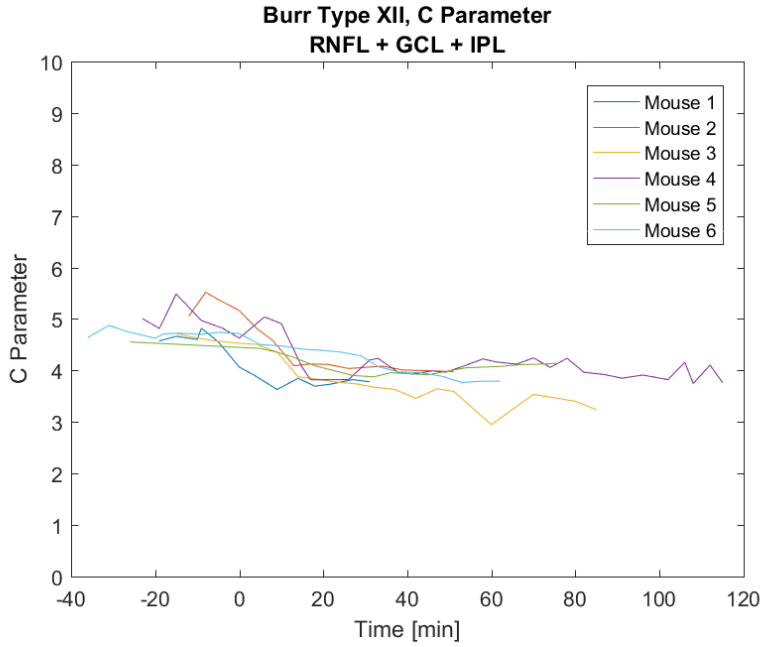

Figure 5.8: The C parameter of the Burr Type XII distribution fit to the RNFL + GCL + IPL layer grouping decreases for each mouse.

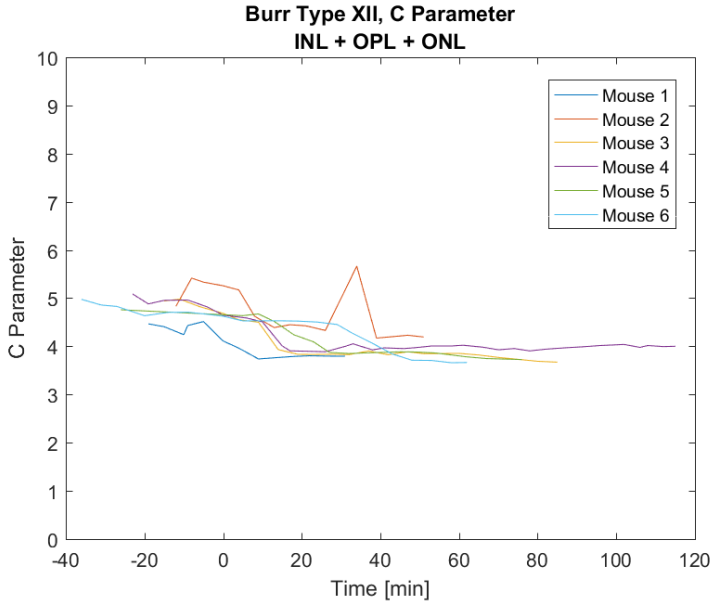

Figure 5.9: The C parameter of the Burr Type XII distribution fit to the INL + OPL + ONL layer grouping decreases for each mouse.

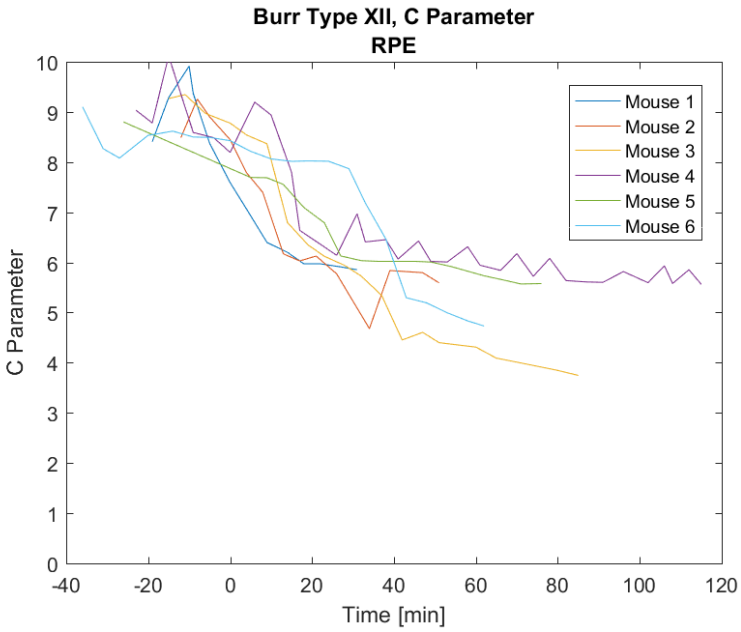

Figure 5.10: The C parameter of the Burr Type XII distribution fit to the RPE decreases for each mouse.

For each grouping of layers (RNFL+GCL+IPL, INL+OPL+OPL, RPE), and for each mouse, the distribution of L/H_2 values grew wider. Representative L/H_2 distributions (mouse 6) for each layer grouping are shown in Figures 5.5-5.7. As described in chapter 5, these changes are best captured numerically by fitting the Burr Type XII distribution and reporting the C parameter (see Figure 5.8-5.10), which is associated roughly with the variance of the distribution. Before initiating euthanasia, the average value for the C parameter was 4.80 (±0.21) for the superficial layers, 4.84 (±0.22) for the intermediate layers, and 8.85 (±0.35) for the RPE. At the point where blood flow had ceased for each mouse, the mean value for the C parameter was 3.88 (±0.15) for the superficial layers, 3.95 (±0.23) for the intermediate layers, and 5.24 (±0.53) for the RPE. The C parameter decreased in every mouse by an average (standard deviation) of 0.91 (±0.18) for the

superficial layers, 0.90 (±0.28) for the intermediate layers, and 2.61 (±0.62) for the RPE. These values are tabulated in Tables 5.1-5.3.

As was the case for the healthy murine retinas in Chapter 5, alpha and K parameters for the Burr Type XII distribution were not different across layers or time.

	RNFL + GCL + IPL		
	Before Euthanasia	After Blood Flow Ceases	Change
Mouse 1	4.58	3.63	-0.95
Mouse 2	5.05	4.09	-0.96
Mouse 3	4.72	3.88	-0.84
Mouse 4	5.01	3.82	-1.19
Mouse 5	4.55	3.90	-0.65
Mouse 6	4.87	3.96	-0.91
Mean	**4.80**	**3.88**	**-0.91**
St. Dev	***0.21***	***0.15***	***0.18***

Table 5.1: The average change in the C parameter for the superficial layers was -0.91. A paired t-test indicated a difference between before and after states ($p<0.0001$).

	INL + OPL + ONL		
	Before Euthanasia	After Blood Flow Ceases	Change
Mouse 1	4.47	3.74	-0.73
Mouse 2	4.83	4.39	-0.44
Mouse 3	4.94	3.93	-1.01
Mouse 4	5.09	3.91	-1.18
Mouse 5	4.76	3.87	-0.89
Mouse 6	4.98	3.84	-1.13
Mean	**4.84**	**3.95**	**-0.90**
St. Dev	***0.22***	***0.23***	***0.28***

Table 5.2: The average change in the C parameter for the superficial layers was -0.90. A paired t-test indicated a difference between before and after states ($p=0.0005$)

	RPE		
	Before Euthanasia	After Blood Flow Ceases	Change
Mouse 1	8.41	6.40	-2.01
Mouse 2	8.49	6.17	-2.32
Mouse 3	9.27	6.80	-2.47
Mouse 4	9.04	6.64	-2.40
Mouse 5	8.80	6.13	-2.67
Mouse 6	9.10	5.30	-3.80
Mean	**8.85**	**6.24**	**-2.61**
St. Dev	***0.35***	***0.53***	***0.62***

Table 5.3: The average change in the C parameter for the superficial layers was -2.61. A paired t-test indicated a difference between before and after states (p=0.0002).

DISCUSSION

A decrease in volumetric blood flow was expected as the mouse died, but the meaning of this analysis is a bit more complicated. CDV detects movement in the OCT image as it compares voxels through time to magnify high-variance features. That is, voxels with any movement will appear whiter in the angiography image. As the heart ceases to beat for each mouse, blood in the vessels does not disappear; instead, it ceases to have as much directed flow. The angiography method employed with OCT is sensitive to Brownian motion in fluids as well, which indicates that the average time to zeros for volumetric blood flow could actually be reporting the average time to blood coagulation, which would persist beyond the directed flow from the mouse's heartbeat. It is also possible that there may be some directed blood flow after the heartbeat is undetectable.

The finding of decreases in reflectance index seen in these mice as they are deprived of oxygen is an important one. A decrease in reflectance index could happen in at least two ways: a decrease in the RNFL reflectivity, or an increase in the RPE reflectivity. In fact, both of these changes are occurring for each mouse in the experiment: decreases in RNFL

reflectivity (Figure 5.11) and increases in RPE reflectivity (Figure 5.12). "Reflectivity" is the intensity of a particular layer in the OCT image (amplitude of the FFT of the detected fringe signal); these variations in intensity could be due to fluctuations in the absorption properties or the scattering properties of retina.

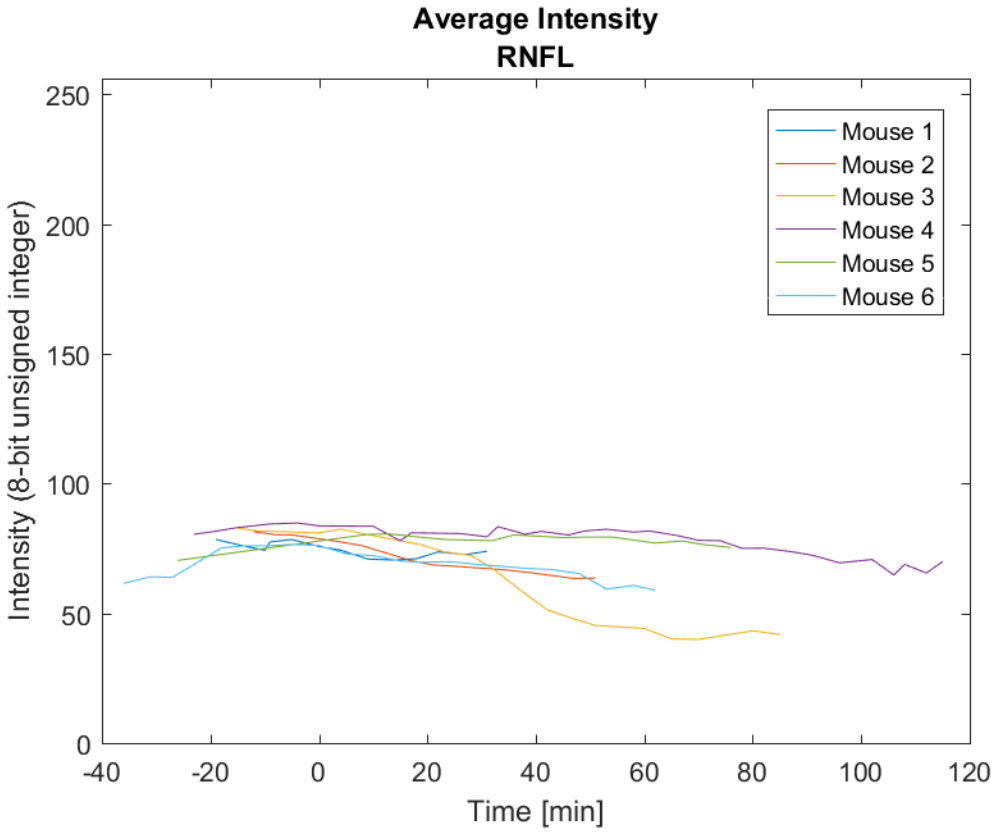

Figure 5.11: The slight decrease in RNFL intensity contributes to the decrease of the reflectance index.

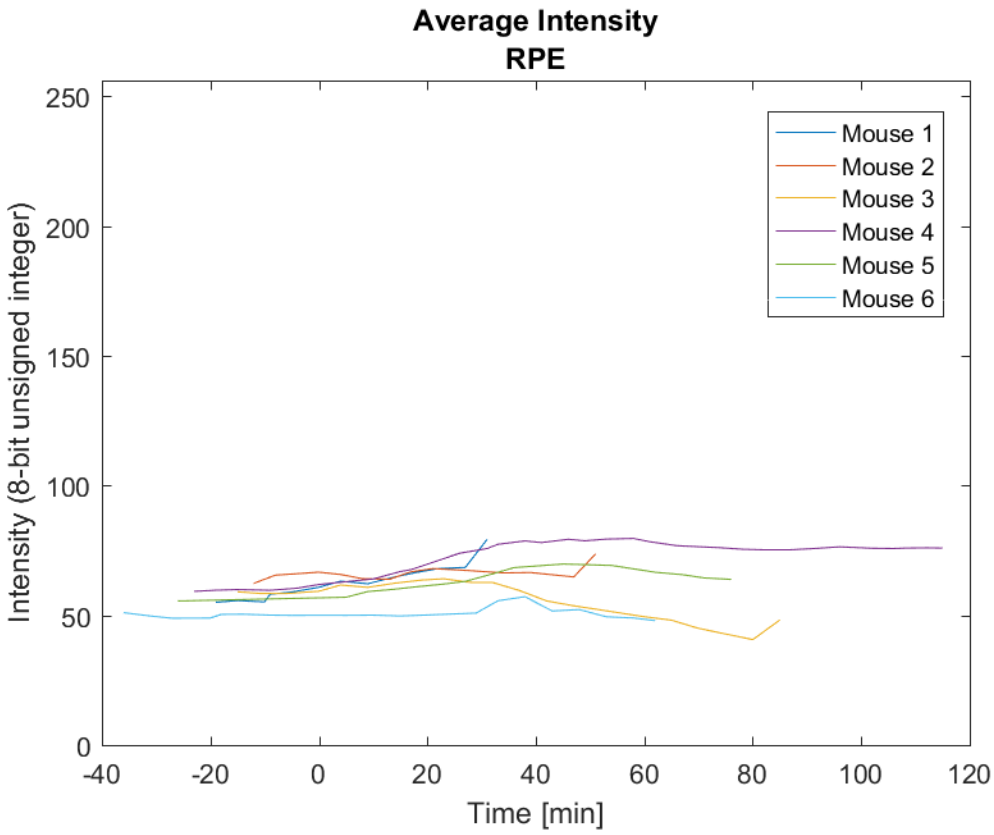

Figure 5.12: The slight increase in RPE intensity contributes to the decrease of the reflectance index.

Increases or decreases in reflectivity are difficult to isolate to either fluctuations in retinal absorption properties or retinal scattering properties, but SAR-OCT opens a door for further analysis in this regard because the PME offers angular discrimination. With SAR-OCT, the decrease in reflectance index are shown to be, at least in part, due to scattering angle changes. Thus, the most interesting result in this study is the combination of reflectance index increases and shifts in the L/H_2 distributions. Instead of simply reporting that the reflectivity index of the mouse retina decreases as the animal dies, this study indicates that there is indeed a shift in the behavior of light scattering in the oxygen-deprived retina giving rise to that change.

For every layer, including both the RNFL and the RPE, changes in the L/H_2 distributions reveal relative increases in both low-angle and high-angle scattering. That is, the probability of low-angle light scattering increases as the mouse dies ($L/H_2 > 1$ increases), and the probability of high-angle light scattering also increases ($L/H_2 < 1$ increases). The C parameter of the burr Type XII distribution decreases for every layer.

This increase in scattering angle diversity can perhaps be explained by a relative increase in entropy in the retina. Specifically, as the mouse dies, the energy required to maintain retinal organization decreases and ultimately expires. With the decrease in available energy, the cells and cellular components in the retina move toward equilibrium positions. This provides a first-order explanation of the increase in retinal thickness as the retinal components move toward to less-dense state. Furthermore, as cellular components begin to diffuse, they become less organized (higher entropy).

As the retina tissue becomes more entropic and scattering patterns become more homogenous, more light is transported to the RPE. That is, there is a general decrease in the number of photons detected by the SAR-OCT system scattered from the RNFL (Figure 5.11). These photons could continue to travel deeper into the retina, which would mean more photons have the opportunity to be transported to the RPE. Indeed, a higher number of photons are reflected from the RPE as the mouse dies as observed in Figure 5.12. Because of the angular discrimination available via SAR-OCT imaging, it is simultaneously observed that the backscattering behaviors of both of these layers change in the same way, a broader distribution of angles.

To explain further, one can imagine the RNFL volume as containing 512 x 512 x 10 voxels, that is just over 2,500,000 voxels. Each of these voxels is assigned a L/H_2 value, usually between 0 and 3. For the healthy pre-euthanasia retina, the L/H_2 tends to be around 1. In particular, about 15% of the voxels have a L/H_2 value that is between 0.95 and 1.05

(Figure 5.13, t = -12 minutes). For the voxels with L/H_2 values around 1, the number of photons scattering at a low angle (pathlength 1) is about equal to the number of photons scattering at a high angle (pathlength 2). That is, if *x* photons are detected in pathlengths 1 and 2 (discounting pathlength 3) as having scattered from a voxel in the RNFL where $L/H_2 = 1$, then we can say that *x/2* are scattered at low angles, and *x/2* are scattered at high angles. For voxels in the RNFL where L/H_2 values are about between 1.95 and 2.05 (about 2% of the voxels at t = -12 minutes, Figure 5.13), *2x/3* photons were scattered at low angle, and *x/3* photons were scattered at a high angle. The opposite is true for voxels in the RNFL where L/H_2 values are between 0.45 and 0.55: *x/3* photons were scattered at low angle, and *2x/3* photons were scattered at a high angle (about 3% of the voxels at t = -12 minutes, Figure 5.13).

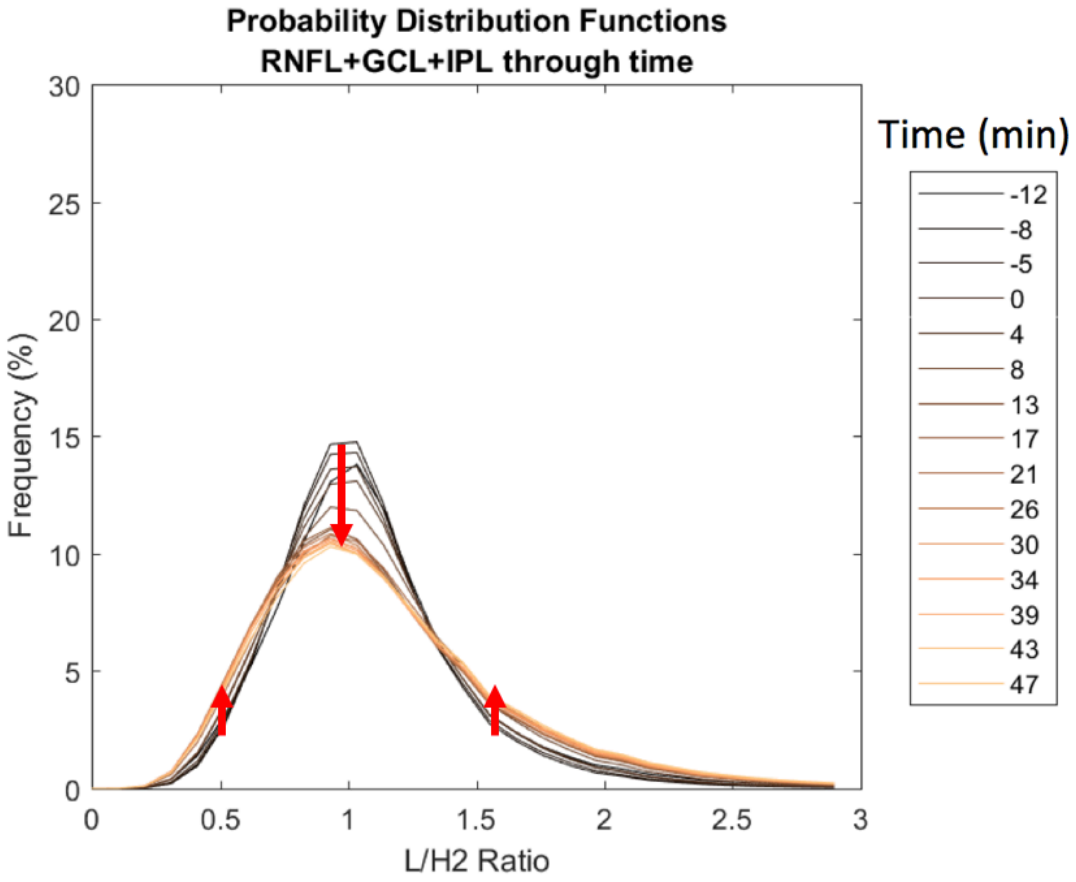

Figure 5.13: The probability distribution function of L/H_2 in the RNFL+GCL+IPL layer grouping for mouse 2 broadens through the euthanasia experiment. This is the same as Figure 5.5.

Now, as the mouse dies, the probability that any given voxel in the RNFL scatters such that *x/2* photons are scattered at low angles and *x/2* photons are scattered at high angles ($0.95 < L/H_2 < 1.05$) decreases from 15% to 10% at t = 47 minutes (Figure 5.13). At the same time, the probability that any given voxel in the RNFL scatters such that *2x/3* photons scatter at low angles and *x/3* photons scatter at high angles ($1.95 < L/H_2 < 2.05$) increases from 2% to 3%. Similarly, the probability that any given voxel in the RNFL scatters such that *x/3* photons scatter at low angles and *2x/3* photons scatter at high angles ($0.45 < L/H_2$

< 0.55) increases from around 3% to around 4%. The same pattern holds for voxels in the RPE.

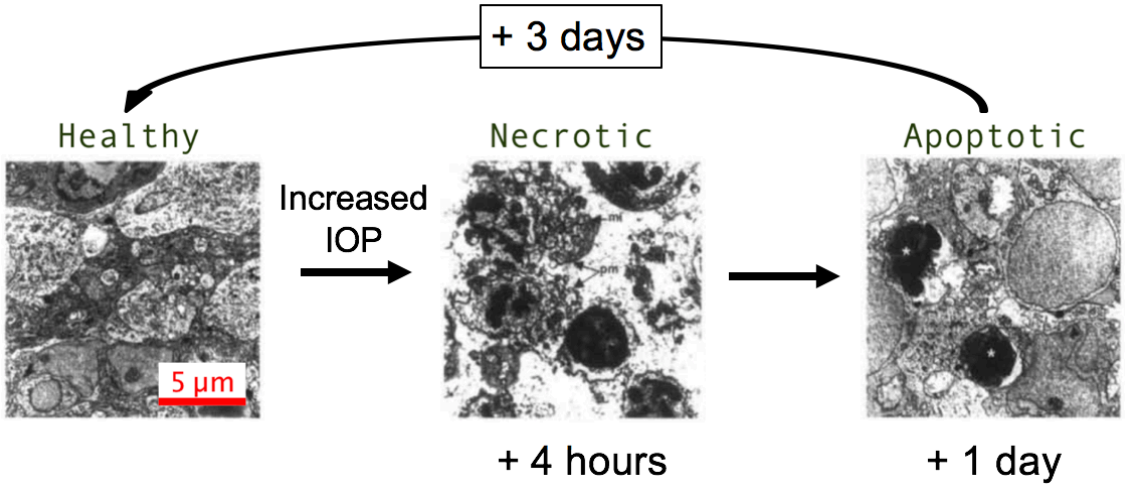

Figure 5.14: Images show electron photomicrographs of healthy, apoptotic, and necrotic retinal sections. For these images, apoptosis and necrosis were induced by retinal ischemia. Plasma membranes (pm) of necrotic cells have disintegrated, and the mitochondria (mi) are swollen and diffusing through the extracellular space. Images taken from Joo et al.[134]

Joo et al. conducted a study in which retinal ischemia was induced by artificially elevating ocular pressure for ninety minutes.[134] In this study, necrosis was noted in the earliest time points examined after the induced retinal ischemia—four hours after (Figure 5.14(C)). Apoptosis was noted in retinal sections one day after inducing ischemia (Figure 5.14(B)), and the retina returned to healthier levels of cellular function after three days (Figure 5.14(A)). Joo's study concluded that "ischemia produces the N-methyl-D-aspartate-mediated necrosis and slowly evolving apoptosis of neurons in the retina." Other in-vitro studies have demonstrated that necrosis occurs in neurons as early at 10-20 minutes after acute oxidative stress,[135] including swollen neurons[135] and fragmented mitochondria.[136] Cortical neurons exhibited apoptotic morphology around three hours after the ischemic insult.[135]

It is imaginable that a similar but different necrotic process is happening in this euthanasia study, as the mouse experienced systemic ischemia. As the retina dies, metabolic processes cease, membrane potentials vanish, and entropy increases, cells likely exhibit necrotic morphology; mitochondria swell, and the cells' plasma membranes disintegrate, spilling cellular components into the intracellular space (Figures 5.14, 5.15).

Healthy cells with components gathered inside plasma membranes might be thought to scatter light in patterns that are a superposition of each of the component's individual scattering profiles—a blurred scattering profile. In contrast, as cells undergo necrosis and spill their components into the intracellular space, light scatters in more distinct patterns. Now considering mitochondria, major scatterers of light in biological tissues: whereas before cellular necrosis, a mitochondria's Mie scattering profile is superposed with the scattering profile of the cell that contains it, a diffusing individual mitochondrion scatters light with a distinct Mie pattern, unaffected by the cellular components that once restrained or surrounded it. Indeed, it has been shown that shifts in optical scattering properties during cell death are due largely to changes in mitochondria.[131]

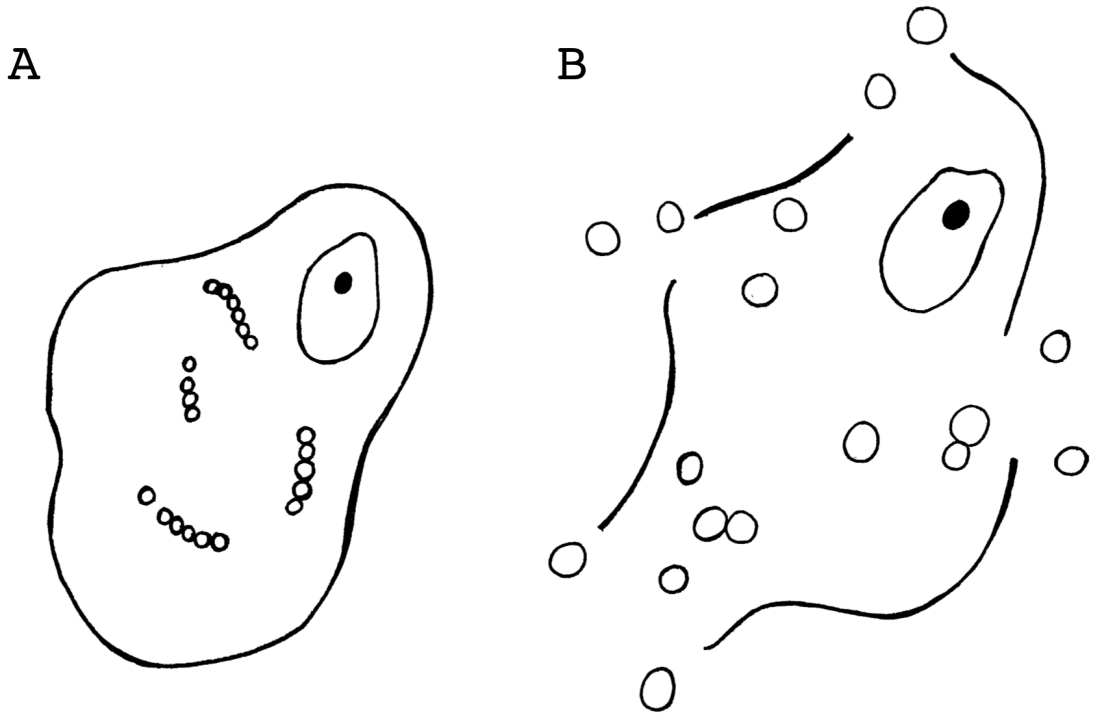

Figure 5.15: These cell diagrams illustrate necrotic changes to major scattering components in the cell: cell membrane, mitochondria, nucleus. Cell membranes break apart; mitochondria enlarge and disperse; and the nucleus remains largely unchanged. (A) is a healthy cell; (B) is a necrotic cell.

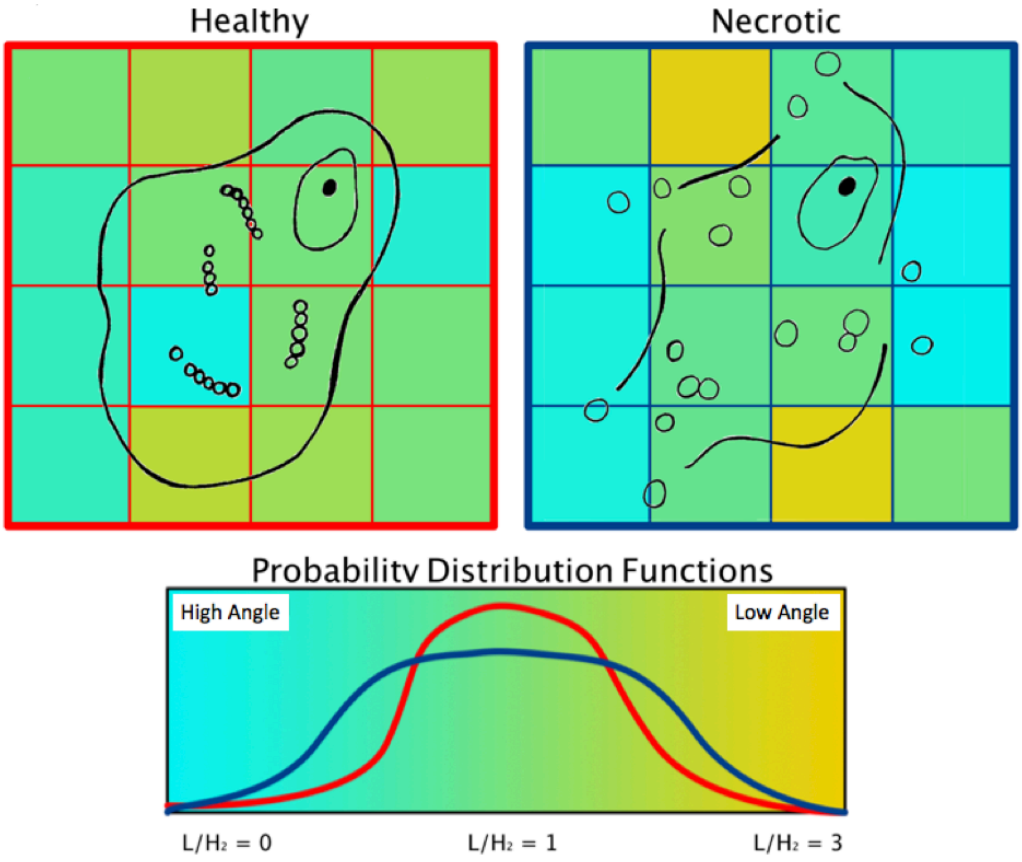

Figure 5.16: Healthy and necrotic tissues scatter with different L/H_2 distributions as has been demonstrated experimentally. This diagram proposes a model of light scattering for major scattering components of the cell: mitochondria, cell membranes, and the nucleus. Yellow indicates voxels that would are imagined to scatter more at low angles than at high angles. Blue voxels indicate areas where there is more high-angle scattering than low-angle scattering. Isolated mitochondria scatter at high-angles, the scattering profile less affected by a containing membrane or nearby cellular component. In contrast, cell membranes scatter at low angles, their scattering profiles less affected by diffused mitochondria. Voxels still containing a mix of cellular components maintain their blurred scattering profiles, a superposition of high-angle and low-angle scattering.

This study was limited in its aim, namely to confirm that longitudinal scattering angle changes may be detected using SAR-OCT. This is the first time that longitudinal

changes in light backscattering angles in the retina have been reported. However, this study alone does not necessarily implicate the utility of SAR-OCT for more subtle changes in the scattering properties of the retina. Changes in the scattering properties of the retina could be due to fast necrotic changes in the retina: mitochondrial fragmentation/swelling and cell membrane disintegration. More studies are needed to study what exactly is giving rise to the increase in both high and low-angle backscattering from the retina, but this study is promising as an imaging method for detection of neuropathies affecting the morphology of neurons in the retina.

CONCLUSIONS

Six mice were euthanized and their retinas monitored with SAR-OCT for approximately 1.5 hours during their deaths. Decreases in volumetric blood flow provided an indicator for tissue oxygenation during euthanasia. Total retinal thickness increased for each mouse, and the reflectance index decreased for each mouse. Most strikingly, the distribution of L/H_2 values showed a distinct broadening pattern, indicating an increase in both high and low-angle scattering when compared to the initial state of the mouse, pre-euthanasia. Altogether, SAR-OCT was demonstrated as being sensitive to profound longitudinal alterations in scattering properties of the murine retina.

Chapter 6: Retinal Changes in a Murine Model of Alzheimer's Disease Using SAR-OCT

This chapter is the goal and culmination of the dissertation. Here, I present the results of retinal imaging of mouse model for AD (3xTg-AD) using SAR-OCT. The data indicate that 3xTg-AD mice are distinguishable from control mice at early ages using SAR-OCT. Specifically, the fitted C parameter of L/H_2 distributions, the thickness of synaptic layers, and the reflectance index detect differences between disease and control groups at early stages of disease development. This study lays the groundwork for future clinical trials using SAR-OCT for early detection of AD.

Introduction

Chapter 1 lays a foundation for this chapter, describing how neurodegeneration, specifically AD affects the retina. In summary, changes observable with OCT—namely changes in light backscattering angle, vasculature, normalized reflectivity (reflectance index), and retinal layer thickness—carry potential as early indicators of AD.

Chapters 4 and 5 demonstrated the utility of SAR-OCT in quantifying the backscattering behavior of the retina. In the same chapters, features like reflectance index, retinal layer thickness, and volumetric blood flow were computed for additional data points and to corroborate changes in reflectivity. Those chapters lay the groundwork for a cross-sectional study of a murine model of AD.

Methods

Altogether, this cross-sectional study imaged the retinas of a murine model of AD and age-matched control mice at ages ranging from 10-48 weeks using SAR-OCT. Four imaging regimes were examined across this age range: (1) scattering angle, (2) vasculature, (3) normalized reflectivity, and (4) layer thicknesses. This section first describes the mouse

model, then outlines the experiment design, and finally describes the features examined for each SAR-OCT imaging regime.

Mouse Model

A triple-transgenic model for AD was used for this study, namely 3xTg-AD, which exhibits plaque and tangle pathology, as well as synaptic dysfunction.[137] The onset of Aβ and tau plaques for 3xTg-AD is similar to that of AD in human patients, both age- and region-dependent.[138], [139] For the 3xTg-AD murine model, Aβ immunoreactivity has been observed at 2 months in the hippocampus.[139] At four months, intraneuronal Aβ pathology is visible in the cortex and amygdala;[140] this correlates with observable cognitive deficits.[141] At month six, Aβ deposits are apparent in the frontal cortex,[140] when learning deficits, memory impediments, and neophobia appear.[142] At twelve months, Aβ is present in the hippocampus and other cortical regions,[142] and tau immunoreactivity becomes apparent in pyramidal neurons in the CA1 region.[140]

Many of the AD pathologies are present in the retina (an anterior extension of the central nervous system) at varying ages for the 3xTg-AD model. In one study, at eight and twelve months, the retinal thickness decreases significantly, but Aβ was not detected at four or eight months, though the tau levels were elevated.[143] In another study, it was observed that profound tau pathology in the visual system is present as early as three months in 3xTg-AD, prior to behavioral deficits and tau accumulation in the brain.[144] The tau build-up occurred mostly in the retinal ganglion cells' (RGCs) soma and dendrites. Another study examined the morphology of Muller cells and astrocytes in the 3xTg-AD retina and found that they undergo complex remodeling similar to astrocytes changes in the brain, though there is still some question as to the occurrence of these morphological changes in the human retina.[144] Regarding apoptosis and necrosis, Cordeiro et al showed

that fourteen-month-old 3xTg-AD mice showed significantly more RGCs in the early stages of apoptosis and fewer necrotic cells compared to age-matched controls.

In this study, Non-transgenic wild type C57BL/6J were used as controls. This is the background of the 3xTg-AD model.

Taken together it is a reasonable hypothesis that the 3xTg-AD mouse model will produce observable changes in the four SAR-OCT regimes.

Experiment Design

To assess the efficacy of SAR-OCT in detecting AD in 3xTg-AD mice compared to control mice, a cross-sectional study was designed in which 3xTg-AD mice and age-matched control mice were imaged (IACUC protocol #AUP-2015-00156). The distribution of age and sex is outlined in Table 6.1. In total, there were 32 mice: 20 3xTg-AD mice and 12 age-matched controls. The mice ranged in age from 10 weeks to 48 weeks.

	Control Mice (n=12)	3xTg-AD mice (n=20)
Group 1	**10 weeks old (3 males)**	10 weeks old (5 males)
Group 2	**19 weeks old (3 males)**	22 weeks old (2 males)
Group 3	**29 weeks old (3 males)**	30 weeks old (2 males, 2 females)
Group 4	**46 weeks old (3 males)**	45 weeks old (2 males, 2 females)
		48 weeks old (5 males)

Table 6.1: This study imaged a total of 20 3xTg-AD mice and 12 age-matched controls using SAR-OCT.

Each mouse was anesthetized first in an induction box (5% isoflurane), and then moved to the imaging platform where anesthesia continued via a custom nose cone (1.5-3% isoflurane). The left retina was imaged by the SAR-OCT system for about 15 minutes,

and then the mouse was allowed to recover. Overall, the imaging session lasted around 30 minutes per mouse.

Data Collected

Several SAR-OCT images were collected for each mouse retina with difference regions of interest, so as to obtain an expansive view of the retina. The number of images obtained for each mouse ranged from one to four, with almost no overlap. The optic nerve head (ONH) was used as a landmark. Under ideal imaging conditions, the ONH was placed once in each corner of the en-face view, so as to collect four volumes with different regions of the same retina. Occasionally, the experimental conditions limited the number of volume acquisitions.

Scattering

In the scattering regime, the L/H_2 ratio is utilized. Recall that the L/H_2 ratio is simply the ratio of intensities from pathlength 1 (L) and pathlength 2 (H_2). Each voxel in a defined region is treated as a sample of a Burr Type XII distribution, and the 3 parameters (α, C, and K) are chosen to minimize error. This process was described in fuller detail in Chapter 4.

After fitting L/H_2 voxel values of a given region and layer to the Burr distribution, one-way MANOVA is performed across time for the 3xTg-AD group. There are three canonical variables resulting for the three inputs (α, C, and K). The canonical variables are a multiplication of the mean-centered samples and an Eigen vector which was chosen to maximize the separation between age groups upon linear combination of these variables. The Eigen vector chosen for the 3xTg-AD group in the MANOVA process is then applied to the corresponding age-matched control group. Finally, the canonical variables of the

3xTg-AD mice and the control mice are compared at each time point using a t-test to indicate whether or not the samples were likely taken from the same distribution.

A second feature set in the scattering regime is to examine only the C parameter of the fitted Burr distribution. It was reported in an earlier chapter that the C parameter consistently contributes the most to the first canonical variable output by MANOVA. Examining the C parameter alone allow for a more intuitive understanding of the underlying scattering properties. Similar to the canonical variable analysis, the C parameters of the 3xTg-AD mice and the control mice are compared using a t-test at each time point.

Both the canonical variables and the C parameters are examined for various combinations of retinal layers and quadrants. Table 6.2 lists each feature examined in the scattering regime.

Feature(s)		
Dependent Variable(s)	**Retinal Layer**	**Retinal Region**
α, C, K	Superficial Layers	All Regions
α, C, K	Superficial Layers	Central
α, C, K	Superficial Layers	Peripheral
α, C, K	Superficial Layers	Nasal (Out-In)
α, C, K	Superficial Layers	Superior (Out-In)
α, C, K	Superficial Layers	Temporal (Out-In)
α, C, K	Superficial Layers	Inferior (Out-In)
α, C, K	Intermediate Layers	All Regions
α, C, K	Intermediate Layers	Central
α, C, K	Intermediate Layers	Peripheral
α, C, K	Intermediate Layers	Nasal (Out-In)
α, C, K	Intermediate Layers	Superior (Out-In)
α, C, K	Intermediate Layers	Temporal (Out-In)
α, C, K	Intermediate Layers	Inferior (Out-In)
α, C, K	RPE	All Regions
C Parameter	Superficial Layers	All Regions
C Parameter	Superficial Layers	Central
C Parameter	Superficial Layers	Peripheral
C Parameter	Superficial Layers	Nasal (Out-In)
C Parameter	Superficial Layers	Superior (Out-In)
C Parameter	Superficial Layers	Temporal (Out-In)
C Parameter	Superficial Layers	Inferior (Out-In)
C Parameter	Intermediate Layers	All Regions
C Parameter	Intermediate Layers	Central
C Parameter	Intermediate Layers	Peripheral
C Parameter	Intermediate Layers	Nasal (Out-In)
C Parameter	Intermediate Layers	Superior (Out-In)
C Parameter	Intermediate Layers	Temporal (Out-In)
C Parameter	Intermediate Layers	Inferior (Out-In)
C Parameter	RPE	All Regions

Table 6.2 In the scattering regime linear canonical variables (MANOVA) and the C parameter (Burr distribution) are examined for various combinations of layers and quadrants.

Angiography

In the angiography regime, two types of features are examined. The first is fasculature fractal dimension. For this feature, the dimension of the fractal is determined by the box-counting method[145] using binarized angiography images. There are three vascular plexuses—superficial, intermediate, and deep. An en-face binarized image is created using the methods described in chapter 3, and the box-counting method is applied to calculate the fractal dimension. The fractal dimension for 3xTg-AD mice is compared to control mice at each time point for various retinal layers and retinal quadrants/regions.

The second feature type is volumetric blood flow. This value is simply the percentage of space that is occupied by a blood vessel. Similarly to the fractal dimension analysis. Volumetric blood flow for 3xTg-AD mice is compared to control mice at each time point for various retinal layers and retinal quadrants/regions. Table 6.3 lists the angiographic features examined in this study.

Feature(s)		
Dependent Variable(s)	**Retinal Layer**	**Retinal Region**
Vasculature Fractal Dimension	Superficial Plexus	All Regions
Vasculature Fractal Dimension	Superficial Plexus	Central
Vasculature Fractal Dimension	Superficial Plexus	Peripheral
Vasculature Fractal Dimension	Intermediate Plexus	All Regions
Vasculature Fractal Dimension	Intermediate Plexus	Central
Vasculature Fractal Dimension	Intermediate Plexus	Peripheral
Vasculature Fractal Dimension	Deep Plexus	All Regions
Vasculature Fractal Dimension	Deep Plexus	Central
Vasculature Fractal Dimension	Deep Plexus	Peripheral
Volumetric Blood Flow	Superficial Plexus	All Regions
Volumetric Blood Flow	Intermediate Plexus	All Regions
Volumetric Blood Flow	Deep Plexus	All Regions

Table 6.3: The angiography regime examines two types of features (vasculature fractal dimension and volumetric blood flow) for various vascular plexuses and retinal regions.

Reflectance Index

Reflectance index is the ratio of intensities in the RNFL and the RPE. The RNFL and RPE representation used is the average of all three pathlengths. The reflectance index is compared to control mice at each time point for three retinal regions: (1) all regions, (2) central (in), and (3) peripheral (out) (Table 6.4).

Feature(s)		
Dependent Variable(s)	**Retinal Layer**	**Retinal Region**
Reflectance Index	RNFL	All Regions
Reflectance Index	RNFL	Central
Reflectance Index	RNFL	Peripheral

Table 6.4: SAR-OCT is used in the reflectance regime to examine differences amongst 3xTg-AD mice and controls across retinal regions and time.

Retinal Layer Thickness

In the thickness regime, SAR-OCT compares the thicknesses of various layers in different regions for the two groups at each time point. The thickness are obtained using the retinal segmentation algorithm outlined in chapter 3. Table 6.5 lists each feature in the thickness regime.

Feature(s)		
Dependent Variable(s)	**Retinal Layer**	**Retinal Region**
Layer Thickness	Superficial Layers	All Regions
Layer Thickness	Superficial Layers	Central
Layer Thickness	Superficial Layers	Peripheral
Layer Thickness	INL	All Regions
Layer Thickness	INL	Central
Layer Thickness	INL	Peripheral
Layer Thickness	OPL	All Regions
Layer Thickness	OPL	Central
Layer Thickness	OPL	Peripheral
Layer Thickness	ONL	All Regions
Layer Thickness	ONL	Central
Layer Thickness	ONL	Peripheral
Layer Thickness	All Layers	All Regions
Layer Thickness	All Layers	Central
Layer Thickness	All Layers	Peripheral

Table 6.5: The thicknesses of retinal layers are examined for superficial layers (ILM-IPL), the INL, the OPL, the ONL, and all layers combined, for central, peripheral, and combined regions.

RESULTS

The results of the t-tests comparing 3xTg-AD and control mice across time are tabularized in Tables 6.6-6.10.

Scattering

Considering the first canonical variable, differences between the 3xTg-AD mice and the control mice were most present at the 19-22 week range. The superficial layers (RNFL + GCL + IPL) tended to have the most distinguishing value—particularly the central regions around the optic nerve head. Specifically, the first canonical variable in the central superficial layers demonstrated an interesting trend. The values of the first canonical variable were significantly greater in the control mice for the 10-week-old group ($p=0.003$) and decreased out to week 45. The canonical variables for 3xTg-AD mice was less than the control at 10 weeks but greater than the control at 20 weeks. Figure 6.1 shows that the canonical variable persisted for 20 weeks and then decreased to be statistically similar to the values of the control mouse at week 45.

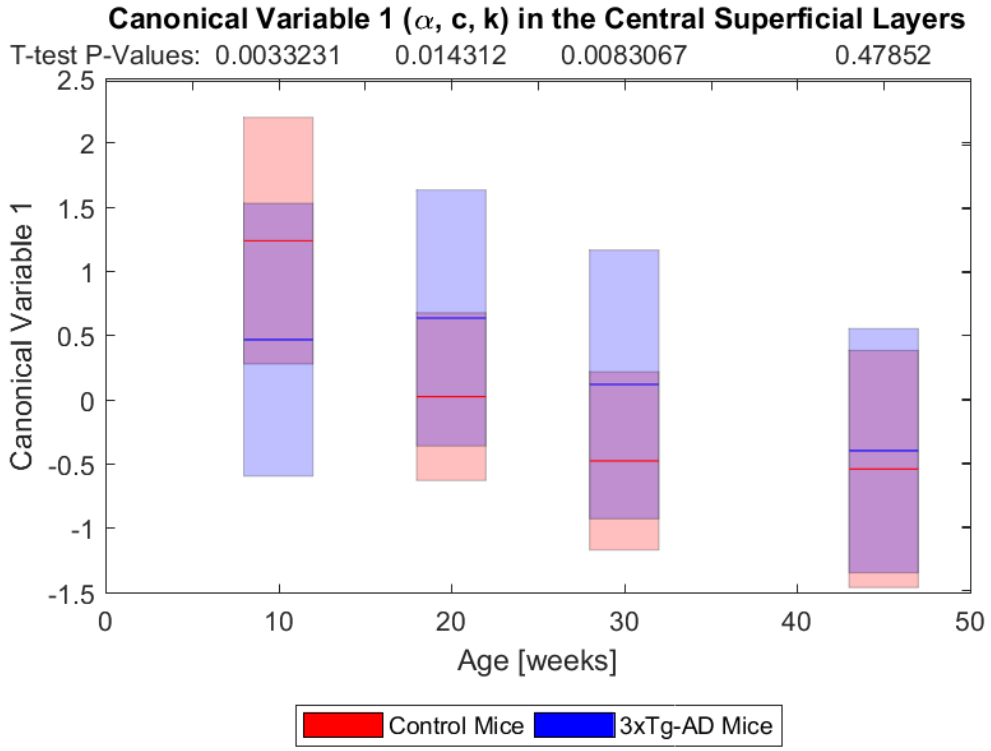

Figure 6.1: The first canonical variable (MANOVA) reveals early scattering differences between the 3xTg-AD mice and control mice. The mean value of the 3xTg-AD mouse persists through 20 weeks and then decreases out to 45 weeks. The mean value of the control mouse variable begins higher than the 3xTg-AD model, but decreases rapidly out to 45 weeks.

Considering the C parameter alone, statistical differences between the 3xTg-AD mice and the control mice were prominent in the 10 week range. Twelve of fifteen layer/region combinations revealed a higher C parameter in the control mouse at 10 weeks. For the peripheral regions of the superficial layer and nearly all regions of the intermediate layers, the C parameter value persisted through the disease. One notable exception to the statistical differences is in the 19-22 week range. At this time point, there were only three statistical differences (out of fifteen possible), and two of them reveal a higher value for

the 3xTg-AD mice. However, in the 19-22 week range, the mean of the C parameter for the control mice is greater than the 3xTg-AD mice in most cases, though not significantly different.

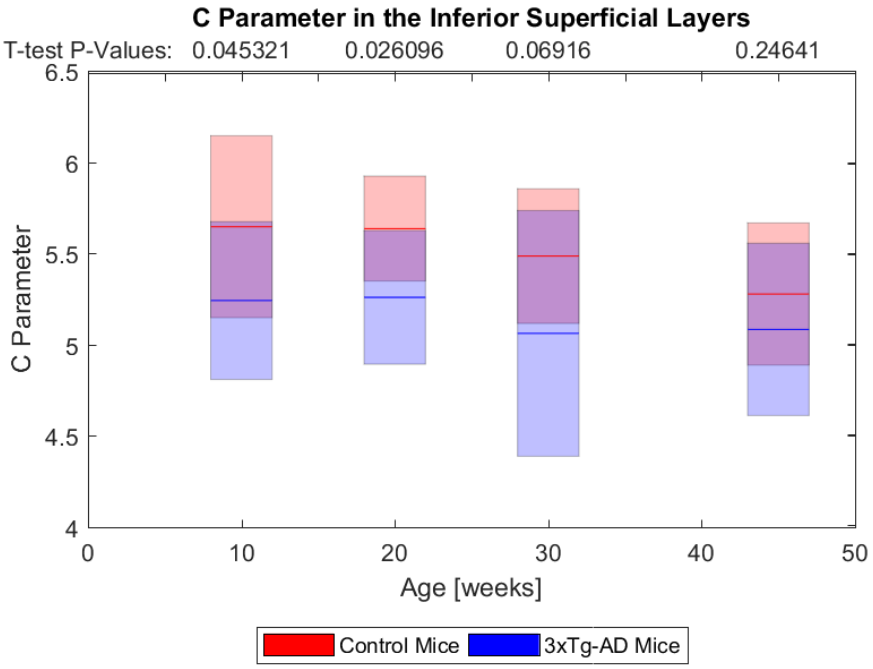

Figure 6.2: The C parameter in the inferior superficial layers is representative of other C parameter data. The C parameter for the control mice is generally greater in than that of the 3xTg-AD mice, particularly in in the earliest time point, 10 weeks.

Figure 6.2 shows the C parameter in the interior superficial layers, a representative image in that the mean C parameter of the control mice is on average greater than that of the 3xTg-AD mice.

Also of note is the general decrease of the C parameter with time. Even without the control mice, which are notoriously difficult to match to a disease model, the C parameters within the 3xTg-AD groups decrease with the ages of the group.

Figure 6.3 shows the C parameter in the deep layers (RPE). There are not statistical differences between the groups in this case, however, it should be noted that that mean

values of the C parameters are closer to 9 or 10—comparable to those of mice in other studies, reinforcing the repeatability of the C parameter across mice.

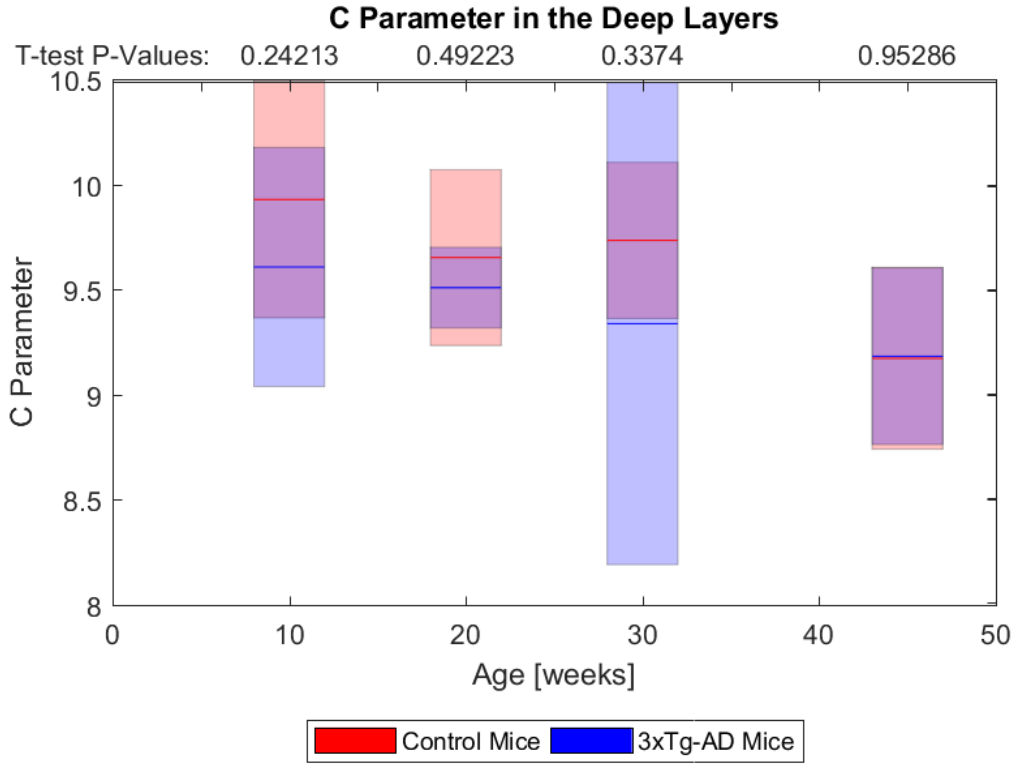

Figure 6.3: The C parameters in the deep layers (RPE) do not show any differences between the 3xTg-AD and control groups, but the values of the C parameter in the RPE are comparable to those of the RPE in other studies.

Scattering						
Feature(s)			P-value: Blue - AD>Control; Red - AD<Control			
Dependent Variable(s)	Retinal Layer	Retinal Region	10 Weeks	19-22 Weeks	29-30 Weeks	45-48 Weeks
1st Canonical Variable (α, C, K)	Super.	All	0.178	0.002	0.231	0.498
1st Canonical Variable (α, C, K)	Super.	In	0.003	0.014	0.008	0.479
1st Canonical Variable (α, C, K)	Super.	Out	0.789	<0.001	0.467	0.566
1st Canonical Variable (α, C, K)	Super.	N (Out-In)	0.106	0.05	0.785	0.345
1st Canonical Variable (α, C, K)	Super.	S (Out-In)	0.001	0.924	0.008	0.791
1st Canonical Variable (α, C, K)	Super.	T (Out-In)	0.261	0.003	0.06	0.042
1st Canonical Variable (α, C, K)	Super.	I (Out-In)	0.98	<0.001	0.086	0.345
1st Canonical Variable (α, C, K)	Int.	All	0.139	0.001	0.348	0.648
1st Canonical Variable (α, C, K)	Int.	In	0.649	<0.001	0.39	0.799
1st Canonical Variable (α, C, K)	Int.	Out	0.235	<0.001	0.095	0.576
1st Canonical Variable (α, C, K)	Int.	N (Out-In)	0.045	0.075	0.366	0.377
1st Canonical Variable (α, C, K)	Int.	S (Out-In)	0.003	<0.001	0.726	0.087
1st Canonical Variable (α, C, K)	Int.	T (Out-In)	0.221	0.001	0.54	0.964
1st Canonical Variable (α, C, K)	Int.	I (Out-In)	0.799	0.285	0.93	0.534
1st Canonical Variable (α, C, K)	RPE	All	0.306	0.003	0.475	0.095

Table 6.6: For the scattering regime, there were statistical differences between the 3xTg-AD and control mice for several of the image features, at various time-points. For the multivariate analysis that yielded canonical variables, the 3xTg-AD mice had generally higher values than the controls at early time points, but those differences faded at later time points.

Scattering						
Feature(s)			P-value: Blue - AD>Control; Red - AD<Control			
Dependent Variable(s)	Retinal Layer	Retinal Region	10 Weeks	19-22 Weeks	29-30 Weeks	45-48 Weeks
C Parameter	Super.	All	0.019	0.574	0.138	0.254
C Parameter	Super.	In	0.001	0.614	0.043	0.055
C Parameter	Super.	Out	<0.001	0.395	0.010	0.036
C Parameter	Super.	N (Out-In)	0.007	0.188	0.016	0.183
C Parameter	Super.	S (Out-In)	0.108	0.714	0.113	0.197
C Parameter	Super.	T (Out-In)	0.02	0.998	0.31	0.172
C Parameter	Super.	I (Out-In)	0.045	0.026	0.069	0.246
C Parameter	Int.	All	0.153	0.639	0.153	0.590
C Parameter	Int.	In	<0.001	0.049	0.002	0.001
C Parameter	Int.	Out	<0.001	0.270	0.003	0.001
C Parameter	Int.	N (Out-In)	<0.001	0.346	0.014	0.019
C Parameter	Int.	S (Out-In)	0.013	0.800	0.036	0.006
C Parameter	Int.	T (Out-In)	<0.001	0.009	0.106	0.007
C Parameter	Int.	I (Out-In)	0.010	0.581	0.006	0.352
C Parameter	RPE	All	0.242	0.492	0.337	0.953

Table 6.7: For the C parameter analysis in the scattering regime, the values for the control mice are generally greater than those of the 3xTg-AD mice. That difference persists in most cases through a majority of the time points.

Angiography

There were only two cases of statistically significant differences in the angiography regime, however these differences are not meaningful enough to draw any conclusions.

Angiography						
Feature(s)			P-value: Blue - AD>Control; Red - AD<Control			
Dependent Variable(s)	Retinal Layer	Retinal Region	10 Weeks	19-22 Weeks	29-30 Weeks	45-48 Weeks
Vasculature Fractal Dimension	Sup. Plexus	All	0.589	0.336	0.339	0.764
Vasculature Fractal Dimension	Sup. Plexus	In	0.123	0.535	0.235	0.923
Vasculature Fractal Dimension	Sup. Plexus	Out	0.589	0.514	0.030	0.312
Vasculature Fractal Dimension	Int. Plexus	All	0.733	0.148	0.292	0.835
Vasculature Fractal Dimension	Int. Plexus	In	0.149	0.668	0.27	0.908
Vasculature Fractal Dimension	Int. Plexus	Out	0.841	0.887	0.17	0.147
Vasculature Fractal Dimension	Dp. Plexus	All	0.823	0.183	0.400	0.637
Vasculature Fractal Dimension	Dp. Plexus	In	0.123	0.466	0.331	0.843
Vasculature Fractal Dimension	Dp. Plexus	Out	0.563	0.632	0.357	0.298
Volumetric Blood Flow	Sup. Plexus	All	0.191	0.569	0.058	0.573
Volumetric Blood Flow	Int. Plexus	All	0.124	0.312	0.054	0.991
Volumetric Blood Flow	Dp. Plexus	All	0.109	0.39	0.011	0.512

Table 6.8: For the angiography regime, there were only two instances of statistical differences. These differences are not sufficient to make any claim on the utility of fractal dimensions or volumetric blood flow in this data set.

Retinal Layer Thickness

Differences in retinal layer thicknesses were largely isolated to the superficial layers (RNFL + GCL + IPL) and the ONL, with differences also appearing in total retinal thickness. There was also more differences between 3xTg-AD and control groups at the early time points compared to the later time points (6 control>AD at 10 weeks, 3 control>AD at 45 weeks).

The central (in) regions of the retina showed the most consistent differences. The central superficial layer was thicker in the control mice at every time point (Figure 6.4),

and the central ONL thickness was greater at every time point except the 45 weeks group (Figure 6.5). Additionally, the total retinal thickness in the central retinal zones was greater in the control group for every time point (Figure 6.6).

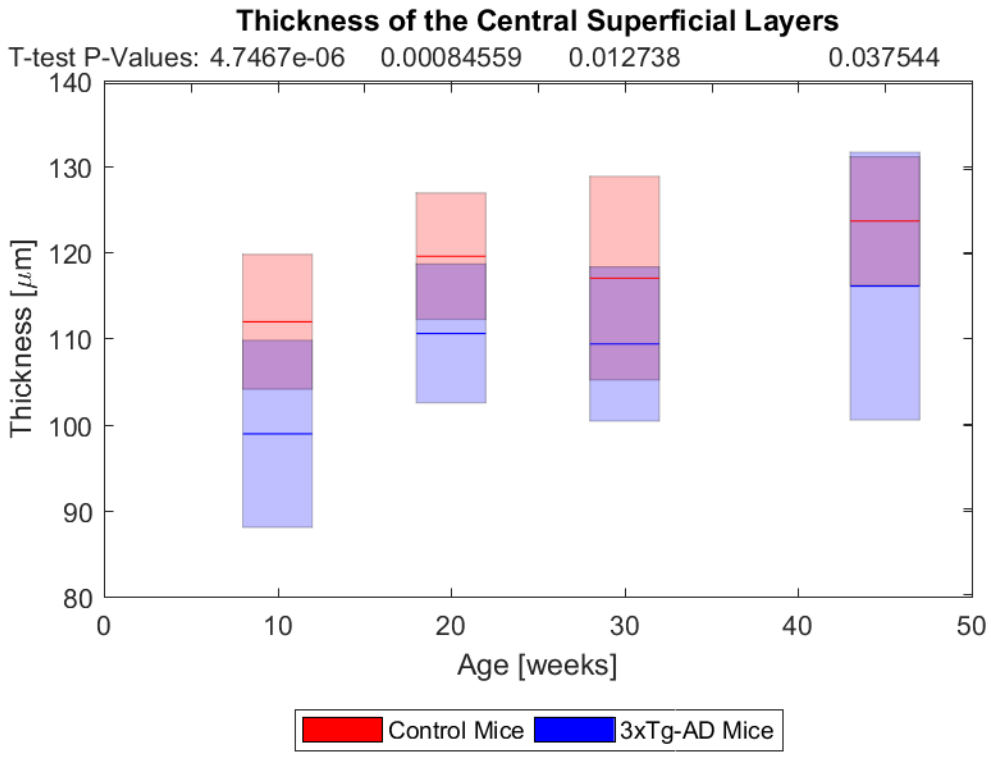

Figure 6.4: The thickness of the central superficial layers is significantly greater in the control mice at every time point.

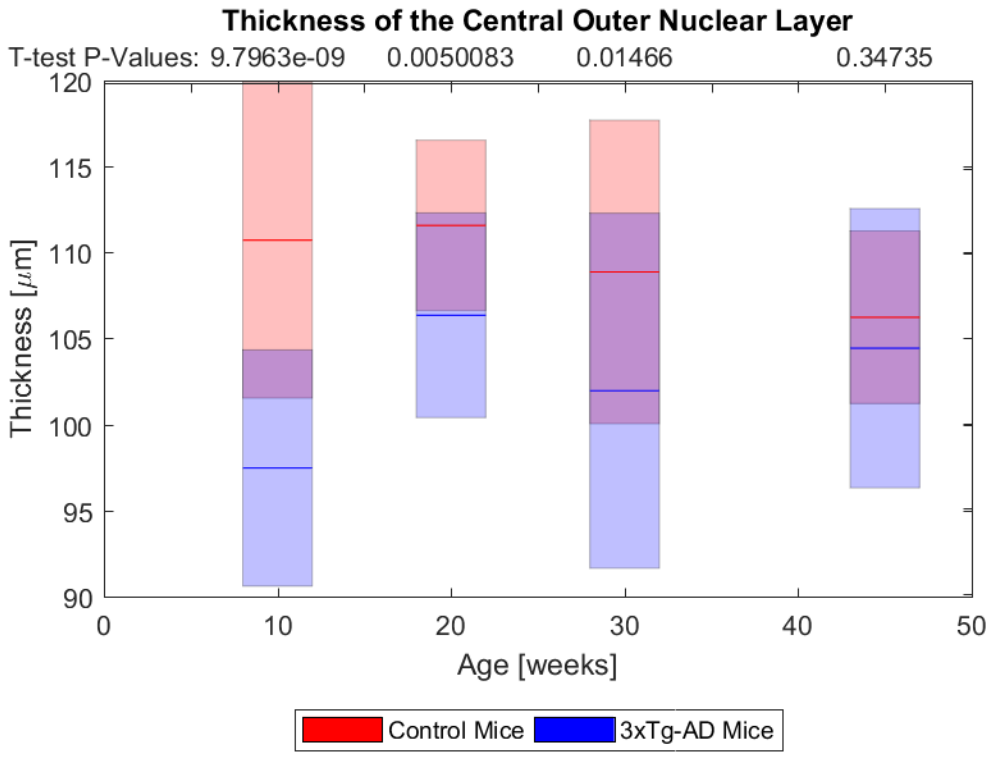

Figure 6.5: The thickness of the central ONL is significantly greater in the control mice at every time point, except the 45-week time point.

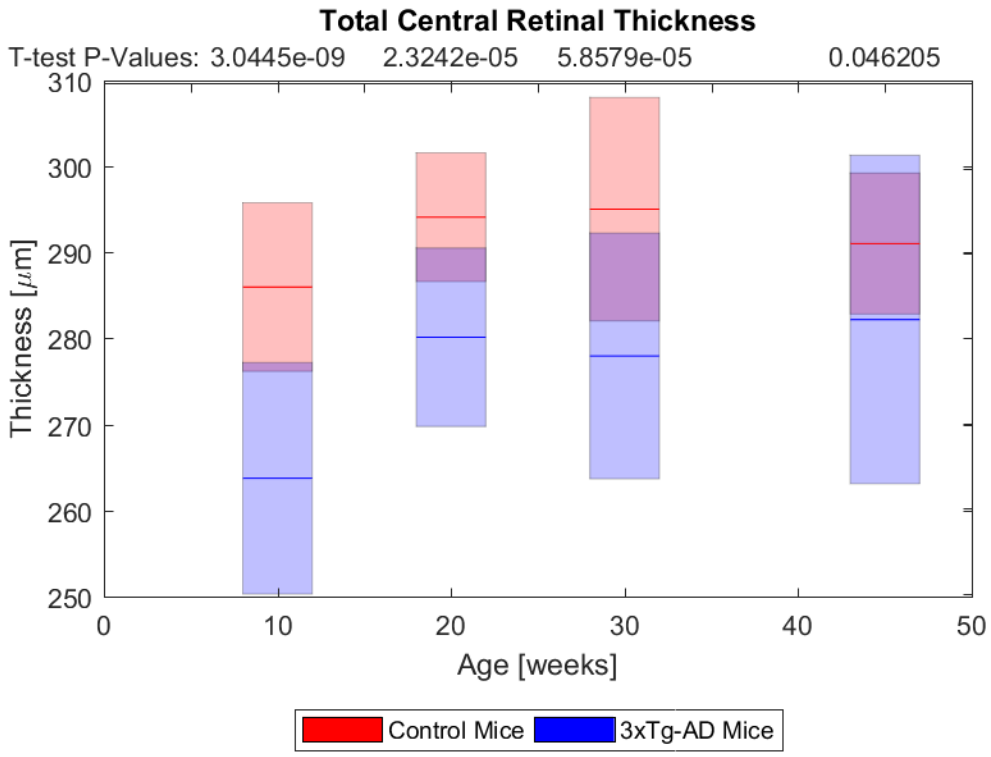

Figure 6.6: The thickness of the total retina in the central zones around the optic nerve head is significantly greater in the control mice at every time point.

Thickness						
Feature(s)			P-value: Blue - AD>Control; Red - AD<Control			
Dependent Variable(s)	Retinal Layer	Retinal Region	10 Weeks	19-22 Weeks	29-30 Weeks	45-48 Weeks
Layer Thickness	Super.	All	0.51	0.024	0.059	0.228
Layer Thickness	Super.	In	<0.001	0.001	0.013	0.038
Layer Thickness	Super.	Out	<0.001	0.094	0.002	0.002
Layer Thickness	INL	All	0.069	0.139	0.136	0.744
Layer Thickness	INL	In	0.001	0.884	0.308	0.602
Layer Thickness	INL	Out	0.159	0.285	0.773	0.235
Layer Thickness	OPL	All	0.044	0.13	0.155	0.584
Layer Thickness	OPL	In	0.002	0.679	0.721	0.792
Layer Thickness	OPL	Out	0.066	0.606	0.372	0.881
Layer Thickness	ONL	All	0.349	0.043	0.075	0.399
Layer Thickness	ONL	In	<0.001	0.005	0.015	0.347
Layer Thickness	ONL	Out	<0.001	0.192	0.102	0.447
Layer Thickness	All	All	0.791	0.038	0.04	0.331
Layer Thickness	All	In	<0.001	<0.001	<0.001	0.046
Layer Thickness	All Layers	Out	<0.001	0.171	<0.001	0.087

Table 6.9: For the thickness regime, the superficial layers, the ONL, and the entire retinal thickness showed differences between the 3xTg-AD and control groups, particularly in the central (In) quadrants.

Reflectance Index

Early differences in the reflectance index were seen when comparing the 3xTg-AD mice to the controls. Namely, in the central region around the optic nerve head, the reflectance index of the control mice was significantly greater than that of the 3xTg-AD mice at 10 weeks. In fact, the mean value of the reflectance index of the control group was greater at every time point, though not significantly so (Figure 6.7).

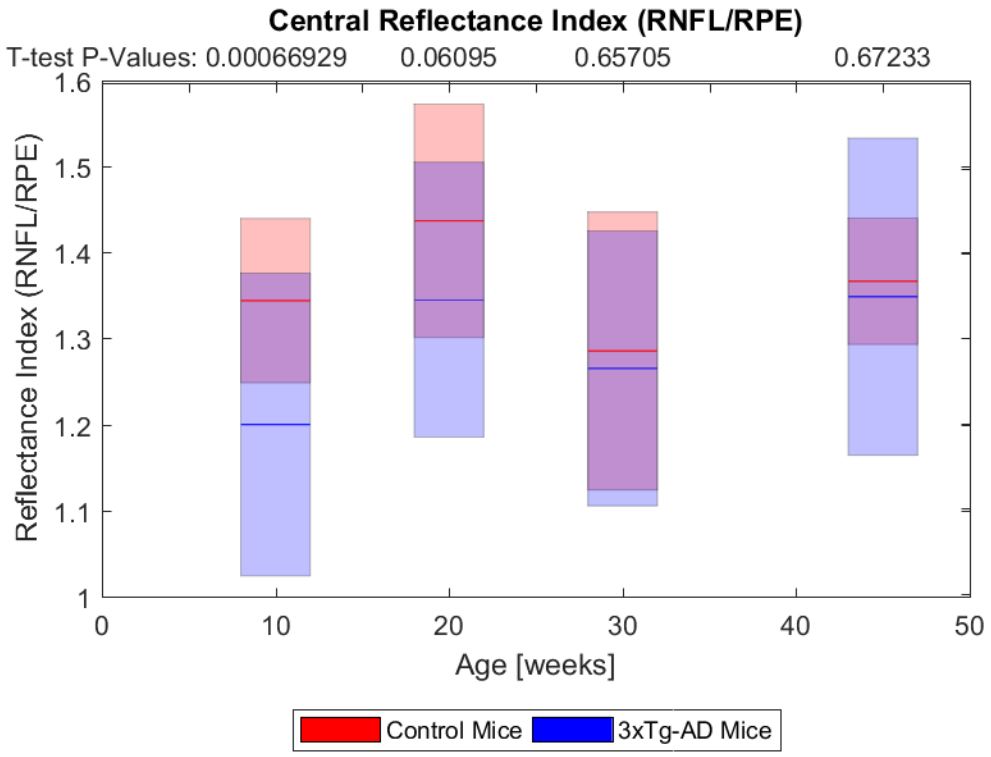

Figure 6.7: The reflectance indices of the central regions of the retina were significantly greater for control mice at 10 weeks. The mean reflectance value was greater at every time point after that also, though not significantly so.

Reflectance Index						
Feature(s)			P-value: Blue - AD>Control; Red - AD<Control			
Dependent Variable(s)	Retinal Layer	Retinal Region	10 Weeks	19-22 Weeks	29-30 Weeks	45-48 Weeks
Reflectance Index	RNFL	All	0.528	0.027	0.105	0.592
Reflectance Index	RNFL	In	0.001	0.061	0.657	0.672
Reflectance Index	RNFL	Out	0.065	0.24	0.307	0.679

Table 6.10: For the reflectance regime, there were no strong patterns to distinguish between the groups.

The complete set of output plots is included in Appendix C.

DISCUSSION

SAR-OCT has demonstrated a sensitivity to differences in control and 3xTg-AD mice due to their retinal scattering properties. It was imagined that differences in the retina might only be apparent in the later time points, but the data show that differences in the scattering properties are more apparent at the early time points. The first canonical variable for the central superficial layer is very interesting in that the values actually converge at the late stages of the disease, but begin with stark differences. The meaning of the first canonical variable is difficult to intuit, but the differences in the C parameter between groups yields more intuitive meaning. The C parameter differences between groups are also more apparent in the earlier time points than they are in the later time points.

Prior to this chapter in the dissertation, a decrease in C parameter has been shown to be correlated with (1) lower RGC density, (2) higher cell volume, (3) lower cellular uniformity, and (4) ischemic cell death. Mitochondrial fission and other cellular processes underlie some of these cellular states. In the case of the 3xTg-AD retina, any possible scattering changes were hypothesized to likely arise from the over-expression of APP, Aβ and/or tau deposition, neuronal cell loss, retinal glial cell changes, and vascular changes. The data clearly show differences between the groups at the youngest imaged age, 10 weeks. As mentioned in the introduction to this chapter, Aβ immunoreactivity is present in the hippocampus at 10 weeks.[139] Aβ is known to trigger neuronal cell loss via the apoptotic pathway.[146], [147] In particular, Aβ targets neuronal mitochondria and promotes mitochondrial fission, disruption of mitochondrial membrane potential, increase in intracellular reactive oxygen species levels, and activation of mitophagy.[148] This mitochondrial swelling, mitochondrial channel opening, and rupture can cause the release

of cytochrome c, which leads to necrosis or apoptosis.[148]–[150] Mitochondria are known to be major scatterers of light in cells, particularly at higher scattering angles.[151] Now, in terms of the four aforementioned correlated cellular states with lower C parameter values: increased rates of mitochondria-initiated apoptosis would lead to a decrease in cell density, particularly in RGCs,[28] and contribute to lower cellular uniformity and higher cell volume as cellular components are consumed. Taken together, it is a reasonable hypothesis that mitochondrial morphology is a contributing factor in differences between the 3xTg-AD model and the control group. Without extensive morphological analysis, it would be difficult to identify the exact causes of the scattering angle changes.

Another interesting feature apparent in this study is the variation of the C parameter with age. While it was not the aim of this study, age seems contribute to a decrease in the C parameter. This hypothesis was tested using one-way ANOVA, which indicated that several retinal regions and layers did, in fact, decrease with age (C parameter for 45 weeks < C parameter for 10 weeks; $p < 0.05$).

There are other retinal changes associated with age that seem to appear in the scattering data (C parameter). As the animal ages, the murine retina expands out, and the RGCs become less dense.[152] There are also fewer synaptic connections in any give IPL volume of older mouse retinas, and the area of RGC dendritic and axonal arbors decreases.[152] Overall, there is a general decrease in cellular and synaptic density. The C parameter also decreases with the age of the mouse in both groups (e.g. Figure 6.2). This evidence further corroborates the hypothesis that a decrease in cellular density is influencing a decrease in the C parameter.

The murine retina has also been shown to thin (axially) as it expands (laterally) in older mice, all while maintaining its volume.[150] Interestingly, the mice imaged in this study exhibited mean thickness values greater at older ages (3xTg-AD and control), though

not statistically different from young mice. This is likely due to experimental noise. An increase in retinal thickness is also in contrast to numerous clinical studies that report thinner retinas with aging human patients, particularly in the parapapillary RNFL.[153]–[157]

While the general decrease in retinal thickness with age was not apparent in this data, it is of interest that the statistically significant differences between the 3xTg-AD mice and the control mice are generally isolated to only two layers: (1) the superficial layers (RNFL + GCL + IPL) and (2) the ONL. As was described in Chapter 1, the RNFL, the IPL, and the OPL are the three layers of the murine retina that contain most of the retina's synapses; the other retinal layers contain mostly cell bodies. AD is known to affect the synapses in early disease states, so it makes sense that these layers would be significantly thinner in the 3xTg-AD model when compared to the control mice. This finding suggests that not only the thickness of the RNFL, but also the thickness of the IPL and the OPL could be used as indicators of neurodegeneration.

The reflectance index exhibited some differences in the central retina between the groups, but this difference disappears at later time points. Similar to the euthanasia experiments outlined in Chapter 5, the lower reflectance indices in the 3xTg-AD mice could be due to two causes: (1) lower RNFL reflectivity or (2) higher RPE reflectivity for 3xTg-AD mice when compared to their age-matched controls. It could be that the beginning stages of Aβ build-up in the young retina shifts the scattering profile in some voxels to more diverse scattering angles, and thus shifting more out of the collection NA. At later ages, shifts in neuronal density could overshadow this affect. Future histological analysis of the 3xTg-AD retina could be more instructive, but the data here are too sparse to draw strong conclusions.

CONCLUSIONS

In conclusion, the retinas of twenty 3xTg-AD mice and twelve control mice were imaged using SAR-OCT in a cross-sectional study. Four SAR-OCT feature regimes were examined for differences between the groups across time. Scattering differences between the 3xTg-AD and control groups were apparent at early ages, in both multivariate analysis and using only the C parameter of the fitted Burr distribution. Also, the C parameter decreased within the disease group alone. The thickness of the central retina was significantly less in the 3xTg-AD mice across all time points, and the central reflectance index exhibited some tempered differences in early age groups. The vasculature features examined in this study did not reveal meaningful differences between the 3xTg-AD and control mice. Taken together, this study suggests that SAR-OCT may be a useful tool for detecting early scattering changes in the retinas of patients developing Alzheimer's disease.

Chapter 7: Conclusions and Future Work

THE C PARAMETER

The C parameter is a new statistical approach for measuring retinal scattering angle changes with SAR-OCT. The C parameter is determined by fitting a Burr Type XII distribution to selected L/H_2 (pathlength 1/pathlength 2) values collected by an SAR-OCT system. The C parameter as an image feature is the major contribution of the dissertation. Prior to this work, SAR-OCT analysis had been limited in its utility by only considering the mean value across a region. Now, by statistically considering the properties of a tissue as a whole, the Burr distribution, and the C parameter in particular, have introduced a powerful method for OCT retinal imaging.

What makes the C parameter change?

In this dissertation, the C parameter of a mouse retina has been demonstrated to change depending on the retinal layer, region, or vascularization (Chapter 4), after ischemic insult (Chapter 5), and in the early stages of/with the development of AD (Chapter 6). With some assumptions, these various cellular changes and their impact on the C parameter are summarized in Table 7.1 and described below.

Retinal Morphology	Impact on the C parameter
Low cell density (e.g. superficial layers)	Low C value
High cell volume/swelling	Low C value
Highly structured cells	High C value
High cellular "entropy"	Low C value
Cell Death	Low C value
Alzheimer's disease • Mitochondrial Fission? • Aβ? • Tau?	Low C value

Table 7.1: Retinal cellular morphology and its impact on the C parameter.

The results of Chapter 4 indicated that the native low cell density and high cell volume peripheral regions of the retina have a lower C parameter. This echoes the Wang study that correlated a shift in the L/H_3 ratio with cellular density.[31] In the same chapter, layers of the retina that are known to be highly structured (RPE) had a significantly higher C parameter. This helps in the understanding of the C parameter as a measure of disorder. Disordered retinal structures should scatter with a broader distribution of L/H_2 values, which would yield a lower C parameter value. This is not the case of the RPE which has a C parameter around 9, whereas the C parameter value for more superficial layers of the retina is between 4 and 6.

While Chapter 5 did not offer much in the way of known morphological changes, the ischemic insult of the retina by isoflurane overdose does suggest some necrosis based on a survey of literature. It was discussed in Chapter 5 that necrosis, if that is indeed what

is taking place in the mouse retina during euthanasia, would lead to a decrease in the C parameter. Disjointed cell membranes, swollen mitochondria, and scattered cellular components would likely contribute to higher disorder.

Lastly, the 3xTg-AD cross-sectional study showed that the C parameter is lower for mice with AD—most significantly at early ages. The difference in the C parameter could be due to cellular disorder arising from mitochondrial fission, the presence of Aβ, or tau protein accumulation. Without extensive histological analysis, it would be difficult to tease apart their individual contributions.

Is there a C parameter floor?

The C parameter does seem to reach a floor around 5. In fact, the C parameter for the control mice and the 3xTg-AD mice seem to converge to around that value as both groups age (Figure 6.2). Thus, any discrimination between the late-stage AD mice and the old control mice is below the noise floor.

It is likely that the limiting factor is the discriminating power of the PME. Recall that in Chapter 2, the PME was shown to be able to discriminate backscattering angles up to around 8 degrees (Figure 2.10). Chapter 3 demonstrated that L/H_2 was sufficient to back-calculate the angle of bulk-backscattering angle up to 8 degrees. However, the L/H_2 ratio reaches a minimum of 0.69 (Figure 3.8).

A higher numerical aperture (NA) lens focusing light onto the retina could theoretically allow for discrimination of backscattering angles beyond 8 degrees and even lower L/H_2 values, but this might not be a practical solution as the NA of the SAR-OCT system designed here was already quite high in comparison to other reported systems. The ocular pupil and the axial length of the mouse eye from the pupil to the retina are the limiting factors.

ANGIOGRAPHY LIMITATIONS

The angiographic analysis performed in this dissertation, particularly the analysis in Chapter 6, was limited. The angiography image is highly dependent on the focal plane of the beam on the retina. Focusing the beam in the RNFL instead of the OPL could yield significantly difference angiography results, particularly for this SAR-OCT that had a high-NA objective to leverage the utility of the PME. Because of this, many of the angiography images had regions that were out-of-focus and produced poor angiography images. Thus, the angiography work performed here should not be interpreted as conclusive evidence for no vascular changes in 3xTg-AD mice.

FUTURE WORK

There are at least two directions this work could take as a result of this dissertation: (1) study if the C parameter is an appropriate measure of scattering properties in non-retinal tissues and (2) study the C parameter for other retinal pathologies with histological analysis.

First, it could be beneficial to analyze the utility of the PME and SAR-OCT for non-retinal imaging. Could the C parameter be used as a feature for detecting diseased tissue such as a brain tumor or skin cancer?

Lastly, other retinal pathologies should be examined with the C parameter to determine how specific this parameter is to neurodegeneration. Like other image features in OCT (e.g. RNFL thickness), it is possible that the C parameter might only be indicating that there is some kind of abnormality, and not specifying what it is. On the other hand, if the C parameter is particular to the introduction of new highly-scattering molecules like Aβ or tau protein tangles, then SAR-OCT could be a clinically viable route for early AD detection.

Appendices

APPENDIX A

Figure A.1 depicts the electrical layout of the SAR-OCT system, including the MEMS mirror.

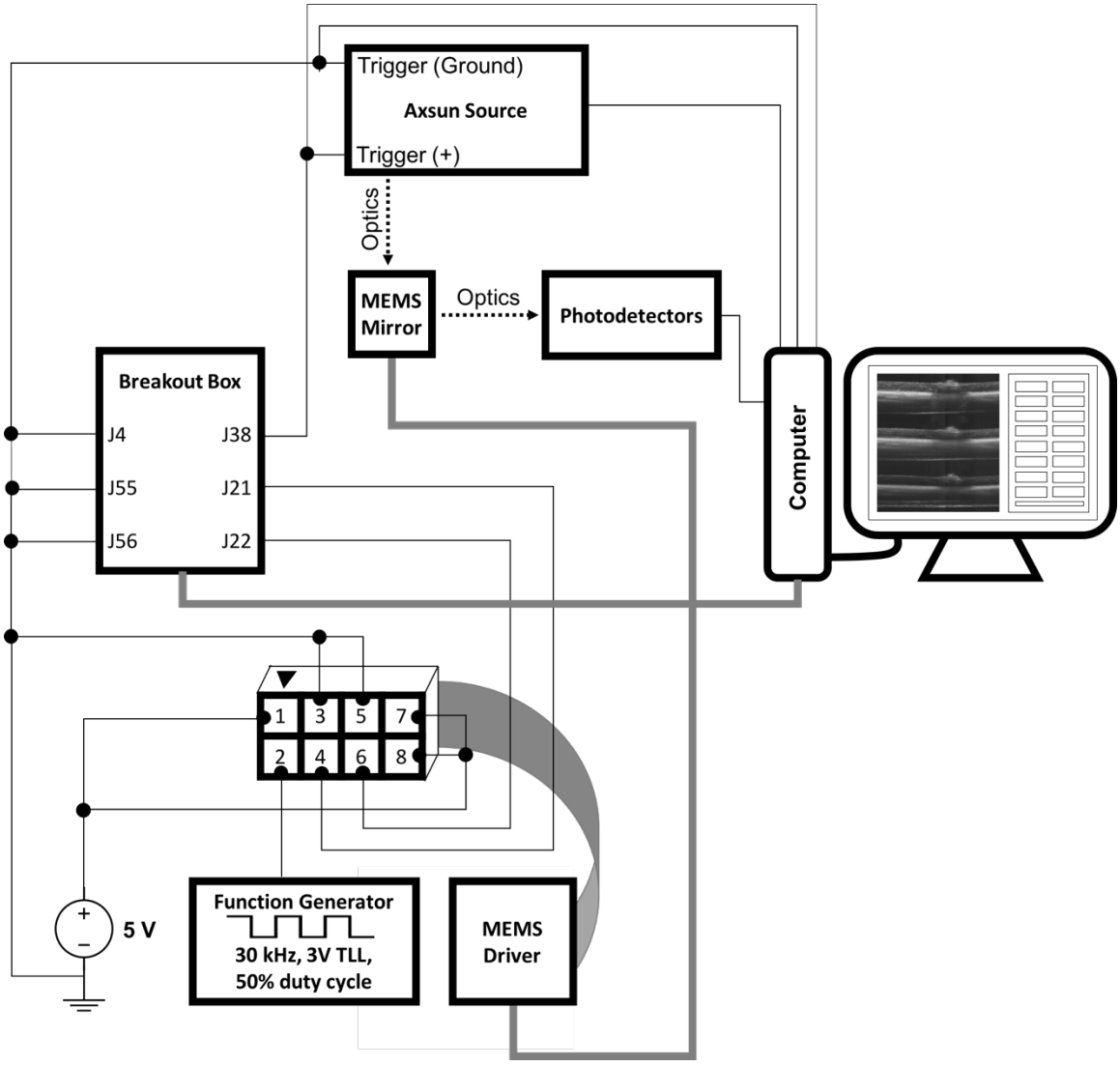

Figure A.1: A wiring diagram for the SAR-OCT system

APPENDIX B

MATLAB scripts developed for this dissertation may be accessed online as supplemental files at the Texas Digital Library.

APPENDIX C

Every output plot from the 3xTg-AD experiment (Chapter 6) is included in this Appendix (Figure C.1-C.10). These plots correspond to the rows in Tables 6.3-6.6.

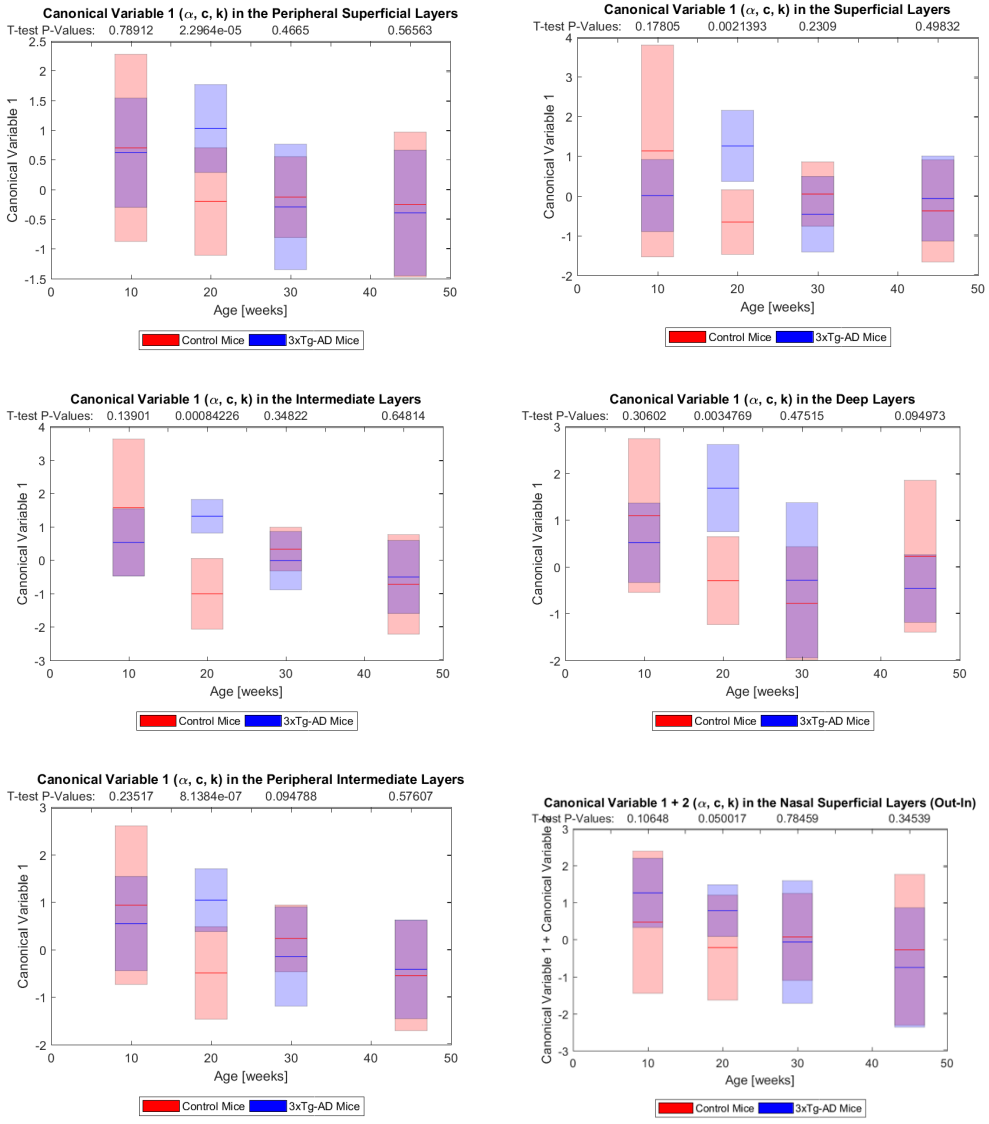

Figure C.1: Complete 3xTg-AD results (1/10)

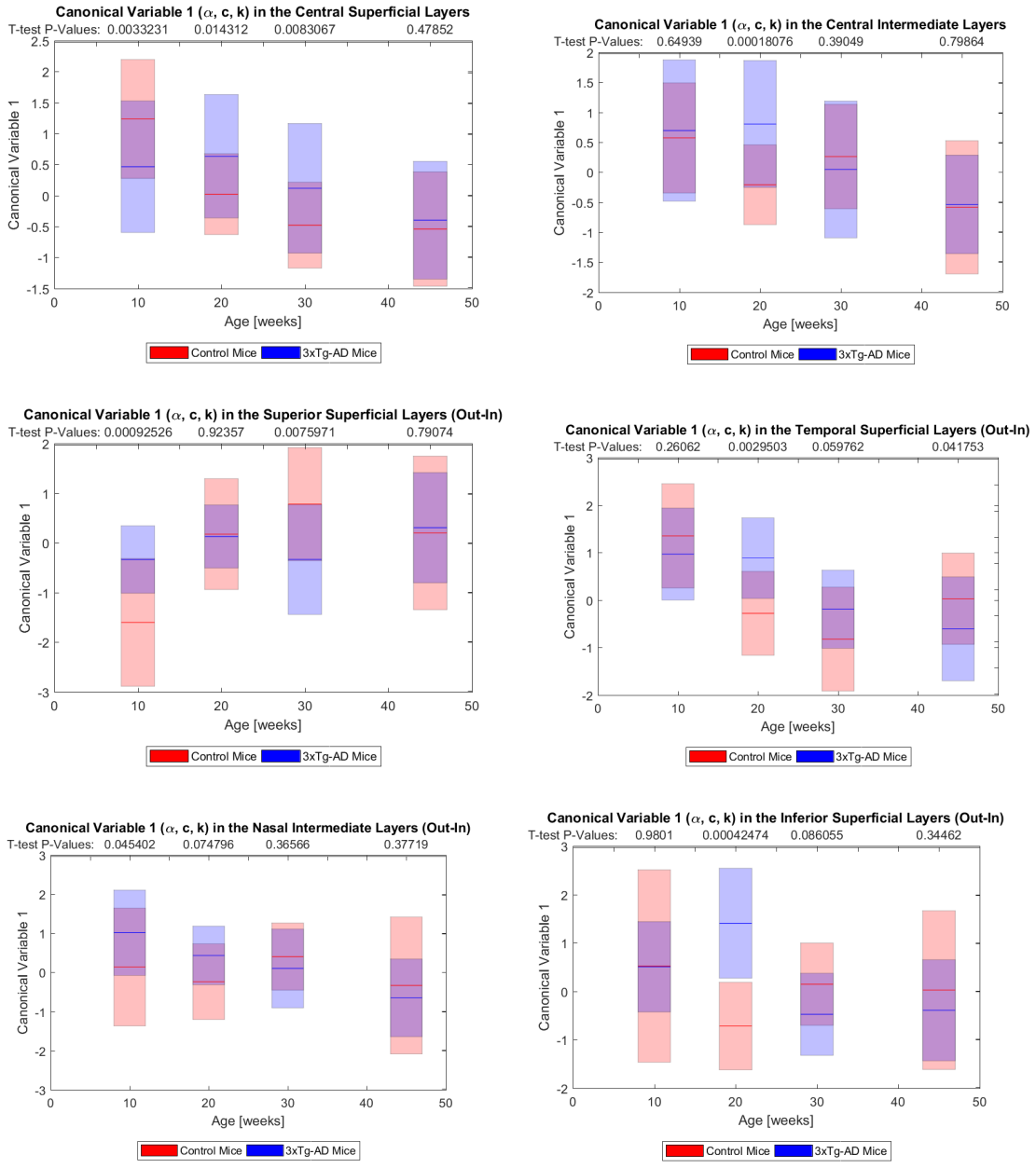

Figure C.2: Complete 3xTg-AD results (2/10)

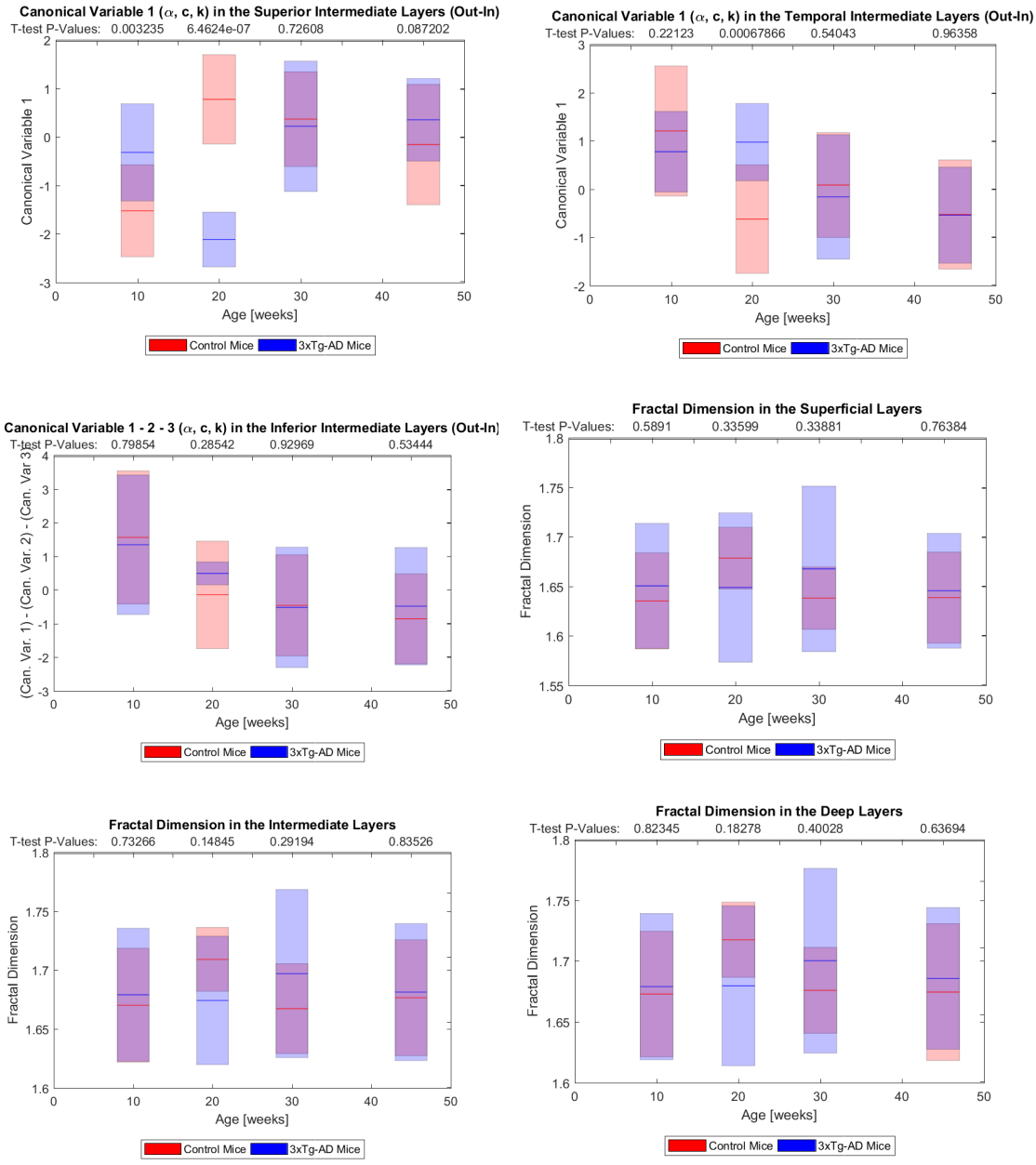

Figure C.3: Complete 3xTg-AD results (3/10)

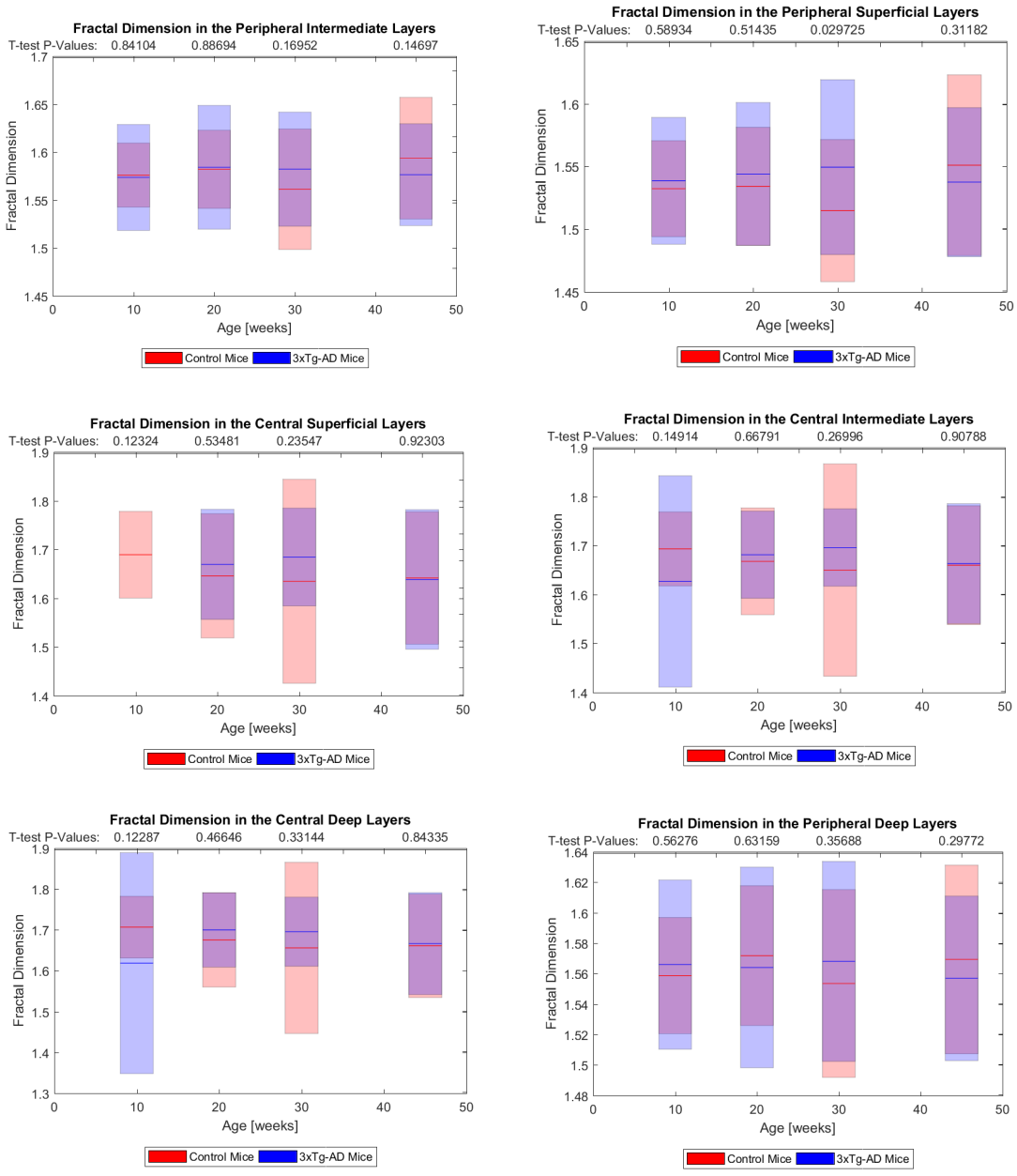

Figure C.4: Complete 3xTg-AD results (4/10)

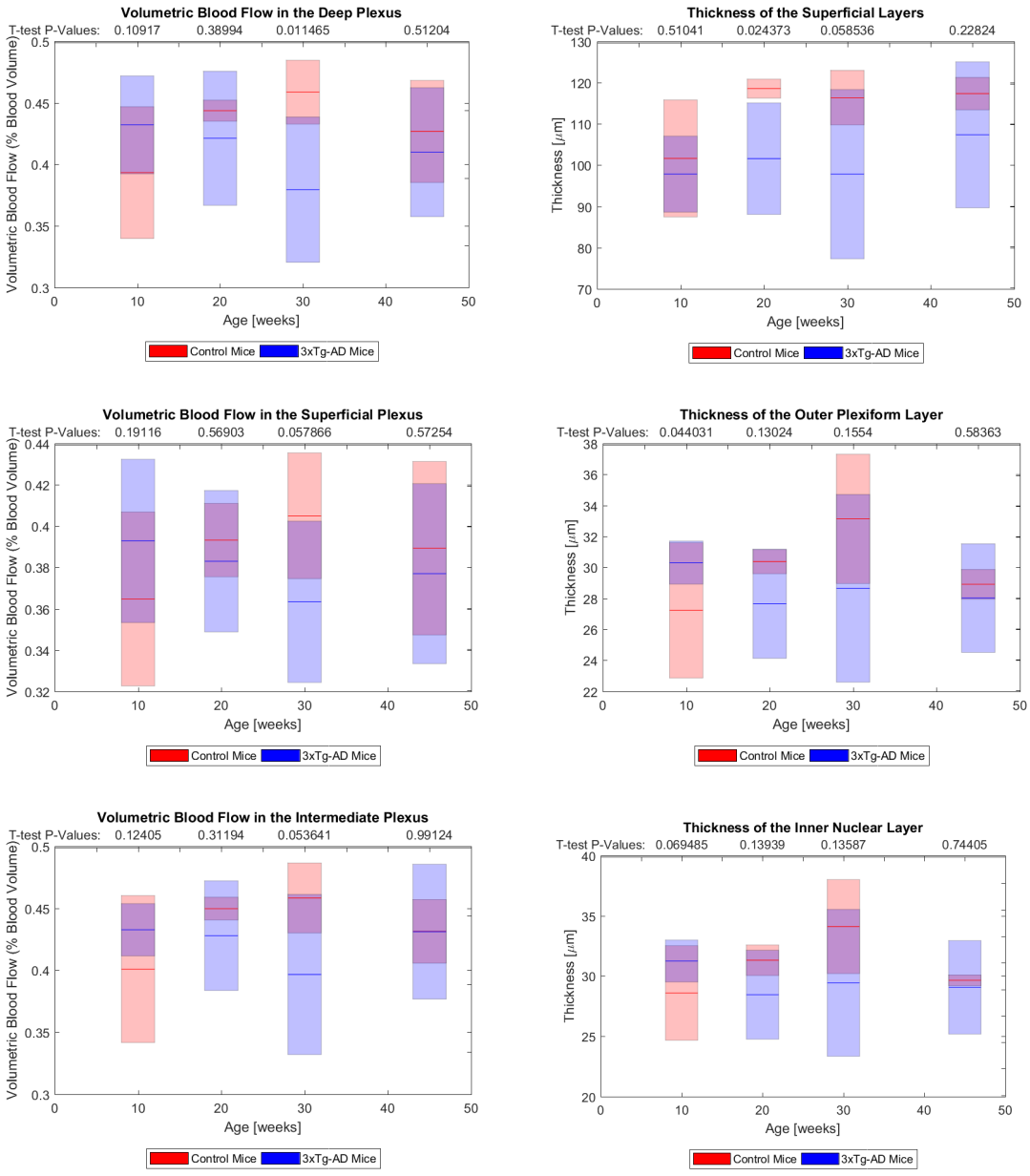

Figure C.5: Complete 3xTg-AD results (5/10)

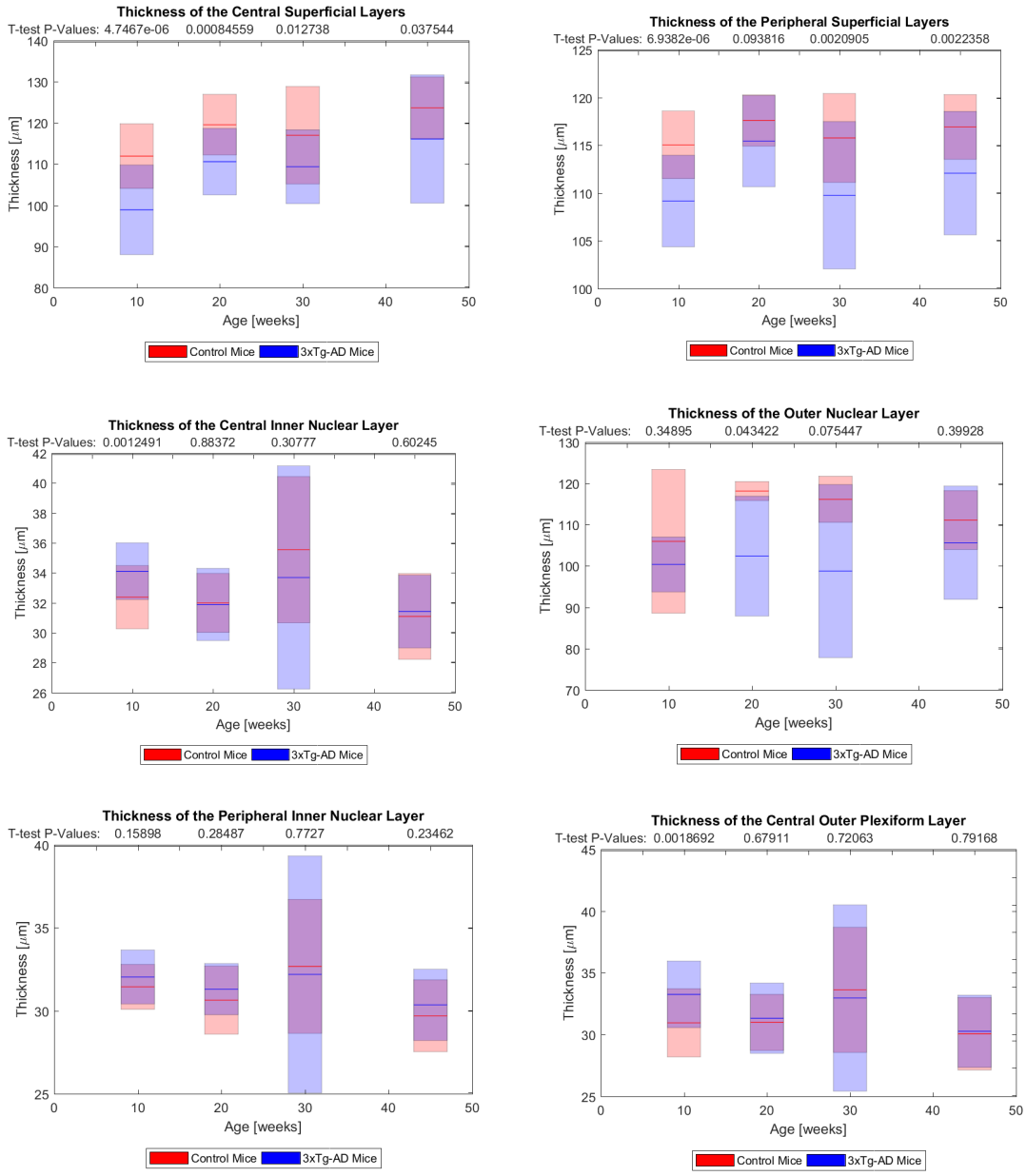

Figure C.6: Complete 3xTg-AD results (6/10)

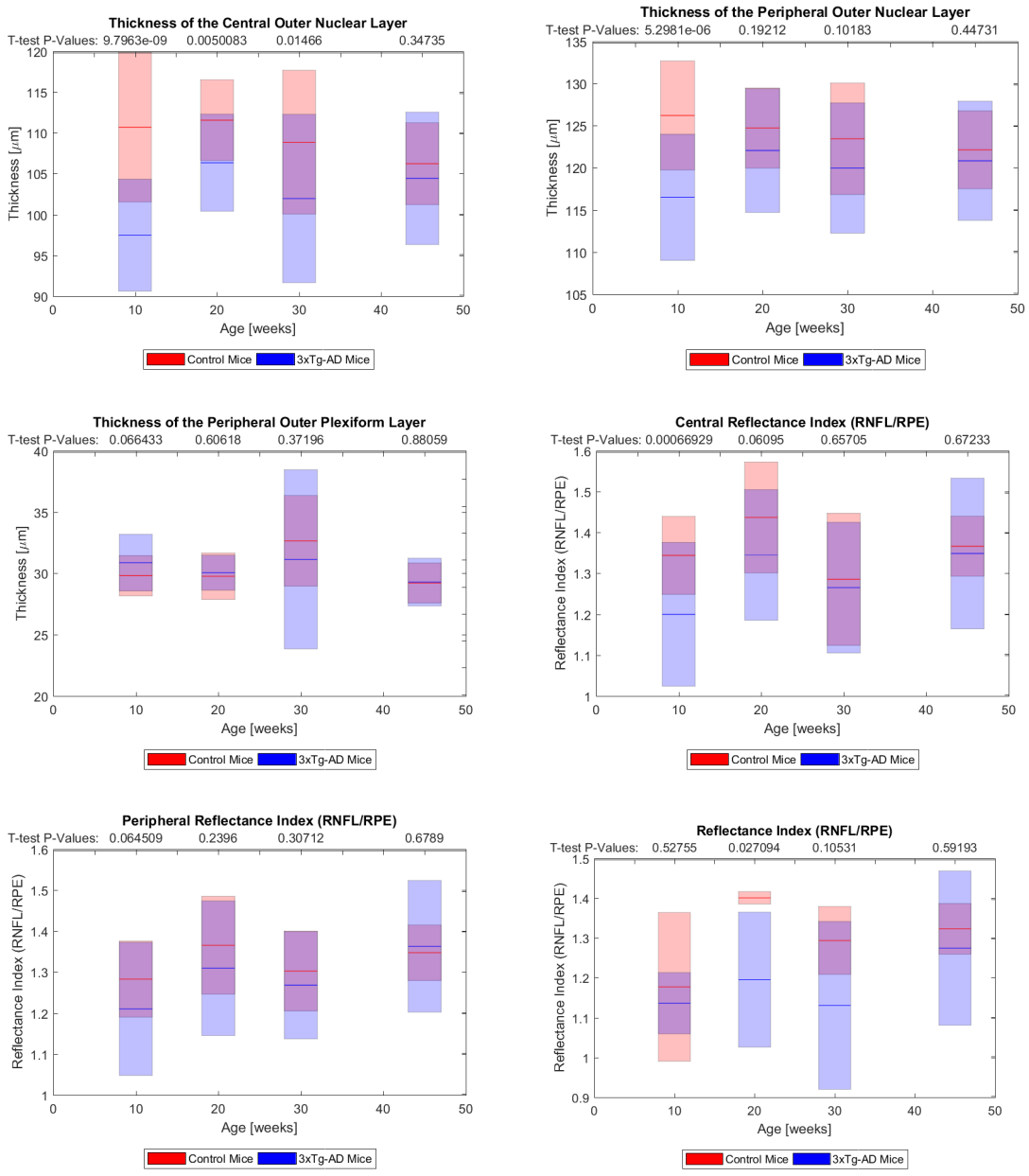

Figure C.7: Complete 3xTg-AD results (7/10)

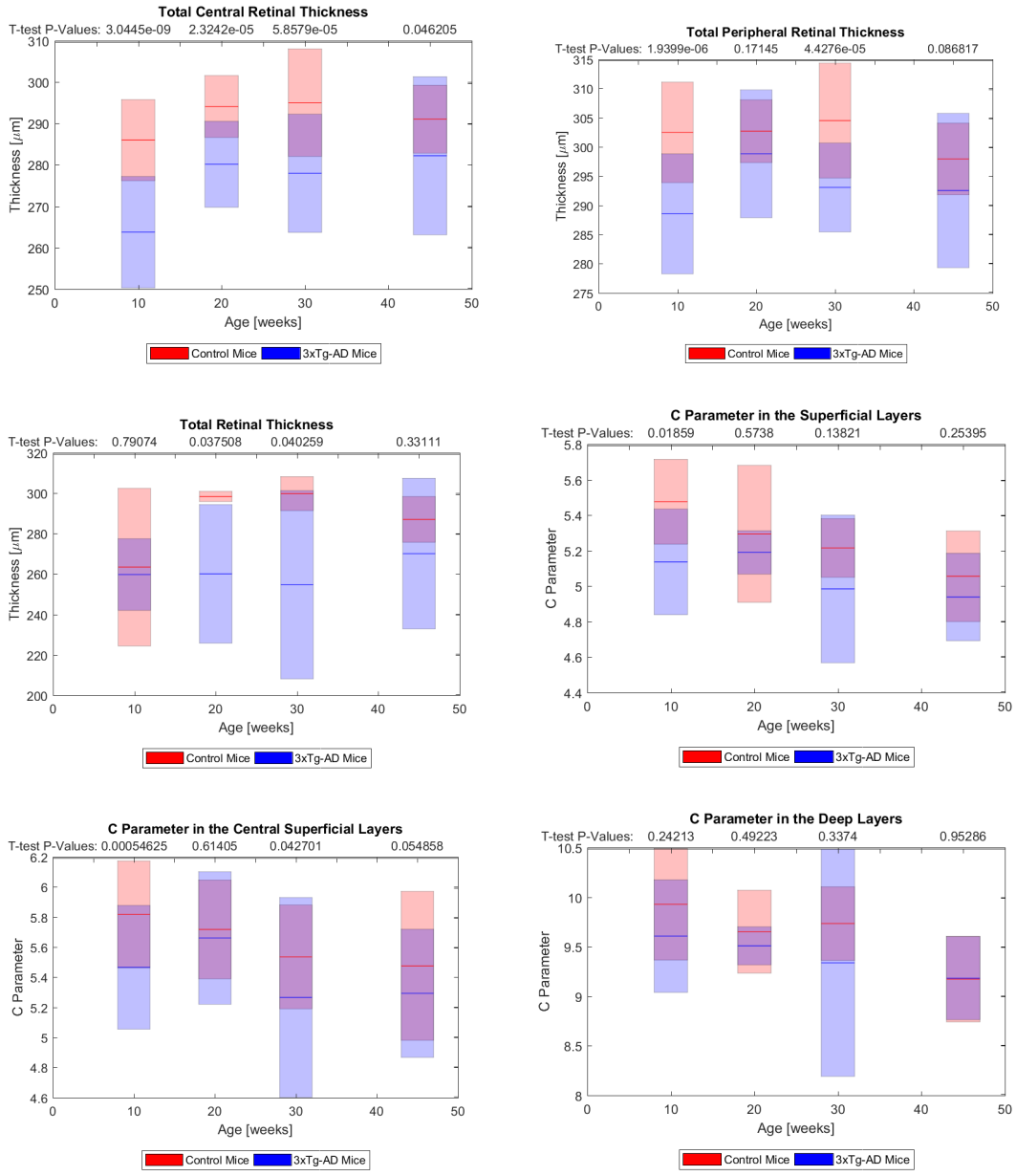

Figure C.8: Complete 3xTg-AD results (8/10)

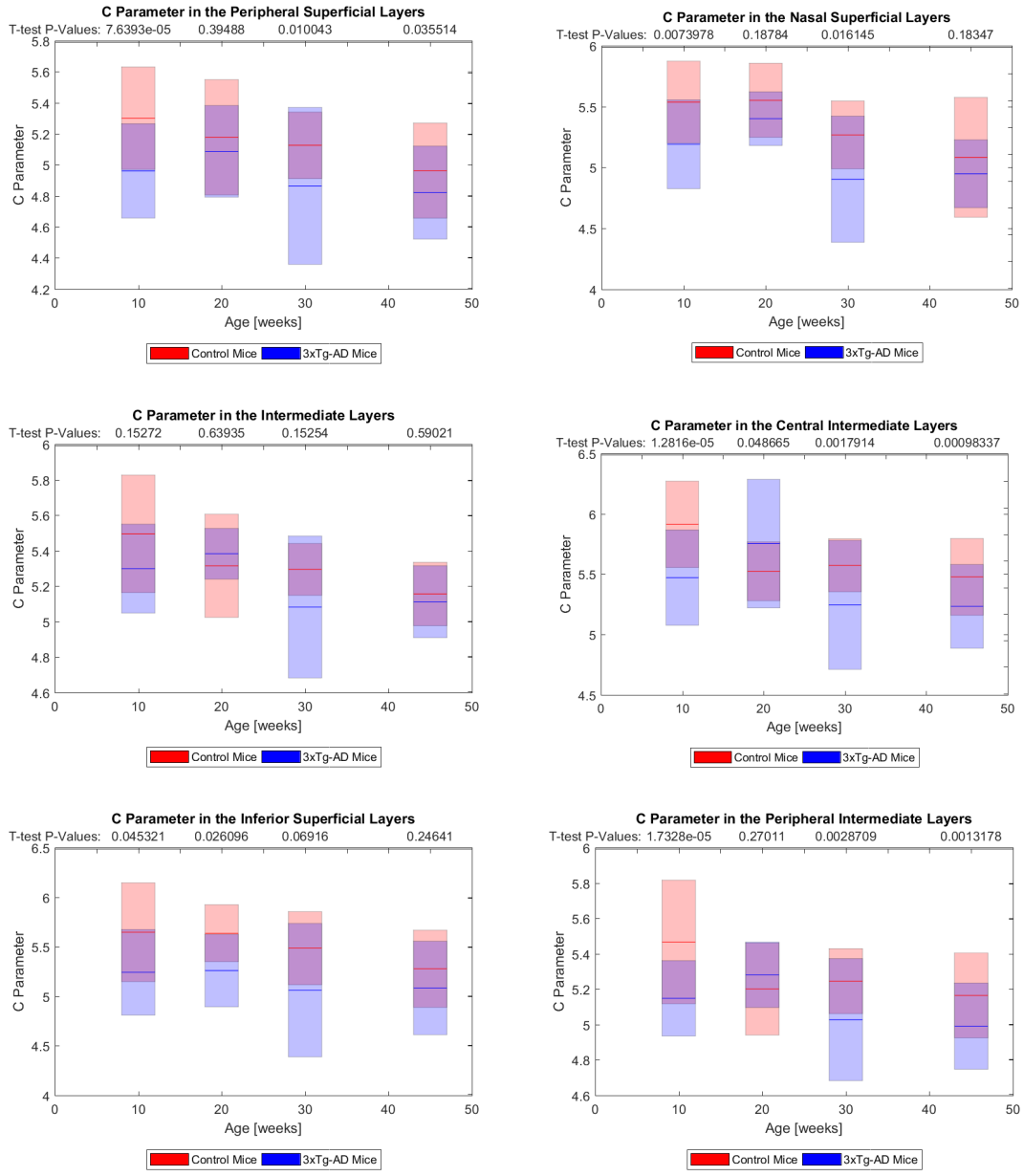

Figure C.9: Complete 3xTg-AD results (9/10)

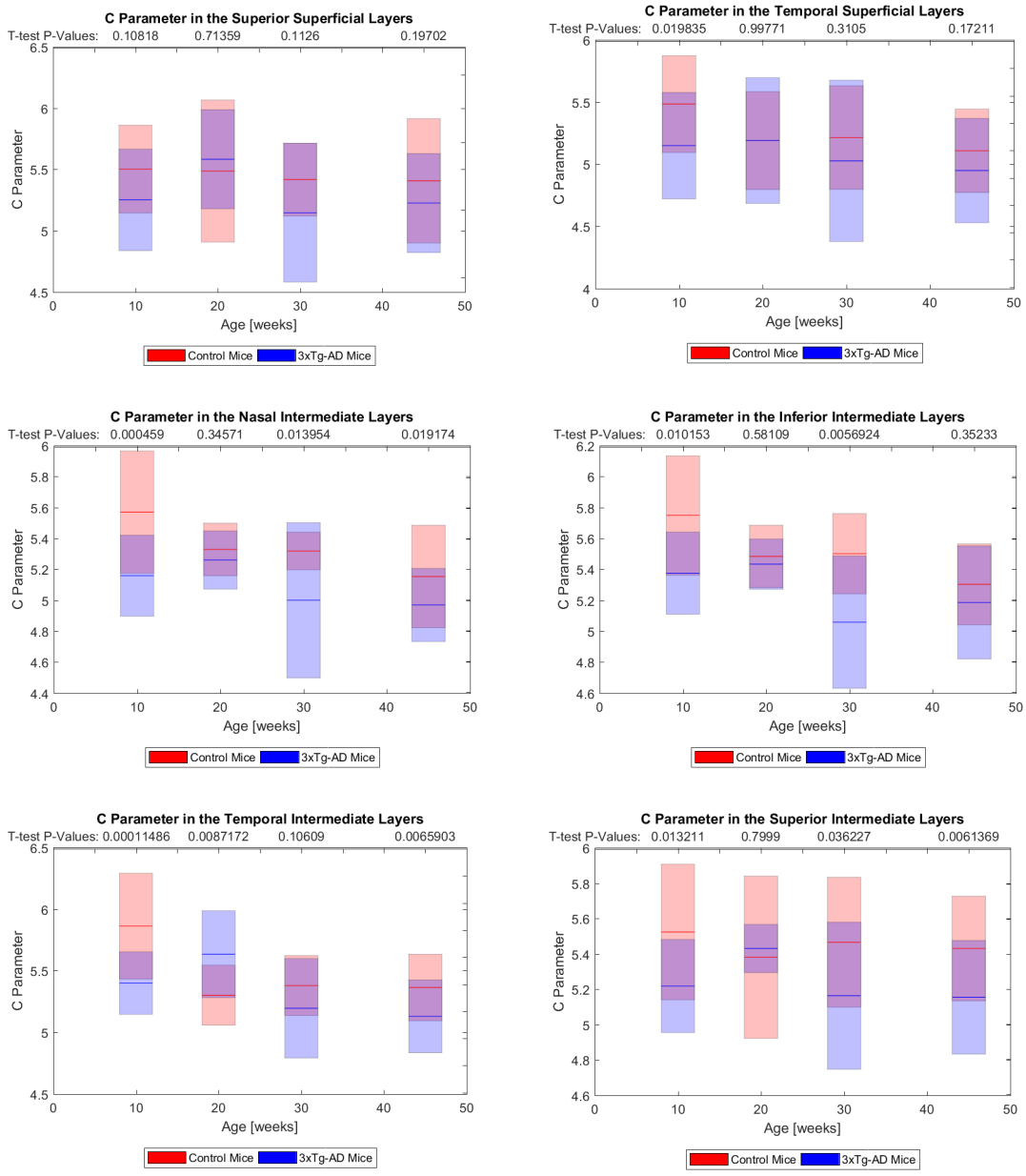

Figure C.10: Complete 3xTg-AD results (10/10)

Glossary

3

3xTg ..... *triple transgenic*

A

AD ..... *Alzheimer's disease*
ALS ..... *amyotrophic lateral sclerosis*
AR ..... *anti-reflective*
Aβ ..... *amyloid beta*

C

CAD ..... *computer-aided design*
CDV ..... *complex differential variance*
CRA ..... *central retinal artery*
CT ..... *computed tomography*

E

ELM ..... *external limiting membrane*

F

FFT ..... *Fast Fourier Transform*

G

GCL ..... *ganglion cell layer*
GDD ..... *group delay dispersion*

H

H_2 ..... *pathlength 2*
H_3 ..... *pathlength 3*
HD ..... *Huntington's disease*

I

ILM ..... *internal limiting membrane*
INL ..... *inner nuclear layer*
IPL ..... *inner plexiform layer*
IS ..... *inner segment*

L

L ..... *pathlength 1*

M

MANOVA ..... *multivariate analysis of variance*
MCI ..... *mild cognitive impairment*
MEMS ..... *microelectromechanical systems*
MS ..... *multiple sclerosis*

N

NA ..... *numerical aperture*

O

OA ..... *ophthalmic artery*
OCT ..... *optical coherence tomography*
OMAG ..... *optical microangiography*
ON ..... *optic nerve*
ONL ..... *outer nuclear layer*
OPL ..... *outer plexiform layer*
OS ..... *outer segment*

P

P1 ..... *pathlength 1 (L)*
P2 ..... *pathlength 2 (H_2)*
P3 ..... *pathlength 3 (H_3)*
PD ..... *Parkinson's disease*
PME ..... *pathlength multiplexing element*

R

RGCs ..... *retinal ganglion cell*
RNFL ..... *retinal nerve fiber layer*
RPE ..... *retinal pigment epithelium*

S

SAR ..... *scattering angle resolved*
SNR ..... *signal-to-noise ratio*
SSADA ..... *split-spectrum amplitude decorrelation angiography*

References

[1] N. Gupta and Y. H. Yucel, "Glaucoma as a neurodegenerative disease.," *Curr. Opin. Ophthalmol.*, vol. 18, no. 2, pp. 110–114, Mar. 2007.

[2] S. Przedborski, M. Vila, and V. Jackson-Lewis, "Series Introduction: Neurodegeneration: What is it and where are we?," *J. Clin. Invest.*, vol. 111, no. 1, pp. 3–10, Jan. 2003.

[3] Alzheimer Association, "2016 Alzheimer's Disease Facts and Figures," *Alzheimer's Dement. 2016*, vol. 12, no. 4, pp. 1–80, 2016.

[4] L. E. Hebert, J. Weuve, P. a. Scherr, and D. a. Evans, "Alzheimer disease in the United States (2010-2050) estimated using the 2010 census," *Neurology*, vol. 80, no. 19, pp. 1778–1783, May 2013.

[5] R. Siegel, J. Ma, Z. Zou, and A. Jemal, "Cancer statistics, 2014," *CA. Cancer J. Clin.*, vol. 64, no. 1, pp. 9–29, 2014.

[6] M. S. Albert *et al.*, "The diagnosis of mild cognitive impairment due to Alzheimer's disease: Recommendations from the National Institute on Aging-Alzheimer's Association workgroups on diagnostic guidelines for Alzheimer's disease," *Alzheimer's Dement. J. Alzheimer's Assoc.*, vol. 7, no. 3, pp. 270–279, Jul. 2016.

[7] R. A. Sperling *et al.*, "Toward defining the preclinical stages of Alzheimer's disease: recommendations from the National Institute on Aging-Alzheimer's Association workgroups on diagnostic guidelines for Alzheimer's disease.," *Alzheimers. Dement.*, vol. 7, no. 3, pp. 280–292, May 2011.

[8] C. R. Jack *et al.*, "Update on hypothetical model of Alzheimer's disease biomarkers," *Lancet Neurol.*, vol. 12, no. 2, pp. 207–216, Feb. 2013.

[9] V. L. Villemagne *et al.*, "Amyloid beta deposition, neurodegeneration, and cognitive decline in sporadic Alzheimer's disease: a prospective cohort study.," *Lancet. Neurol.*, vol. 12, no. 4, pp. 357–367, Apr. 2013.

[10] E. M. Reiman *et al.*, "Brain imaging and fluid biomarker analysis in young adults at genetic risk for autosomal dominant Alzheimer's disease in the presenilin 1 E280A kindred: a case-control study.," *Lancet. Neurol.*, vol. 11, no. 12, pp. 1048–1056, Dec. 2012.

[11] C. R. Jack *et al.*, "Serial PIB and MRI in normal, mild cognitive impairment and Alzheimer's disease: implications for sequence of pathological events in Alzheimer's disease," *Brain*, vol. 132, no. 5, pp. 1355–1365, May 2009.

[12] S. G. Mueller *et al.*, "Ways toward an early diagnosis in Alzheimer's disease: the Alzheimer's Disease Neuroimaging Initiative (ADNI).," *Alzheimers. Dement.*, vol. 1, no. 1, pp. 55–66, 2005.

[13] H. Liu-Seifert *et al.*, "Delayed-start analysis: Mild Alzheimer's disease patients in solanezumab trials, 3.5 years," *Alzheimer's Dement. Transl. Res. Clin. Interv.*, vol. 1, no. 2, pp. 111–121, Aug. 2016.

[14] R. Brookmeyer, E. Johnson, K. Ziegler-Graham, and H. M. Arrighi, "Forecasting

the global burden of Alzheimer's disease," *Alzheimer's Dement.*, vol. 3, pp. 186–191, 2007.
[15] O. Hansson, H. Zetterberg, P. Buchhave, E. Londos, K. Blennow, and L. Minthon, "Association between CSF biomarkers and incipient Alzheimer's disease in patients with mild cognitive impairment: a follow-up study.," *Lancet. Neurol.*, vol. 5, no. 3, pp. 228–234, Mar. 2006.
[16] S. L. Risacher, A. J. Saykin, J. D. West, L. Shen, H. A. Firpi, and B. C. McDonald, "Baseline MRI predictors of conversion from MCI to probable AD in the ADNI cohort.," *Curr. Alzheimer Res.*, vol. 6, no. 4, pp. 347–361, Aug. 2009.
[17] D. P. Perl, "Neuropathology of Alzheimer's disease.," *Mt. Sinai J. Med.*, vol. 77, no. 1, pp. 32–42, 2010.
[18] D. J. Selkoe, "Alzheimer's disease is a synaptic failure.," *Science*, vol. 298, no. October, pp. 789–791, 2002.
[19] H. Du, L. Guo, S. Yan, A. a Sosunov, G. M. McKhann, and S. S. Yan, "Early deficits in synaptic mitochondria in an Alzheimer's disease mouse model.," *Proc. Natl. Acad. Sci. U. S. A.*, vol. 107, no. 43, pp. 18670–18675, 2010.
[20] H.-Y. Wu *et al.*, "Amyloid beta induces the morphological neurodegenerative triad of spine loss, dendritic simplification, and neuritic dystrophies through calcineurin activation.," *J. Neurosci.*, vol. 30, no. 7, pp. 2636–2649, 2010.
[21] X. Wang *et al.*, "Impaired balance of mitochondrial fission and fusion in Alzheimer's disease.," *J. Neurosci.*, vol. 29, no. 28, pp. 9090–9103, 2009.
[22] R. H. Swerdlow, J. M. Burns, and S. M. Khan, "The Alzheimer's disease mitochondrial cascade hypothesis: Progress and perspectives," *Biochim. Biophys. Acta - Mol. Basis Dis.*, vol. 1842, no. 8, pp. 1219–1231, 2014.
[23] S. Oddo, L. Billings, J. P. Kesslak, D. H. Cribbs, and F. M. LaFerla, "AB Immunotherapy immunotherapy leads to clearance of early, but not late, hyperphosphorylated tau aggregates via the proteasome," *Neuron*, vol. 43, no. 3, pp. 321–332, 2004.
[24] A. Maresca, C. la Morgia, L. Caporali, M. L. Valentino, and V. Carelli, "The optic nerve: A 'mito-window' on mitochondrial neurodegeneration," *Mol. Cell. Neurosci.*, vol. 55, pp. 62–76, 2013.
[25] A. London, I. Benhar, and M. Schwartz, "The retina as a window to the brain - from eye research to CNS disorders," *Nat Rev Neurol*, vol. 9, no. 1, pp. 44–53, Jan. 2013.
[26] A. Petzold *et al.*, "Optical coherence tomography in multiple sclerosis: A systematic review and meta-analysis," *Lancet Neurol.*, vol. 9, no. 9, pp. 921–932, 2010.
[27] N. K. Archibald, M. P. Clarke, U. P. Mosimann, and D. J. Burn, "The retina in Parkinsons disease," *Brain*, vol. 132, pp. 1128–1145, 2009.
[28] L. Guo, J. Duggan, and M. F. Cordeiro, "Alzheimer's Disease and Retinal Neurodegeneration," *Curr. Alzheimer Res.*, vol. 7, no. 1, pp. 3–14, Feb. 2010.
[29] J. Dwelle *et al.*, "Thickness, phase retardation, birefringence, and reflectance of the retinal nerve fiber layer in normal and glaucomatous non-human primates,"

Investig. Ophthalmol. Vis. Sci., vol. 53, no. 8, pp. 4380–4395, Jul. 2012.
[30] S. Liu *et al.*, "Retinal nerve fiber layer reflectance for early glaucoma diagnosis," *J. Glaucoma*, vol. 23, no. 1, 2014.
[31] B. Wang, B. Yin, J. Dwelle, H. G. Rylander, M. K. Markey, and T. E. Milner, "Path-length-multiplexed scattering-angle-diverse optical coherence tomography for retinal imaging," *Opt. Lett.*, vol. 38, no. 21, pp. 4374–4377, 2013.
[32] K. Santacruz *et al.*, "Tau suppression in a neurodegenerative mouse model improves memory function.," *Science*, vol. 309, no. 5733, pp. 476–481, Jul. 2005.
[33] D. Huang *et al.*, "Optical coherence tomography," *Science*, vol. 254, no. 5035. pp. 1178–1181, 1991.
[34] Y. Dong, J. Zhang, Y. Shen, K. Su, and J. A. Zeitler, "Non-destructive characterization of automobile car paints using terahertz pulsed imaging and infrared optical coherence tomography," in *40th International Conference on Infrared, Millimeter, and Terahertz waves (IRMMW-THz)*, 2015, pp. 1–2.
[35] J. Zhang *et al.*, "Non-destructive analysis of flake properties in automotive paints with full-field optical coherence tomography and 3D segmentation," *Opt. Express*, vol. 25, no. 16, pp. 18614–18628, 2017.
[36] N. H. Cho, K. Park, J.-Y. Kim, Y. Jung, and J. Kim, "Quantitative assessment of touch-screen panel by nondestructive inspection with three-dimensional real-time display optical coherence tomography," *Opt. Lasers Eng.*, vol. 68, pp. 50–57, 2015.
[37] Z. Chen, Y. Shen, W. Bao, P. Li, X. Wang, and Z. Ding, "Identification of surface defects on glass by parallel spectral domain optical coherence tomography," *Opt. Express*, vol. 23, no. 18, pp. 23634–23646, 2015.
[38] C. Li, J. A. Zeitler, Y. Dong, and Y. Shen, "Non-Destructive Evaluation of Polymer Coating Structures on Pharmaceutical Pellets Using Full-Field Optical Coherence Tomography," *J. Pharm. Sci.*, vol. 103, no. 1, pp. 161–166, 2014.
[39] A. Lewis, M. Gardner, A. McElroy, T. Milner, S. Fish, and J. Beaman, "In-situ process monitoring and ex-situ part quality assessment of selective laser sintering using optical coherence tomography," in *Proceedings of the 27th International SFF Symposium-An Additive Manufacturing Conference*, 2016, pp. 1397–411.
[40] M. R. Gardner *et al.*, "In situ process monitoring in selective laser sintering using optical coherence tomography," *Opt. Eng.*, vol. 57, no. 4, p. 41407, 2018.
[41] M. Cilingiroglu *et al.*, "Detection of vulnerable plaque in a murine model of atherosclerosis with optical coherence tomography," *Catheter. Cardiovasc. Interv.*, vol. 67, no. 6, pp. 915–923, 2006.
[42] M. G. Ducros *et al.*, "Polarization sensitive optical coherence tomography of the rabbit eye," *IEEE J. Sel. Top. Quantum Electron.*, vol. 5, no. 4, pp. 1159–1167, 1999.
[43] J. Barrick, A. Doblas, M. R. Gardner, P. R. Sears, L. E. Ostrowski, and A. L. Oldenburg, "High-speed and high-sensitivity parallel spectral-domain optical coherence tomography using a supercontinuum light source," *Opt. Lett.*, vol. 41, no. 24, pp. 5620–5623, 2016.

[44] N. Katta *et al*., "Image-guided smart laser system for precision implantation of cells in cartilage," in *SPIE Medical Imaging*, 2017, p. 101350V–101350V.
[45] H. H. Gilgen, R. P. Novak, R. P. Salathe, W. Hodel, and P. Beaud, "Submillimeter optical reflectometry," *J. Light. Technol.*, vol. 7, no. 8, pp. 1225–1233, 1989.
[46] R. C. Youngquist, S. Carr, and D. E. N. Davies, "Optical coherence-domain reflectometry: a new optical evaluation technique," *Opt. Lett.*, vol. 12, no. 3, pp. 158–160, 1987.
[47] K. Takada, I. Yokohama, K. Chida, and J. Noda, "New measurement system for fault location in optical waveguide devices based on an interferometric technique," *Appl. Opt.*, vol. 26, no. 9, pp. 1603–1606, 1987.
[48] J. M. Schmitt, A. Knüttel, and R. F. Bonner, "Measurement of optical properties of biological tissues by low-coherence reflectometry," *Appl. Opt.*, vol. 32, no. 30, pp. 6032–6042, 1993.
[49] X. Clivaz, F. Marquis-Weible, and R. P. Salathe, "Optical low coherence reflectometry with 1.9 mu m spatial resolution," *Electron. Lett.*, vol. 28, no. 16, pp. 1553–1555, 1992.
[50] D. Huang, J. Wang, C. P. Lin, C. A. Puliafito, and J. G. Fujimoto, "Micron-resolution ranging of cornea anterior chamber by optical reflectometry.," *Lasers Surg. Med.*, vol. 11, no. 5, pp. 419–425, 1991.
[51] W. Drexler and J. G. Fujimoto, *Optical coherence tomography: technology and applications*. Springer Science & Business Media, 2008.
[52] C. Dysli, V. Enzmann, R. Sznitman, and M. S. Zinkernagel, "Quantitative analysis of mouse retinal layers using automated segmentation of spectral domain optical coherence tomography images," *Transl. Vis. Sci. Technol.*, vol. 4, no. 4, p. 9, 2015.
[53] F. Wang, W. Tang, H. M. McGraw, J. Bennett, L. W. Enquist, and H. M. Friedman, "Herpes simplex virus type 1 glycoprotein e is required for axonal localization of capsid, tegument, and membrane glycoproteins," *J. Virol.*, vol. 79, no. 21, pp. 13362–13372, 2005.
[54] M. W. Country, "Retinal metabolism: A comparative look at energetics in the retina," *Brain Res.*, vol. 1672, pp. 50–57, 2017.
[55] A. Ames III, "Energy requirements of CNS cells as related to their function and to their vulnerability to ischemia: a commentary based on studies on retina," *Can. J. Physiol. Pharmacol.*, vol. 70, no. S1, pp. S158–S164, 1992.
[56] M. Wong-Riley, "Energy metabolism of the visual system," *Eye Brain*, vol. 2, p. 99, 2010.
[57] J. E. Dowling, *The retina: an approachable part of the brain*. Harvard University Press, 1987.
[58] D.-Y. Yu and S. J. Cringle, "Oxygen distribution and consumption within the retina in vascularised and avascular retinas and in animal models of retinal disease," *Prog. Retin. Eye Res.*, vol. 20, no. 2, pp. 175–208, 2001.
[59] M. Schmidt, A. Giessl, T. Laufs, T. Hankeln, U. Wolfrum, and T. Burmester, "How does the eye breathe? Evidence for neuroglobin-mediated oxygen supply in the mammalian retina," *J. Biol. Chem.*, vol. 278, no. 3, pp. 1932–1935, 2003.

[60] A. Bentmann, M. Schmidt, S. Reuss, U. Wolfrum, T. Hankeln, and T. Burmester, "Divergent distribution in vascular and avascular mammalian retinae links neuroglobin to cellular respiration," *J. Biol. Chem.*, vol. 280, no. 21, pp. 20660–20665, 2005.
[61] J. Chase, "The evolution of retinal vascularization in mammals: a comparison of vascular and avascular retinae," *Ophthalmology*, vol. 89, no. 12, pp. 1518–1525, 1982.
[62] S. Hughes, H. Yang, and T. Chan-Ling, "Vascularization of the human fetal retina: roles of vasculogenesis and angiogenesis.," *Invest. Ophthalmol. Vis. Sci.*, vol. 41, no. 5, pp. 1217–1228, Apr. 2000.
[63] S. E. Connolly, T. A. Hores, L. E. Smith, and P. A. D'Amore, "Characterization of vascular development in the mouse retina.," *Microvasc. Res.*, vol. 36, no. 3, pp. 275–290, Nov. 1988.
[64] C. A. May and E. Lütjen-Drecoll, "Morphology of the murine optic nerve," *Invest. Ophthalmol. Vis. Sci.*, vol. 43, no. 7, pp. 2206–2212, 2002.
[65] S. Kim *et al.*, "Analyzing spatial correlations in tissue using angle-resolved low coherence interferometry measurements guided by co-located optical coherence tomography," *Biomed. Opt. Express*, vol. 7, no. 4, p. 1400, 2016.
[66] A. Wax *et al.*, "Cellular Organization and Substructure Measured Using Angle-Resolved Low-Coherence Interferometry," *Biophys. J.*, vol. 82, no. 4, pp. 2256–2264, Apr. 2002.
[67] Y. Geng *et al.*, "Optical properties of the mouse eye.," *Biomed. Opt. Express*, vol. 2, no. 4, pp. 717–738, 2011.
[68] S. Remtulla and P. E. Hallett, "A schematic eye for the mouse, and comparisons with the rat," *Vision Res.*, vol. 25, no. 1, pp. 21–31, 1985.
[69] C. Schmucker and F. Schaeffel, "A paraxial schematic eye model for the growing C57BL/6 mouse," *Vision Res.*, vol. 44, no. 16, pp. 1857–1867, Jul. 2004.
[70] A. E. Conrady, *Applied Optics and Optical Design, Part Two*, 1st ed. New York: Dover Publications, Inc., 1960.
[71] E. A. Swanson *et al.*, "In vivo retinal imaging by optical coherence tomography," *Opt. Lett.*, vol. 18, no. 21, pp. 1864–1866, 1993.
[72] O. Carrasco-Zevallos, D. Nankivil, B. Keller, C. Viehland, B. J. Lujan, and J. A. Izatt, "Pupil tracking optical coherence tomography for precise control of pupil entry position," *Biomed. Opt. Express*, vol. 6, no. 9, pp. 3405–3419, 2015.
[73] K. Kumar *et al.*, "Fast 3D in vivo swept-source optical coherence tomography using a two-axis MEMS scanning micromirror," *J. Opt. A Pure Appl. Opt.*, vol. 10, no. 4, p. 44013, 2008.
[74] A. D. Aguirre *et al.*, "Two-axis MEMS scanning catheter for ultrahigh resolution three-dimensional and en face imaging," *Opt. Express*, vol. 15, no. 5, pp. 2445–2453, 2007.
[75] C. D. Lu *et al.*, "Handheld ultrahigh speed swept source optical coherence tomography instrument using a MEMS scanning mirror," *Biomed. Opt. Express*, vol. 5, no. 1, pp. 293–311, 2014.

[76] F. LaRocca, D. Nankivil, T. DuBose, C. A. Toth, S. Farsiu, and J. A. Izatt, "In vivo cellular-resolution retinal imaging in infants and children using an ultracompact handheld probe," *Nat. Photonics*, vol. 10, pp. 580–584, Aug. 2016.
[77] M. R. Gardner, N. Katta, A. McElroy, V. Baruah, H. G. Rylander, and T. E. Milner, "Scattering angle resolved optical coherence tomography for in vivo murine retinal imaging," in *SPIE BiOS*, 2017, p. 100531O–100531O.
[78] E. G. de la Cera, G. Rodríguez, L. Llorente, F. Schaeffel, and S. Marcos, "Optical aberrations in the mouse eye," *Vision Res.*, vol. 46, no. 16, pp. 2546–2553, 2006.
[79] Y. Yu, T. Zhang, A. Meadway, X. Wang, and Y. Zhang, "High-speed adaptive optics for imaging of the living human eye," *Opt. Express*, vol. 23, no. 18, pp. 23035–23052, Sep. 2015.
[80] R. J. Zawadzki *et al.*, "Adaptive-optics optical coherence tomography for high-resolution and high-speed 3D retinal in vivo imaging," *Opt. Express*, vol. 13, no. 21, pp. 8532–8546, 2005.
[81] Y. Jian, J. Xu, M. A. Gradowski, S. Bonora, R. J. Zawadzki, and M. V Sarunic, "Wavefront sensorless adaptive optics optical coherence tomography for in vivo retinal imaging in mice," *Biomed. Opt. Express*, vol. 5, no. 2, pp. 547–559, 2014.
[82] Y. Jian, R. J. Zawadzki, and M. V Sarunic, "Adaptive optics optical coherence tomography for in vivo mouse retinal imaging," *J. Biomed. Opt.*, vol. 18, no. 5, p. 56007, 2013.
[83] M. Hammer, A. Roggan, D. Schweitzer, and G. Muller, "Optical properties of ocular fundus tissues-an in vitro study using the double-integrating-sphere technique and inverse Monte Carlo simulation," *Phys. Med. Biol.*, vol. 40, no. 6, p. 963, 1995.
[84] Z. Chen *et al.*, "Noninvasive imaging of in vivo blood flow velocity using optical Doppler tomography," *Opt. Lett.*, vol. 22, no. 14, pp. 1119–1121, 1997.
[85] J. A. Izatt, M. D. Kulkarni, S. Yazdanfar, J. K. Barton, and A. J. Welch, "In vivo bidirectional color Doppler flow imaging of picoliter blood volumes using optical coherence tomography," *Opt. Lett.*, vol. 22, no. 18, pp. 1439–1441, 1997.
[86] H. C. Hendargo, R. P. McNabb, A.-H. Dhalla, N. Shepherd, and J. A. Izatt, "Doppler velocity detection limitations in spectrometer-based versus swept-source optical coherence tomography," *Biomed. Opt. Express*, vol. 2, no. 8, pp. 2175–2188, 2011.
[87] A. Mariampillai *et al.*, "Speckle variance detection of microvasculature using swept-source optical coherence tomography," *Opt. Lett.*, vol. 33, no. 13, pp. 1530–1532, 2008.
[88] C. Blatter *et al.*, "Ultrahigh-speed non-invasive widefield angiography," vol. 17, no., pp. 70504–70505, 2012.
[89] Y. Huang *et al.*, "Swept-source OCT angiography of the retinal vasculature using intensity differentiation-based optical microangiography algorithms," *Ophthalmic Surgery, Lasers Imaging Retin.*, 2014.
[90] Y. Yasuno *et al.*, "In vivo high-contrast imaging of deep posterior eye by 1-μm swept source optical coherence tomography and scattering optical coherence

angiography," *Opt. Express*, vol. 15, no. 10, pp. 6121–6139, 2007.
[91] J. Enock, E. Joey, and L. M. J., "Correlation mapping method for generating microcirculation morphology from optical coherence tomography (OCT) intensity images," *J. Biophotonics*, vol. 4, no. 9, pp. 583–587, Dec. 2010.
[92] Y. Jia *et al.*, "Split-spectrum amplitude-decorrelation angiography with optical coherence tomography," *Opt. Express*, vol. 20, no. 4, pp. 4710–4725, Feb. 2012.
[93] L. An, J. Qin, and R. K. Wang, "Ultrahigh sensitive optical microangiography for in vivo imaging of microcirculations within human skin tissue beds," *Opt. Express*, vol. 18, no. 8, pp. 8220–8228, 2010.
[94] A. S. Nam, I. Chico-Calero, and B. J. Vakoc, "Complex differential variance algorithm for optical coherence tomography angiography," *Biomed. Opt. Express*, vol. 5, no. 11, pp. 3822–3832, 2014.
[95] A. F. Frangi, W. J. Niessen, K. L. Vincken, and M. A. Viergever, "Multiscale vessel enhancement filtering," in *International Conference on Medical Image Computing and Computer-Assisted Intervention*, 1998, pp. 130–137.
[96] J. B. Fisher *et al.*, "Relation of Visual Function to Retinal Nerve Fiber Layer Thickness in Multiple Sclerosis," *Ophthalmology*, vol. 113, no. 2, pp. 324–332, Mar. 2018.
[97] H. A. Quigley, C. Enger, J. Katz, A. Sommer, R. Scott, and D. Gilbert, "Risk factors for the development of glaucomatous visual field loss in ocular hypertension," *Arch. Ophthalmol.*, vol. 112, p. 644, 1994.
[98] H. A. Quigley, G. R. Dunkelberger, and W. R. Green, "Retinal ganglion cell atrophy correlated with automated perimetry in human eyes with glaucoma," *Am. J. Ophthalmol.*, vol. 107, no. 5, pp. 453–464, 1989.
[99] H. A. Quigley, E. M. Addicks, and W. R. Green, "Optic nerve damage in human glaucoma: III. Quantitative correlation of nerve fiber loss and visual field defect in glaucoma, ischemic neuropathy, papilledema, and toxic neuropathy," *Arch. Ophthalmol.*, vol. 100, no. 1, pp. 135–146, 1982.
[100] A. Sommer *et al.*, "Clinically detectable nerve fiber atrophy precedes the onset of glaucomatous field loss," *Arch. Ophthalmol.*, vol. 109, no. 1, pp. 77–83, 1991.
[101] A. Sommer, N. R. Miller, I. Pollack, A. E. Maumenee, and T. George, "The nerve fiber layer in the diagnosis of glaucoma," *Arch ophthalmol*, vol. 95, no. 12, pp. 2149–2156, 1977.
[102] P. J. Airaksinen and H. I. Alanko, "Effect of retinal nerve fibre loss on the optic nerve head configuration in early glaucoma," *Graefe's Arch. Clin. Exp. Ophthalmol.*, vol. 220, no. 4, pp. 193–196, 1983.
[103] C. Bowd, W. RN, W. JM, and Z. LM, "The retinal nerve fiber layer thickness in ocular hypertensive, normal, and glaucomatous eyes with optical coherence tomography," *Arch. Ophthalmol.*, vol. 118, no. 1, pp. 22–26, Jan. 2000.
[104] S. Kirbas, K. Turkyilmaz, O. Anlar, A. Tufekci, and M. Durmus, "Retinal nerve fiber layer thickness in patients with Alzheimer disease," *J. Neuro-ophthalmology*, vol. 33, no. 1, pp. 58–61, 2013.
[105] Y. Lu *et al.*, "Retinal nerve fiber layer structure abnormalities in early Alzheimer's

disease: Evidence in optical coherence tomography," *Neurosci. Lett.*, vol. 480, no. 1, pp. 69–72, 2010.
[106] R. Inzelberg, J. A. Ramirez, P. Nisipeanu, and A. Ophir, "Retinal nerve fiber layer thinning in Parkinson disease," *Vision Res.*, vol. 44, no. 24, pp. 2793–2797, 2004.
[107] S. Kirbas, K. Turkyilmaz, A. Tufekci, and M. Durmus, "Retinal nerve fiber layer thickness in Parkinson disease," *J. Neuro-Ophthalmology*, vol. 33, no. 1, pp. 62–65, 2013.
[108] P. Barboni *et al.*, "Retinal nerve fiber layer evaluation by optical coherence tomography in Leber's hereditary optic neuropathy," *Ophthalmology*, vol. 112, no. 1, pp. 120–126, 2005.
[109] E. Ivanova, A. H. Toychiev, C. W. Yee, and B. T. Sagdullaev, "Intersublaminar Vascular Plexus: The Correlation of Retinal Blood Vessels With Functional Sublaminae of the Inner Plexiform Layer," *Invest. Ophthalmol. Vis. Sci.*, vol. 55, no. 1, pp. 78–86, Jan. 2014.
[110] M. Ruggeri *et al.*, "In vivo three-dimensional high-resolution imaging of rodent retina with spectral-domain optical coherence tomography.," *Invest. Ophthalmol. Vis. Sci.*, vol. 48, no. 4, pp. 1808–1814, Apr. 2007.
[111] J. Molnár, D. Chetverikov, D. C. DeBuc, W. Gao, and G. M. Somfai, "Layer extraction in rodent retinal images acquired by optical coherence tomography," *Mach. Vis. Appl.*, vol. 23, no. 6, pp. 1129–1139, 2012.
[112] A. Yazdanpanah, G. Hamarneh, B. R. Smith, and M. V Sarunic, "Segmentation of intra-retinal layers from optical coherence tomography images using an active contour approach," *IEEE Trans. Med. Imaging*, vol. 30, no. 2, pp. 484–496, 2011.
[113] B. J. Antony *et al.*, "A combined machine-learning and graph-based framework for the segmentation of retinal surfaces in SD-OCT volumes," *Biomed. Opt. Express*, vol. 4, no. 12, pp. 2712–2728, 2013.
[114] P. P. Srinivasan, S. J. Heflin, J. A. Izatt, V. Y. Arshavsky, and S. Farsiu, "Automatic segmentation of up to ten layer boundaries in SD-OCT images of the mouse retina with and without missing layers due to pathology," *Biomed. Opt. Express*, vol. 5, no. 2, pp. 348–365, 2014.
[115] W. K. Pratt, *Digital Image Processing*. New York, NY, USA: John Wiley & Sons, Inc., 1978.
[116] S. K. Singh and G. S. Maddala, "A function for size distribution of incomes," in *Modeling income distributions and Lorenz curves*, Springer, 2008, pp. 27–35.
[117] W. J. Zimmer, J. B. Keats, and F. K. Wang, "The Burr XII distribution in reliability analysis," *J. Qual. Technol.*, vol. 30, no. 4, p. 386, 1998.
[118] S. R. Lindsay, G. R. Wood, and R. C. Woollons, "Modelling the diameter distribution of forest stands using the Burr distribution," *J. Appl. Stat.*, vol. 23, no. 6, pp. 609–620, 1996.
[119] M. A. P. Taylor, "Modelling travel time reliability with the Burr distribution," *Procedia-Social Behav. Sci.*, vol. 54, pp. 75–83, 2012.
[120] Y. Jia *et al.*, "Quantitative OCT angiography of optic nerve head blood flow," *Biomed. Opt. Express*, vol. 3, no. 12, pp. 3127–3137, 2012.

[121] L. Liu *et al*., "Optical coherence tomography angiography of the peripapillary retina in glaucoma," *JAMA Ophthalmol*., vol. 133, no. 9, pp. 1045–1052, 2015.
[122] A. Yarmohammadi *et al*., "Optical coherence tomography angiography vessel density in healthy, glaucoma suspect, and glaucoma eyes," *Invest. Ophthalmol. Vis. Sci*., vol. 57, no. 9, p. OCT451-OCT459, 2016.
[123] S. G. K. Gadde *et al*., "Quantification of vessel density in retinal optical coherence tomography angiography images using local fractal dimension," *Invest. Ophthalmol. Vis. Sci*., vol. 57, no. 1, pp. 246–252, 2016.
[124] H. Taud and J.-F. Parrot, "Measurement of DEM roughness using the local fractal dimension," *Géomorphologie Reli. Process. Environ*., vol. 11, no. 4, pp. 327–338, 2005.
[125] N. Sarkar and B. B. Chaudhuri, "An efficient differential box-counting approach to compute fractal dimension of image," *IEEE Trans. Syst. Man. Cybern*., vol. 24, no. 1, pp. 115–120, 1994.
[126] K. A. Vermeer, J. van der Schoot, H. G. Lemij, and J. F. de Boer, "RPE-Normalized RNFL Attenuation Coefficient Maps Derived from Volumetric OCT Imaging for Glaucoma AssessmentRNFL Attenuation Coefficient Maps for Glaucoma," *Invest. Ophthalmol. Vis. Sci*., vol. 53, no. 10, pp. 6102–6108, 2012.
[127] U. C. Dräger and J. F. Olsen, "Ganglion cell distribution in the retina of the mouse.," *Invest. Ophthalmol. Vis. Sci*., vol. 20, no. 3, pp. 285–293, 1981.
[128] C.-J. Jeon, E. Strettoi, and R. H. Masland, "The major cell populations of the mouse retina," *J. Neurosci*., vol. 18, no. 21, pp. 8936–8946, 1998.
[129] J. D. Wilson, C. E. Bigelow, D. J. Calkins, and T. H. Foster, "Light Scattering from Intact Cells Reports Oxidative-Stress-Induced Mitochondrial Swelling," *Biophys. J*., vol. 88, no. 4, pp. 2929–2938, 2005.
[130] N. N. Boustany, R. Drezek, and N. V Thakor, "Calcium-Induced Alterations in Mitochondrial Morphology Quantified in Situ with Optical Scatter Imaging," *Biophys. J*., vol. 83, no. 3, pp. 1691–1700, 2002.
[131] R. M. Pasternack, J.-Y. Zheng, and N. N. Boustany, "Optical scatter changes at the onset of apoptosis are spatially associated with mitochondria," vol. 15, no., pp. 40503–40504, 2010.
[132] N. N. Boustany, Y.-C. Tsai, B. Pfister, W. M. Joiner, G. A. Oyler, and N. V Thakor, "BCL-xL-dependent light scattering by apoptotic cells.," *Biophys. J*., vol. 87, no. 6, pp. 4163–4171, Dec. 2004.
[133] B. Beauvoit, S. M. Evans, T. W. Jenkins, E. E. Miller, and B. Chance, "Correlation between the light scattering and the mitochondrial content of normal tissues and transplantable rodent tumors.," *Anal. Biochem*., vol. 226, no. 1, pp. 167–174, Mar. 1995.
[134] C. K. Joo *et al*., "Necrosis and apoptosis after retinal ischemia: involvement of NMDA-mediated excitotoxicity and p53.," *Invest. Ophthalmol. Vis. Sci*., vol. 40, no. 3, pp. 713–720, Mar. 1999.
[135] E. Bonfoco, D. Krainc, M. Ankarcrona, P. Nicotera, and S. A. Lipton, "Apoptosis and necrosis: two distinct events induced, respectively, by mild and intense insults

with N-methyl-D-aspartate or nitric oxide/superoxide in cortical cell cultures," *Proc. Natl. Acad. Sci.*, vol. 92, no. 16, p. 7162 LP-7166, Aug. 1995.
[136] M. J. Barsoum *et al.*, "Nitric oxide-induced mitochondrial fission is regulated by dynamin-related GTPases in neurons.," *EMBO J.*, vol. 25, no. 16, pp. 3900–3911, 2006.
[137] S. Oddo *et al.*, "Triple-transgenic model of Alzheimer's Disease with plaques and tangles: Intracellular Aβ and synaptic dysfunction," *Neuron*, vol. 39, no. 3, pp. 409–421, Jul. 2003.
[138] M. MESULAM, "A plasticity-based theory of the pathogenesis of Alzheimer's disease," *Ann. N. Y. Acad. Sci.*, vol. 924, no. 1, pp. 42–52, 2000.
[139] M. A. Mastrangelo and W. J. Bowers, "Detailed immunohistochemical characterization of temporal and spatial progression of Alzheimer's disease-related pathologies in male triple-transgenic mice," *BMC Neurosci.*, vol. 9, no. 1, p. 81, 2008.
[140] S. Oddo, A. Caccamo, M. Kitazawa, B. P. Tseng, and F. M. LaFerla, "Amyloid deposition precedes tangle formation in a triple transgenic model of Alzheimer's disease.," *Neurobiol. Aging*, vol. 24, no. 8, pp. 1063–1070, Dec. 2003.
[141] L. M. Billings, S. Oddo, K. N. Green, J. L. McGaugh, and F. M. LaFerla, "Intraneuronal Abeta causes the onset of early Alzheimer's disease-related cognitive deficits in transgenic mice.," *Neuron*, vol. 45, no. 5, pp. 675–688, Mar. 2005.
[142] L. Gimenez-Llort *et al.*, "Modeling behavioral and neuronal symptoms of Alzheimer's disease in mice: a role for intraneuronal amyloid," *Neurosci. Biobehav. Rev.*, vol. 31, no. 1, pp. 125–147, 2007.
[143] A. C. Neves *et al.*, "Alzheimer's disease: can the retina be a window to the brain?," *Acta Ophthalmol.*, vol. 95, no. S259, 2017.
[144] M. Chiasseu *et al.*, "Tau accumulation in the retina promotes early neuronal dysfunction and precedes brain pathology in a mouse model of Alzheimer's disease," *Mol. Neurodegener.*, vol. 12, no. 1, p. 58, 2017.
[145] L. S. Liebovitch and T. Toth, "A fast algorithm to determine fractal dimensions by box counting," *Phys. Lett. A*, vol. 141, no. 8–9, pp. 386–390, 1989.
[146] Y. Ohyagi *et al.*, "Intracellular Abeta42 activates p53 promoter: a pathway to neurodegeneration in Alzheimer's disease.," *FASEB J. Off. Publ. Fed. Am. Soc. Exp. Biol.*, vol. 19, no. 2, pp. 255–257, Feb. 2005.
[147] Z. Suo *et al.*, "GRK5 deficiency leads to early Alzheimer-like pathology and working memory impairment.," *Neurobiol. Aging*, vol. 28, no. 12, pp. 1873–1888, Dec. 2007.
[148] X.-J. Han *et al.*, "Amyloid β-42 induces neuronal apoptosis by targeting mitochondria," *Mol. Med. Rep.*, vol. 16, no. 4, pp. 4521–4528, Oct. 2017.
[149] S. Desagher and J.-C. Martinou, "Mitochondria as the central control point of apoptosis," *Trends Cell Biol.*, vol. 10, no. 9, pp. 369–377, 2000.
[150] A. Gross, J. M. McDonnell, and S. J. Korsmeyer, "BCL-2 family members and the mitochondria in apoptosis," *Genes Dev.*, vol. 13, no. 15, pp. 1899–1911, 1999.

[151] J. R. Mourant, J. P. Freyer, a H. Hielscher, a a Eick, D. Shen, and T. M. Johnson, "Mechanisms of light scattering from biological cells relevant to noninvasive optical-tissue diagnostics.," *Appl. Opt.*, vol. 37, no. 16, pp. 3586–3593, 1998.
[152] M. A. Samuel, Y. Zhang, M. Meister, and J. R. Sanes, "Age-related alterations in neurons of the mouse retina," *J. Neurosci.*, vol. 31, no. 44, pp. 16033–16044, 2011.
[153] D. L. Budenz *et al.*, "Determinants of Normal Retinal Nerve Fiber Layer Thickness Measured by Stratus OCT," *Ophthalmology*, vol. 114, no. 6, pp. 1046–1052, 2007.
[154] P. H. Peng, S. Y. Hsu, W. S. Wang, and M. L. Ko, "Age and axial length on peripapillary retinal nerve fiber layer thickness measured by optical coherence tomography in nonglaucomatous Taiwanese participants," *PLoS One*, vol. 12, no. 6, p. e0179320, Jun. 2017.
[155] D. Bendschneider *et al.*, "Retinal nerve fiber layer thickness in normals measured by spectral domain OCT," *J. Glaucoma*, vol. 19, no. 7, pp. 475–482, 2010.
[156] R. S. Parikh, S. R. Parikh, G. C. Sekhar, S. Prabakaran, J. G. Babu, and R. Thomas, "Normal age-related decay of retinal nerve fiber layer thickness," *Ophthalmology*, vol. 114, no. 5, pp. 921–926, 2007.
[157] W. J. Feuer *et al.*, "Topographic Differences in the Age-Related Changes in the Retinal Nerve Fiber Layer of Normal Eyes Measured by Stratus™ Optical Coherence Tomography," *J. Glaucoma*, vol. 20, no. 3, p. 133, 2011.

Vita

Michael R. Gardner is originally from Clifton, Texas, and earned a BS in Biomedical Engineering from Purdue University in 2012. After spending two years in the Middle East teaching English and studying Arabic, he returned to Texas and earned a MSE in Biomedical Engineering from the University of Texas at Austin in 2016. His PhD is in the same field. In 2018, he was selected as a Fulbright Scholar by the U.S. Department of State to teach optics and image processing at a university in the Middle East.

Permanent email: gardnermr@icloud.com

This dissertation was typed by the author.